2011

Control design and genetic algorithm optimization for electrostatic MEMS

Jill C. Blecke
Michigan Technological University

CONTROL DESIGN AND GENETIC ALGORITHM OPTIMIZATION FOR ELECTROSTATIC MEMS

By

Jill C. Blecke

A DISSERTATION

Submitted in partial fulfillment of the requirements for the degree of

DOCTOR OF PHILOSOPHY

(Mechanical Engineering – Engineering Mechanics)

MICHIGAN TECHNOLOGICAL UNIVERSITY

2011

This dissertation, "CONTROL DESIGN AND GENETIC ALGORITHM OPTIMIZATION FOR ELECTROSTATIC MEMS," is hereby approved in partial fulfillment for the requirements for the Degree of DOCTOR OF PHILOSOPHY IN Mechanical Engineering – Engineering Mechanics.

Department of Mechanical Engineering – Engineering Mechanics

Advisor: _____
Dr. Gordon G. Parker

Committee Member: _____
Dr. Chris Passerello

Committee Member: _____
Dr. Michele Miller

Committee Member: _____
Dr. Sarah Green

Department Chair: _____
Professor William W. Predebon

Date: _____

Contents

List of Figures

List of Tables

Acknowledgments

First and foremost, I would like to thank my advisor, Dr. Gordon G. Parker for being an incredible role model, teacher and mentor. The time, technical knowledge and advice he self-lessly shared on a daily basis were invaluable and so greatly appreciated. Much of my achievement would not have been possible without him and I am deeply grateful for his dedication to my success.

Secondly, I would like to thank the members of my committee, Dr. Chris Passerello, Dr. Michele Miller and Dr. Sarah Green, for the sharing of their time and knowledge in my pursuit of graduate degrees.

I would also like to thank the staff members at Sandia National Laboratories in Albuquerque, NM for their support of my work throughout my graduate career. The projects handed to me with confidence and mentoring given to me by the organization has greatly contributed to molding me into the researcher I am today.

Finally, I would like to thank my family for their unwavering love and support, both financially and emotionally. I would not be where I am today, or the person I am today, without them. I would also like to thank all of my friends that I have met along the way for always keeping my spirits high and their kind words of encouragement throughout the journey.

Abstract

CONTROL DESIGN AND GENETIC ALGORITHM OPTIMIZATION FOR ELECTROSTATIC MEMS

Jill C. Blecke

Michigan Technological University, 2011

Advisor: Dr. Gordon G. Parker

This dissertation discusses structural-electrostatic modeling techniques, genetic algorithm based optimization and control design for electrostatic micro devices.

First, an alternative modeling technique, the interpolated force model, for electrostatic micro devices is discussed. The method provides improved computational efficiency relative to a benchmark model, as well as improved accuracy for irregular electrode configurations relative to a common approximate model, the parallel plate approximation model. For the configuration most similar to two parallel plates, expected to be the best case scenario for the approximate model, both the parallel plate approximation model and the interpolated force model maintained less than 2.2% error in static deflection compared to the benchmark model. For the configuration expected to be the worst case scenario for the parallel plate approximation model, the interpolated force model maintained less than 2.9% error in static

deflection while the parallel plate approximation model is incapable of handling the configuration.

Second, genetic algorithm based optimization is shown to improve the design of an electrostatic micro sensor. The design space is enlarged from published design spaces to include the configuration of both sensing and actuation electrodes, material distribution, actuation voltage and other geometric dimensions. For a small population, the design was improved by approximately a factor of 6 over 15 generations to a fitness value of 3.2 fF. For a larger population seeded with the best configurations of the previous optimization, the design was improved by another 7% in 5 generations to a fitness value of 3.0 fF.

Third, a learning control algorithm is presented that reduces the closing time of a radio-frequency microelectromechanical systems switch by minimizing bounce while maintaining robustness to fabrication variability. Electrostatic actuation of the plate causes pull-in with high impact velocities, which are difficult to control due to parameter variations from part to part. A single degree-of-freedom model was utilized to design a learning control algorithm that shapes the actuation voltage based on the open/closed state of the switch. Experiments on 3 test switches show that after 5-10 iterations, the learning algorithm lands the switch with an impact velocity not exceeding 0.2 m/s, eliminating bounce.

1. Introduction

Microelectromechanical Systems (MEMS) have the properties of being small, light weight, capable of high frequency operation and relatively low cost. This provides performance advantages over their macro scale counterparts when incorporated in various applications such as sensors, switches, actuators and other structures (1, 2). As MEMS devices rise in popularity, so does the need for improved modeling techniques and control strategies to aid in their design and eventual implementation into larger systems. The purpose of this work is three-fold. The first goal is to advance the modeling techniques of electrostatic MEMS devices by developing an improved electrostatic model for use in optimization algorithms and control design that improves upon accuracy of approximate models, but does not compromise computational efficiency. The second goal is to improve upon the overall design of electrostatic MEMS devices by employing a multi-objective genetic algorithm based optimization program with integrated control, capable of filtering invalid geometries. The third goal is to improve the performance of MEMS devices with strategic learning control that preserves the practicality of the device for use outside of a laboratory setting.

There exist multi-physics analysis codes that are capable of detailed modeling of the interaction between structural and electrostatic coupled systems (3). However, for operations such as optimization based design, where computational efficiency is required, complex

models are not practical. A simplified electrostatic model can approximate the device as two parallel electrode plates and estimates the nonlinear attractive distributed force based on the capacitance (4). A major assumption of this approach is that the electrostatic field is uniform between the plates, as it neglects fringing effects. In this work, where genetic algorithms will be employed to perform discrete topology optimization of both the material and electrode distribution of the device, this assumption is often violated and there exists a need for an intermediate electrostatic model. The objective here is to develop an improved electrostatic model that approximates fringing effects, but still preserves the practical solution times for use in optimization algorithms and control design.

As MEMS devices become more complex and advances in fabrication extends the design space of features, finding optimal designs becomes more challenging. For capacitive-sensing electrostatic MEMS devices, design involves decisions of geometry and electrode configurations. Material distribution as well as size and location of both actuation and sensing electrodes are important players in their behavior. Typically these types of problems have many local minima so gradient-based optimization methods have a tendency to find the nearest local minima to the starting solution. Genetic algorithms can be useful in computing an optimal geometry for MEMS devices that have multiple objectives or large design spaces (5–8). In this research, a genetic algorithm optimization function will be employed to aid in the design of a MEMS resonant mass sensor. An alternative sensing technique will also be discussed.

A major factor in the performance of MEMS devices is part-to-part variation due to large fabrication tolerances relative to device dimensions (9). Another major challenge in control of MEMS lies in limited sensing techniques on the micro scale (10). The control problem in this work will be demonstrated on an electrostatically actuated, radio-frequency

MEMS switch and will focus on reducing the effects of part-to-part variation by employing a practical learning control strategy that relies only on the sensed potential difference between the electrodes. The benefit of this type of control is that it is practical outside of a laboratory setting and can act as a calibration tool over the lifetime of the part, accounting for variations due to both fabrication or altered properties of the device due to aging or wear.

The remainder of the document is organized as follows: Chapter 2 will provide a brief introduction to electrostatics and genetic algorithm optimization. The literature review in Chapter 3 is broken into three parts: (i) analytical formulas to approximate the capacitance for parallel plate capacitor type devices, (ii) use of genetic algorithms for optimization of MEMS device design and (iii) control strategies for electrostatically actuated MEMS devices. Chapter 4 describes the development of an improved structural-electrostatic model for electrostatic MEMS devices. A proposed sensing method for MEMS mass sensors using input shaping techniques is discussed in Chapter 5. Chapter 6 breaks down the details of genetic algorithm optimization for improving the design of a MEMS resonant mass sensor. Learning control strategies to eliminate bounce for a RF-MEMS switch are discussed in Chapter 7. Chapter 8 and Chapter 9 will describe potential future work beyond the scope of this project and a summary of the contributions, respectively.

2. Background

2.1 Electrostatic Modeling

This section will introduce the governing equations of electrostatics to form the foundation equations upon which electrostatically actuated MEMS devices operate. Further derivations, explanations and applications of these equations are available in (11).

Electrostatic force equations begin with Coulomb's law which states that the electrostatic force, $\vec{F}$, on a charged particle, q_1, due to a second charged particle, q_2, is equal to Eq. 2.1, where ϵ_0 is the permittivity of free space (8.854×10^{-12} F/m), $\vec{r}_i$ is the position vector of each charge. A system of two charged particles is illustrated in Figure 2.1(a).

The following notation will be used throughout the remainder of this section: r - scalar, $\vec{r}$ - vector, $\vec{\boldsymbol{r}}$ - unit vector, $|\vec{r}|$ - magnitude of a vector.

$$\vec{F} = \frac{q_1 q_2 (\vec{r}_1 - \vec{r}_2)}{4\pi\epsilon_0 |\vec{r}_1 - \vec{r}_2|^3} = \frac{q_1 q_2 \vec{\boldsymbol{r}}_{12}}{4\pi\epsilon_0 |\vec{r}_{12}|^2} \tag{2.1}$$

Eq. 2.1 can be extended to compute the electrostatic force on charge, q_i, by a system of n charges by summing up the forces of each charge, q_j, shown in Eq. 2.2. A system of n

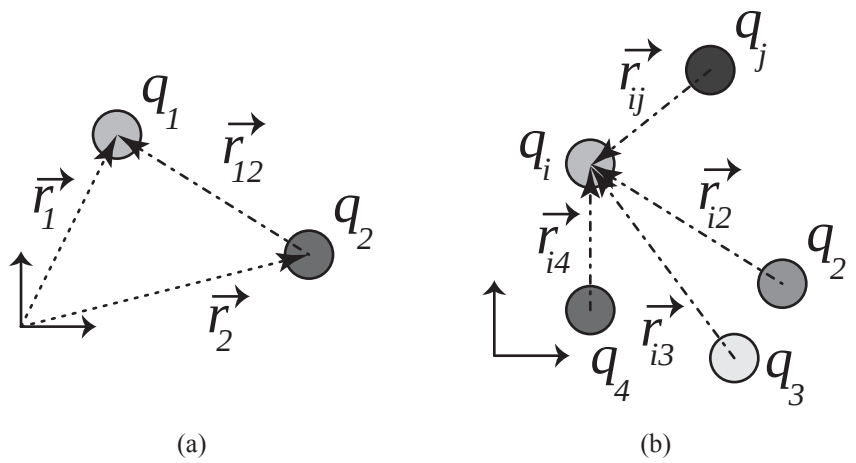

Figure 2.1. (a) System of two charged particles; (b) System of n charged particles

charged particles is illustrated in Figure 2.1(b).

$$\vec{F}_{ij} = \frac{q_i}{4\pi\epsilon_0} \sum_{j=1}^{n} q_j \frac{\vec{\boldsymbol{r}}_{ij}}{|\vec{r}_{ij}|^2} \tag{2.2}$$

If a charge, q is small enough such that it does not disturb other charges in the vicinity, then the electrostatic field, $\vec{E}$, is defined as the force per unit charge and can be computed using Eq. 2.3.

$$\vec{E} = \frac{\vec{F}}{q} \tag{2.3}$$

The electrostatic field due to a single point charge, q, at any location, $\vec{r}_i$, is described by Eq. 2.4.

$$\vec{E}_i = \frac{q(\vec{r}_i - \vec{r})}{4\pi\epsilon_0 |\vec{r}_i - \vec{r}|^3} \tag{2.4}$$

Extended to a system of n charges, the electrostatic field at any location, $\vec{r}_i$, is described by Eq. 2.5.

$$\vec{E}_{ij} = \sum_{j=1}^{n} \frac{q_j \vec{\boldsymbol{r}}_{ij}}{4\pi\epsilon_0 |\vec{r}_{ij}|^2} \tag{2.5}$$

In the case of a charge density, $\rho(x, y, z)$, in a volume, V, the electrostatic field is described by Eq. 2.6, where $\vec{r}$ is the position vector from the volume element to the point of interest.

$$\vec{E}(x, y, z) = \frac{1}{4\pi\epsilon_0} \int_V \rho(x, y, z) \frac{\vec{\boldsymbol{r}}}{|\vec{r}|^2} \tag{2.6}$$

An important relation to acknowledge is given by Eq. 2.7. Substituting Eq. 2.7 into Eq. 2.6, the electrostatic field can also be expressed as Eq. 2.8.

$$\frac{\vec{\boldsymbol{r}}}{|\vec{r}|^2} = -\nabla \left(\frac{1}{|\vec{r}|} \right) \tag{2.7}$$

$$\vec{E}(x, y, z) = \frac{-1}{4\pi\epsilon_0} \int_V \rho \nabla \left(\frac{1}{|\vec{r}|} \right) dV \tag{2.8}$$

The gradient computation can be pulled outside the integral if both the limits of integration and the charge density are not functions of the evaluation location.

$$\vec{E}(x, y, z) = -\nabla \frac{1}{4\pi\epsilon_0} \int_V \rho \left(\frac{1}{|\vec{r}|} \right) dV \tag{2.9}$$

The integrand in Eq. 2.9 is a scalar quantity at each location and is defined as the electrostatic potential function, ϕ, shown in Eq. 2.10. This allows for the more compact form of Eq. 2.9, shown in Eq. 2.11.

$$\phi = \int_V \frac{\rho}{4\pi\epsilon_0|\vec{r}|} dV \tag{2.10}$$

$$E = -\nabla\phi \tag{2.11}$$

The electric flux, D is proportional to the electrostatic field, shown by Eq. 2.12. Substituting Eq. 2.6 into Eq. 2.12, the flux can also be expressed as Eq. 2.13.

$$\vec{D} = \epsilon_0\vec{E} \tag{2.12}$$

$$\vec{D} = \frac{1}{4\pi}\int_V \rho\frac{\vec{\boldsymbol{r}}}{|\vec{r}|^2} \tag{2.13}$$

Gauss' law, shown in Eq. 2.14, states that the surface integral of the electric flux is equal to the total charge in a volume surrounded by the closed surface, S. Since the electrostatic field within a conductor is zero, if the closed surface is comprised entirely of conducting material, the total charge and the electric flux, are zero.

$$\int_S \vec{D}\cdot d\vec{S} = \int_V \rho dV \tag{2.14}$$

If the charge density is a continuous function, the divergence theorem can be applied

and Eq. 2.14 can be re-written as Eq. 2.15.

$$\int_S \vec{D} \cdot d\vec{S} = \int_V \nabla \cdot \vec{D} dV \tag{2.15}$$

Equating the right hand sides of Eq. 2.14 and Eq. 2.15, the charge distribution can be related to the electric potential though the flux and electrostatic field equations, shown in Eq. 2.11 and Eq. 2.12. Eq. 2.16 is the differential form of Gauss' law and is commonly referred to as Poisson's equation.

$$\nabla \vec{D} = \rho \longrightarrow \nabla(-\nabla\phi) = \rho \longrightarrow \nabla^2\phi = -\frac{\rho}{\epsilon_0} \tag{2.16}$$

In a region free of any charge, Eq. 2.16 becomes Eq. 2.17, and is known as Laplace's equation.

$$\nabla^2\phi = 0 \tag{2.17}$$

2.2 Genetic Algorithm Based Optimization

Genetic algorithm based optimization is an evolutionary based method of searching a design space for an optimal solution. Each possible configuration in the design space is represented by a bit string of finite length, referred to as a member. The numerical solution to a genetic algorithm optimization problem is defined by the size of the population, number of generations and the fitness function that is to be minimized in the optimization.

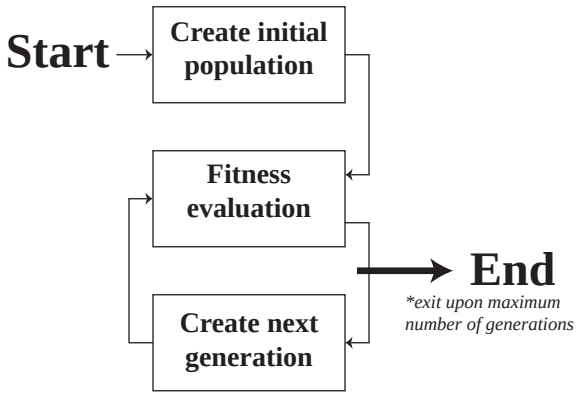

Figure 2.2. Genetic algorithm based optimization

The schematic in Figure 2.2 shows the process flow of a generic genetic algorithm based optimization code, for which there are 3 key steps.

Step 1 is to randomly generate the members of the initial population. Step 2 is to evaluate each member of the population in the current generation according to the fitness function. Each member is ranked, where the best configuration is the member with the lowest fitness value. If the generation just evaluated is not the final generation, a new population for the next generation is created using 3 distinct processes - elite members, crossover and mutation. Elite members are the members of the previous generation that have the lowest fitness values. These members automatically survive to the next generation. Crossover creates children for the new population by combining two parents from the previous generation. The mutation process creates members for the new population by applying a small probability of modest alterations to members of the current generation. Once the population of the new generation is created, each member is evaluated, ranked, and the process repeats until the maximum number of generations set by the user is reached. The output of the

genetic algorithm optimization is the set of members in the final generation with the lowest fitness values.

The disadvantages of genetic algorithm optimization are that a global minimum solution is not guaranteed and that it can become computationally expensive. An advantage, however, is that it is perfectly positioned to handle discrete design variables and that the entire design space can be searched without being constrained to local minima. It is for these advantages that genetic algorithm based optimization was chosen for this work.

3. Literature Review

The literature review provided below will describe published research for 3 main topics:

1. Analytical formulas to approximate the capacitance for parallel plate capacitor type devices, including MEMS,

2. Use of genetic algorithms for optimization of MEMS device design, and

3. Control strategies for electrostatically actuated MEMS devices.

3.1 Electrostatic Models

The modeling spectrum, from complex to simple, illustrated in Figure 3.1, for electrostatic devices ranges from fully-coupled, structural-electrostatic analysis to a parallel plate approximation. The fully-coupled, structural-electrostatic analysis allows for accurate solutions, but can be too computationally expensive for use in optimization or control design applications. On the opposite end of the spectrum, the parallel plate approximation is a common simplified model that provides enormous reduction in solution time, but cannot take into account fringing forces near the edges of the electrodes. Many researchers have ad-

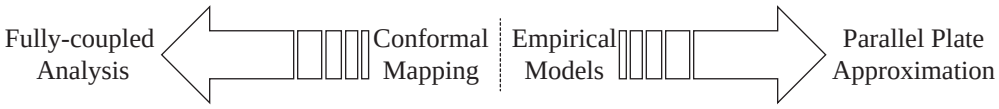

Figure 3.1. Electrostatic model spectrum from complex to simple, left to right

dressed inclusion of higher order effects attempting to find a balance between computational efficiency and accuracy using conformal mapping techniques and by computing empirical models for a defined geometry set. Section 3.1.1 and Section 3.1.2 briefly describes the fully-coupled structural-electrostatic analysis and the parallel plate model, respectively. A discussion of published analytical models designed to take into account the fringing fields ignored by the parallel plate model, follows in Section 3.1.3.

3.1.1 Fully-Coupled, Structural-Electrostatic Analysis

Consider the system consisting of two conducting plates held at a voltage differential, V, shown in Figure 3.2. The plates are of length, l, width, w, thickness, t and are separated by an air gap, g.

The electric potential between the two plates satisfies Laplace's equation, given by Eq. 3.1. Fully-coupled, structural-electrostatic analysis codes exist that compute the solution to Laplace's equation, subject to the appropriate boundary conditions, and uses the electric potential solution to compute the electrostatic force, which serves as an input to the structural analysis. The magnitude of the electrostatic force is dependent upon the instantaneous air gap from the structural analysis, thus coupling the two analyses.

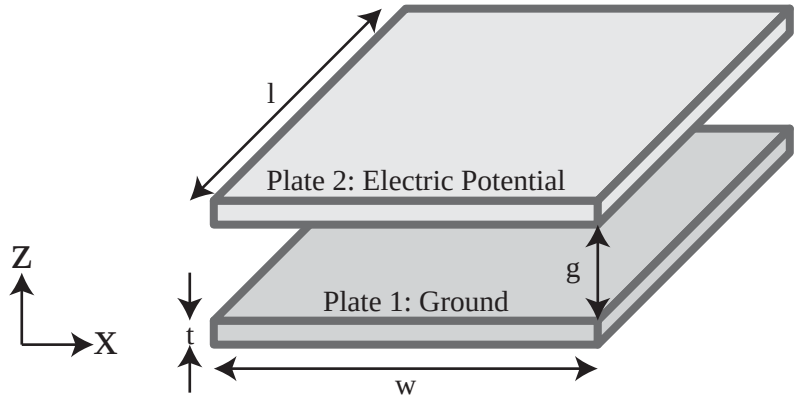

Figure 3.2. Two parallel conducting plates held at a voltage potential, V

$$\frac{\partial^2 \phi}{\partial x^2} + \frac{\partial^2 \phi}{\partial y^2} + \frac{\partial^2 \phi}{\partial z^2} = 0 \tag{3.1}$$

Figure 3.3 shows a cross-section view of the electric potential through the center of two fixed plates using COMSOL Multiphysics. Near the center of the plates, away from the edges, the potential only varies linearly in the z-direction between the two plates. Near the edges, the electric potential also varies in the x-direction, as well as the y-direction into the page, which is not shown in this view. The fringing forces generated near the edges of the electrodes will be the center of the discussion in the remainder of this section.

3.1.2 Parallel Plate Approximation Model

The parallel plate approximation neglects fringing effects, reducing the Laplace equation in Eq. 3.1 to Eq. 3.2, subject to the given boundary conditions.

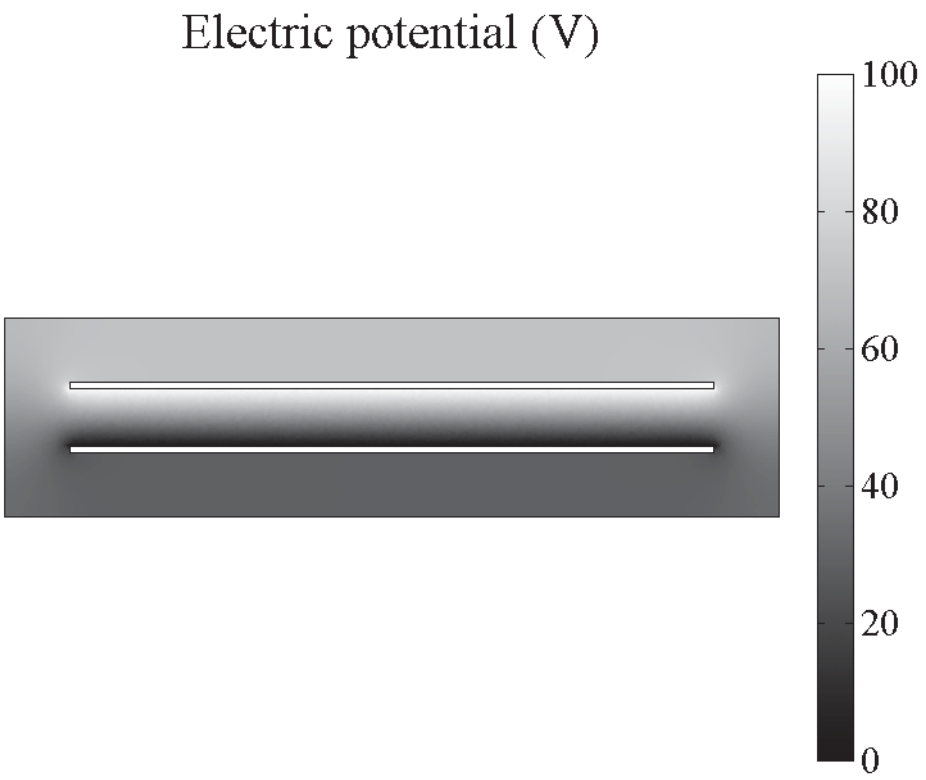

Figure 3.3. Voltage potential, V, in volts, between two parallel plates held at a 100 V potential difference

$$\left.\frac{\partial^2 \phi}{\partial z^2} = 0\right\} \phi(0) = 0; \phi(g) = V \tag{3.2}$$

A solution for Eq. 3.2 is given by Eq. 3.3. This solution requires that the electric field is uniform between the two plates. The magnitude of the uniform electrostatic field is given by Eq. 3.4.

$$\phi(z) = \frac{Vz}{g} \tag{3.3}$$

$$E = \nabla\phi = -\frac{V}{g} \tag{3.4}$$

Substituting Eq. 3.4 into Eq. 2.12, the electric flux is written as Eq. 3.5. On the surface of a conductor, the electric flux density is equal to the surface charge density, σ. Thus, for electrode area, A, the total charge, Q, is given by Eq. 3.6.

$$D = \frac{\epsilon V}{g} \tag{3.5}$$

$$Q = \frac{\epsilon A V}{g} \tag{3.6}$$

Capacitance is defined as the ratio of charge to electric potential, so the parallel plate approximation for the capacitance between two plates held at a potential difference is given in Eq. 3.7.

$$C = \frac{Q}{V} = \frac{\epsilon A}{g} \tag{3.7}$$

3.1.3 Closed-Form Capacitance Formulas Including Fringing

Closed-form models that account for the fringing effects have been developed for drum-shaped electrostatic MEMS (12), circular disc capacitors (13, 14) and MEMS comb drive actuators (15, 16). This particular section will review the models applied to rectangular parallel plate capacitors and rectangular conducting lines over a ground plane. With the exception of one, the analytical capacitance formulas listed in this paper can be categorized

into those derived from conformal mapping techniques and those empirically derived. The remainder of this section will address the models in chronological order of the publication date for the references listed.

For this discussion, the following notation will be used - plate length, l (m); plate width, w (m); plate thickness, t (m); plate separation in the z-direction, g (m); permittivity of free space, ϵ_0 (F/m).

In 1937, Palmer (17) published a paper to increase accessibility to fringing models for parallel plate capacitors. The models listed in Palmer's article were derived using Schwartz-Christoffel transformations and are applicable to capacitors with plates of negligible thickness and large ratios of width to plate separation. The first model, shown by Eq. 3.8, takes into account the fringing of the flux and the flux passing through the back of the plates. The second model, given in Eq. 3.9, accounts for fringing near the ends of the finite plates. Both models give the capacitance per unit length of the device. The first term of each computes the capacitance due to the parallel plates. The second and third terms account for the fringing effects.

$$C = \frac{\epsilon w}{g}\left[1 + \frac{g}{w\pi} + \frac{g}{w\pi}\ln\left(\frac{2\pi w}{g}\right)\right] \tag{3.8}$$

$$C = \frac{\epsilon w}{g}\left[1 + \frac{g}{\pi w} + \frac{g}{\pi w}\ln\left(1 + \frac{\pi w}{g}\right)\right] \tag{3.9}$$

Also derived using conformal mapping techniques, Elliott (11) describes the total capacitance of a parallel plate capacitor given in Eq. 3.10. Once again, the first term calculates the capacitance from the plates and the fringing is accounted for by the second and third

terms.

$$C = \frac{\epsilon w l}{g}\left[1 + \frac{\ln\left(\frac{\pi w}{g}\right)}{\frac{\pi w}{g}} + \frac{\ln\left(\frac{\pi l}{g}\right)}{\frac{\pi l}{g}}\right] \tag{3.10}$$

Chang (18, 19) developed a model using approximate conformal mapping techniques. While the model, shown in Eq. 3.12, is an improvement in accuracy over the parallel plate approximation and takes into account fringing due to the thickness, relatively, it is a more complex capacitance computation and is limited to plates with a width to gap ratio larger than unity.

$$\begin{aligned}
C &= \frac{2\epsilon}{\pi}\ln\left(\frac{2R_b}{R_a}\right) \\
\ln\left(R_a\right) &= -1 - \frac{\pi w}{2g} - \left(\frac{p+a}{\sqrt{p}}\right)\tanh^{-1}\left(\frac{1}{\sqrt{p}}\right) - \ln\left(\frac{p-1}{4p}\right) \\
R_b &= \eta + \frac{p+1}{2}\ln\left(\Delta\right) \\
\eta &= \sqrt{p}\left[\frac{\pi w}{2g} + \frac{p+1}{2\sqrt{p}}\left[1 + \ln\left(\frac{4}{p-1}\right)\right] - 2\tanh^{-1}\left(\frac{1}{\sqrt{p}}\right)\right] \\
\Delta &= max\left(p, \eta\right) \\
p &= 2B^2 - 1 + \sqrt{\left(2B-1\right)^2 - 1} \\
B &= 1 + \frac{t}{g}
\end{aligned} \tag{3.11}$$

For a rectangular conductor, the authors in reference (20) approximated the capacitance due to the fringing field of a rectangular conductor by utilizing the circular capacitance formula and modeling the ends of the conductor as semicircles. For widths greater than half of the thickness, the capacitance per unit length is described by Eq. 3.12. The first term

computes the capacitance for a rectangular cross-section, subtracting off the two end pieces represented by semicircles. The capacitance due to the two end pieces are then computed by the second term. For widths less than half of the thickness, the capacitance per unit length is described by Eq. 3.13.

$$C = \epsilon \left[\frac{w - \frac{t}{2}}{g} + \frac{2\pi}{\ln\left(1 + \frac{2g}{t} + \sqrt{\frac{2g}{t}\left(\frac{2g}{t} + 2\right)}\right)} \right] \tag{3.12}$$

$$C = \epsilon \left[\frac{w}{g} + \frac{\pi\left(1 - \frac{0.0543t}{2g}\right)}{\ln\left(1 + \frac{2g}{t} + \sqrt{\frac{2g}{t}\left(\frac{2g}{t} + 2\right)}\right)} + 1.47 \right] \tag{3.13}$$

Seeking to decrease the complexity of Eq. 3.11, the authors in reference (21) derived an empirical model for the capacitance per unit length of a single line over a ground plane. Eq. 3.14 is valid for devices with a width to gap ratio and thickness to gap ratio of 0.3-30.

$$C = \epsilon \left[1.15\frac{w}{g} + 2.8\left(\frac{t}{g}\right)^{0.222} \right] \tag{3.14}$$

In reference (22) it is demonstrated that the accuracy of the empirical model in Eq. 3.14 could be improved by limiting the valid geometries. For wires with a width to gap ratio greater than unity and a thickness to gap ratio between 0.1 and 4, the capacitance per unit length can be described by Eq. 3.15.

$$C = \epsilon \left[\frac{w}{g} + 0.77 + 1.06\left(\frac{w}{g}\right)^{0.25} + 1.06\left(\frac{t}{g}\right)^{0.5} \right] \tag{3.15}$$

Empirical models for various shapes of capacitors are presented by references (23, 24).

For a micro-strip capacitor, the capacitance per unit length, including fringing effects, can be computed by Eq. 3.16 - Eq. 3.18. Eq. 3.16 is valid for gap to width ratios less than 0.01. Eq. 3.17 is valid for gap to width ratios between 0.01 and 0.1. Eq. 3.18 is valid for gap to width ratios larger than 0.1

$$C = \frac{\epsilon w}{g}\left[1 + 2.123\left(\frac{g}{w}\right)\right] \tag{3.16}$$

$$C = \frac{\epsilon w}{g}\left[1 + \sqrt{2.7781\left(\frac{g}{w}\right)^2 + 0.001097}\right] \tag{3.17}$$

$$C = \frac{\epsilon w}{g}\left[1 + 1.1205\left(\frac{g}{w}\right)^{0.8258}\right] \tag{3.18}$$

For a square capacitor, the capacitance per unit length, including fringing effects can be computed using Eq. 3.19 and Eq. 3.20. Eq. 3.19 is valid for gap to width ratios between 0.1 and unity. Eq. 3.20 is valid for gap to width ratios between 1.0 and 10.

$$C = \frac{\epsilon w}{g}\left[1 + 2.343\left(\frac{g}{w}\right)^{0.891}\right] \tag{3.19}$$

$$C = \frac{\epsilon w}{g}\left[1 + 2.343\left(\frac{g}{w}\right)^{0.992}\right] \tag{3.20}$$

The authors in reference (25) combined some of the fringing models described above to create a new analytical model for the capacitance of a electrostatically actuated MEMS parallel plate actuator. The capacitance per unit length of a device having a width to gap ratio larger than 5 can be computed using Eq. 3.21.

$$C = \frac{\epsilon w}{g}\left[1 + \frac{g}{w\pi} + \frac{g}{w\pi}\ln\left(\frac{2\pi w}{g}\right) + \frac{g}{w\pi}\ln\left(1 + \frac{2t}{g} + 2\sqrt{\frac{t}{g} + \frac{t^2}{g^2}}\right)\right] \tag{3.21}$$

Current literature provides viable options for modeling the fringing fields for two parallel plates separated by a gap. However, the fringing field models are limited to two electrodes that share the same dimensions and are directly aligned. The models fail to accurately represent the fringing for two plates that are not the same size or shape, such as the presence of a hole(s) in one of the plates or extra electrode areas neighboring one of the plates.

3.2 Genetic Algorithm Based Optimization and MEMS

Optimization techniques are beneficial to incorporate into the early stages of design for any type of device, and electrostatically actuated MEMS devices are no exception. Through the use of carefully designed optimization algorithms, optimum topologies, electrode sizes and locations, driving voltages and more can be discovered such that the performance of the device matches the target design behavior. This section will investigate how optimization algorithms have been utilized to assist in the design process of MEMS devices in general. While most optimization programs for MEMS have been centered on gradient based techniques (some examples include, but are certainly not limited to references (26–38)), this discussion will be focused on the use of genetic algorithm based optimization methods only.

Genetic algorithms began their use in the field of MEMS in regards to the design synthe-

sis of MEMS components. Li and Antonsson (39) employed genetic algorithms to optimize the synthesis of MEMS mask layouts and fabrication processes. The objective was to create a synthesis that resulted in as close to the desired 3D shape as possible, despite random shape and process variations. The authors in reference (40) demonstrated the use of genetic algorithms to optimize MEMS synthesis design as well, but expanded the objective to include the topology and size of the devices such that a particular performance characteristic was achieved. The design variables were the number, types and connectivity of basic components. The solution could then be further refined using gradient based optimization methods (41). Fan et al. (42) proposed a similar method of MEMS synthesis optimization, but also included the use of bond graphs.

Genetic algorithms have also been used to define physical properties of MEMS devices. The authors in reference (8) demonstrated the use of genetic algorithms to optimize the thickness of a micro-membrane to match a desired pump performance. In simulation, the membrane was divided into sections and the thickness of each section was represented by a bit, correlating to one of two thickness values. Susanto and Yang (43) optimized the force-deflection at the tip of a piezoelectric forceps using physical design parameters as the design variables, while the authors in reference (6) optimized the dimensions of a micro-beam resonator to achieve a desired frequency response curve. The dimensions of an electro-thermal actuator were also optimized by a genetic algorithm to maximize the deflection of the device (7). The authors in reference (44) optimized the dimensions of an RF-MEMS switch with a minimized actuation voltage and maximized dynamic stiffness by combining genetic algorithms with orthogonal experiment and BP neural network methods. Yuan et al. (45) expanded the design variables beyond dimensions to include the driving voltage as well, in which the global sensitivity of an electrostatically driven gyroscope was minimized by

genetic algorithm optimization. Engesser et al. (46) likewise expanded the design variable set to include geometric and material properties when minimizing the total area of a MEMS accelerometer. The authors in reference (47) employed genetic algorithms to define the discrete location and size of the piezoelectric components for a MEMS actuator. This optimization program was further wrapped in a gradient based optimization loop that performed topology optimization of the device. Further use of genetic algorithms for topology optimization in MEMS was documented by Motiee (48) who optimized an electro-thermal actuator to achieve a desired deflection at a given location. The authors in reference (49) used unique evolutionary programming to optimize the springs of a MEMS resonator device, taking into account both location noise and pre-stress, where the fitness of each design was computed as a function of its resonant frequency and deflection.

Current literature demonstrates that genetic algorithms are a great tool for the design and optimization of MEMS. The protocol can find a family of good solutions without being constrained by local minima. However, the optimization algorithms have not yet demonstrated constraint to connected geometries for discrete material topologies. Also, the design space could be expanded to include both material distribution, electrode configurations and applied voltages such that an entire system configuration could be optimized.

3.3 Control Design for Electrostatic MEMS

The inherent instability in electrostatic MEMS devices has sparked enormous efforts in control design to defeat pull-down and improve performance. The control objectives for electrostatic MEMS tend to focus around set-point control through the entire gap, tracking

a reference trajectory through the entire gap, compensation for parameter uncertainty that may lead to pull-down and self-calibration. Closed-loop control strategies are difficult to implement on such structures because of the high structural frequencies. Also, many times, sensors are not compatible with the size of micro devices or are not practical outside of a laboratory setting. While the open-loop strategies are simpler to implement, they cannot account for parameter variation, a trait very common due to uncertainty in MEMS fabrication or inaccurate models (10).

This section of the literature review will discuss control strategies already published generally focused around extending the stable operating range of electrostatic MEMS devices beyond pull-in, or avoiding the effects of pull-in. Control categories include open-loop device design considerations, open-loop input waveform design, introduction of additional circuitry to the system, closed-loop linear control, closed-loop nonlinear control and adaptive control.

There exists a plethora of excellent control strategies, both open-loop and closed-loop, published for a variety of electrostatic MEMS devices. Open-loop control strategies are capable of reducing or eliminating the effects of pull-down but lack robustness for parts subject to fabrication imperfections. Closed-loop control strategies are often times significantly more robust but are impractical and hide under implementation challenges defined by devices with high structural frequencies, availability of micro-sized sensors and complex control laws.

3.3.1 Open-loop Control of Electrostatic MEMS via Fabrication and Design Considerations

Simple design configurations can be made to improve the performance of MEMS devices by avoiding the effects of pull-down without the need to address the challenges of feedback. The first design consideration is unique electrode configurations. Legtenberg et al. (50) expanded the stable travel region of a beam by using a curved electrode, thereby favorably altering the pull-down behavior of the device. Another strategy is to use laterally offset electrodes, as opposed to electrodes directly across the gap. In this case, actuation is motivated strictly by the fringing forces due to the non-uniform electrostatic field at the edges, and the stable operating range can be expanded depending on the shape and location of the offset electrodes (51, 52). Hung and Senturia (53) defined a "leveraged bending" technique that designed uniquely shaped beams and actuated only selective areas of the device, such that the remainder performed as a lever and was allowed to extend beyond the original instability. The authors in reference (54) developed a unique sequential actuation scheme for a set of two different electrodes that was used to achieve stable displacements beyond pull-in for a comb drive. Rather than alter electrode shape or location, Wu et al. (55) coated the inner surface of a micro-mirror actuator with a silicon dioxide layer to create a larger stable operating range.

The counterpart to the use of novel electrode configurations for open-loop control of electrostatic MEMS devices beyond pull-in is to design unique flexure components. One tactic is to alter the material properties of the device. Hung and Senturia (53) developed a "strain stiffening" technique that introduced a geometric nonlinearity in the beam to improve stability. Similarly, the authors in reference (56) demonstrated that the curvature of

a structure can be altered by introducing a stress gradient along the length and width of a beam. Due to the change in stiffness of the curved beam, the stable travel range of the device was extended. A second tactic is to change the stiffness of the flexure components through shape design. Many novel suspension systems have been designed, including a spring design with stiffness properties such that the restorative force is proportional to the square, and higher orders, of the deflection (57). Zhou and Dowd (58) designed a "tilted folded-beam" suspension to improve the stability of a comb drive actuator, while the authors in reference (59) developed a flexure component inspired by a four bar linkage that created a nonlinear restoring force shown to improve the pull-in performance. Zhang and Dunn (60) created a "tailored topology" approach, where two bi-layer beams were connected together using a combination of plate and flexure components. The components not only created unique stiffness characteristics, but also electrode configurations to assist in the improved stability. The authors in reference (61) developed a two beam suspension design with one anchored beam and a single movable beam. This setup extended the stable travel range of the device.

3.3.2 Open-loop Control of Electrostatic MEMS via Input Waveform Design

A second control approach for electrostatic MEMS to avoid the negative effects of pull-down is special input waveforms to achieve desired performance. Nadal-Guardia et al. (62) used a current drive method for electrostatic MEMS actuators connected to a series capacitor for stable set point control. A current source delivered an initial charge and was then turned off to place the structure in a desired location. The authors in reference (10) proposed a high voltage spike followed by a trailing steady-state voltage to reduce vibrations in an electrostatic micro-optical-electro-mechanical system (MOEMS) comb drive. For a

bi-directional parallel plate actuator, a unique command of the polarity of the moving electrode relative to the stationary electrode was proven to allow stable set point control beyond pull-in (63). The authors in reference (64) applied an AC voltage with a DC offset to stabilize microstructures beyond pull-in. A pulse and hold waveform was shown to avoid pull-in and allow fast switching and soft-landing without bounce for RF-MEMS switches (65, 66). A similar pulse and hold waveform was also demonstrated in reference (67) for a MEMS switch that must traverse the entire gap. Chen and Ou also explored zero vibration and zero vibration derivative input shaping for the use of nonlinear two and three step shapers to reduce vibration in parallel plate actuators. Zero vibration response is achieved for a torsional micro-mirror by combining the static response of the system, an energy balance equation and a nonlinear approximation solution to analytically compute the magnitude and timing of pulses of the input waveform (68).

3.3.3 Open-loop Control of Electrostatic MEMS through Additional Circuitry Design

Another design consideration to extending the stable operating range of electrostatic MEMS devices is the addition of extra circuitry components in series with the device. Both a single capacitor and a "switched capacitor" circuit, consisting of an operational amplifier-capacitor combination, have been shown to extend stability beyond pull-down when placed in series with a parallel plate actuator under either voltage or charge control (69–72). Chan and Dutton (73) designed a special "folded capacitor" design to allow for stable control beyond pull-in. The introduction of an inductor-capacitor circuit in series with the device was also shown to extend the stable operating range of a parallel plate actuator (74). Cagdaser and

Boser (75) demonstrated that an inductor in series with the device, when actuated at its electrical resonance, extended the stable operating range as well.

3.3.4 Closed-loop Linear Control of Electrostatic MEMS

Linear controllers have been demonstrated as an option for position control of electrostatic MEMS. Chu and Pister (76) demonstrated the use of a proportional position feedback controller to extend the stable operating range of a microgirpper device. A proportional control law was also discussed for position control of a long-range micro-positioner in reference (77). A proportional controller supplemented with integral control was shown to provide position control for a lateral micro-actuator in reference (78) and a micro-mirror subject to uncertainty in reference (79). The authors in reference (80) utilized a proportional-integral-derivative (PID) controller for both translational position control and disturbance rejection for a comb resonator. The authors in reference (81) improved the performance of a dual-axis micro-mirror using PID control in multiple loops. A phase lead compensator was employed for position control of a parallel plate actuator in reference (82). Lu and Fedder (83, 84) used a pre-filter to enhance the performance of their linear time invariant (LTI) controlled micro-actuator.

3.3.5 Closed-loop Nonlinear Control of Electrostatic MEMS

By far the majority of publications for extending the stable operating range of electrostatic MEMS falls into nonlinear control due to the nonlinear nature of electrostatic actuation. Many of the nonlinear controllers have been shown to not only increase the operation range

of the devices, but also improve transient performance and robustness. One nonlinear control strategy is the design of closed-loop dynamic drives. The authors in (85–87) use a dynamic on-off voltage drive based on a threshold for the position feedback of parallel plate actuators. Nadal-Guardia et al. proposed using dynamic, on-off type, current drives to extend the stable travel range of parallel plate actuators (62) and torsional actuators (88). Chen et al. (89) designed a voltage drive that inputs a constant voltage for a tilt-angle micro-mirror at small angles and after crossing a threshold, can linearly or nonlinearly decreases the voltage as the device reaches the commanded position. Other nonlinear strategies also include switching control or sliding mode control (90–93) and model inversion or linearization (94, 95). Some work has been focused around supplementing conventional linear type controllers with nonlinear functions. The authors in reference (96) proposed two controllers, one that uses a linear proportional feedback combined with a timed step function, and another that uses sine wave feedback in conjunction with a step function. Borovic et al. (97) introduced a nonlinear proportional-derivative controller to control an optical switch. The control utilized a feedforward term as well to assist in fast switching with desireable overshoot performance. The authors in reference (98) also introduced a nonlinear proportional-derivative controller for the closed-loop control of a torsional micro-mirror and compared the performance to a gain scheduling approach. The authors in reference (99) designed a robust tracking control law based on energy. The control constrained the total energy in the system to be less than the minimum energy to achieve contact.

Extensive work has been published comparing various nonlinear controllers. References (100–108) compare nonlinear strategies applied to a parallel plate actuators and/or torsional micro-mirrors, including, but not limited to, control schemes based on differential flatness, Lyapunov stability, backstepping and trajectory planning. Various controllers

utilizing dynamic and static state or output feedback strategies for the stabilization of parallel plate actuators have also been compared in (109–112). Wang (113) compared various nonlinear feedback controls to control the position of a microbeam tip as well as suppress vibrations.

3.3.6 Adaptive and Self-Tuning Control of Electrostatic MEMS

Adaptive and self-tuning controllers lend well to accounting for uncertainty in modeling, environmental effects or imperfections in fabrications and the world of MEMS is no exception. The authors in reference (114) demonstrated the improved position control of a parallel plate actuator that is subjected to fabrication variations. An adaptive backstepping control was applied to a parallel plate actuator to improve robustness (115, 116). Both adaptive state feedback and adaptive output feedback have been shown to control bi-directional micro actuators (117–119). Stable control of a lateral comb resonator under both structure and fault conditions was demonstrated using self-tuning variable structure controllers (120, 121).

Current literature provides numerous control strategy options for electrostatically actuated micro devices. This work will aim to provide alternative learning control techniques that can adapt based on previous behavior of the device, improve the performance of the device and use sensing techniques viable for real world implementation.

4. Modeling of Electrostatic MEMS

In Chapter 6, genetic algorithm based optimization will be shown to be a useful tool to aid in the design of an electrostatically actuated MEMS resonant mass sensor. However, before the optimization discussion can begin, the issue of how best to model the device must be addressed. The goal of this section is to develop a model that can accurately model an electrostatically actuated micro cantilever beam, including fringing effects, without sacrificing computational efficiency. Three models will be discussed. First, in Section 4.1, a fully-coupled structural-electrostatic analysis will be described and regarded as the benchmark model. Secondly, in Section 4.2, a commonly used simplified model using the parallel plate approximation, previously discussed in Section 3.1.2, will be described. Thirdly, in Section 4.3, a proposed model that decreases the computational time relative to the benchmark model, as well as improving the accuracy in a static deflection analysis will be described. Finally, the performance of the model using the parallel plate approximation described in Section 4.2 and the proposed model described in Section 4.3, will be compared to that of the benchmark for 3 configurations in Section 4.4. For further modeling details in COMSOL, see Section 6.4.2.

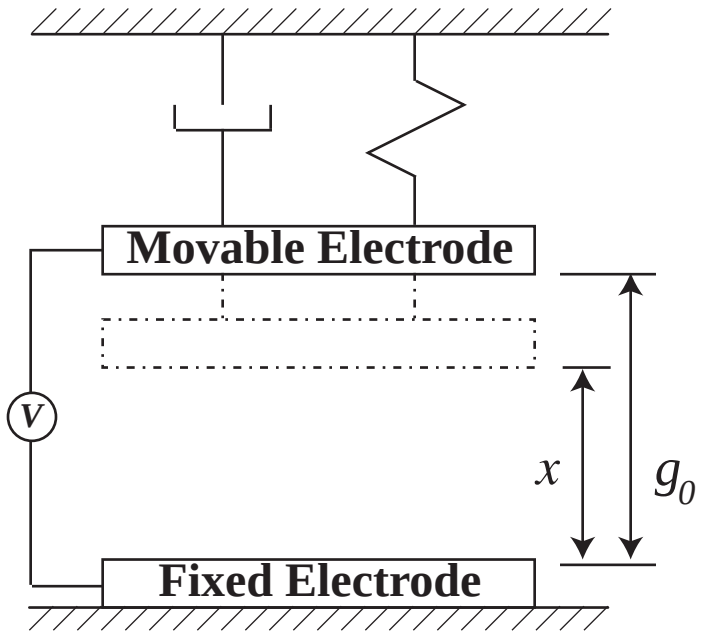

Figure 4.1. General electrostatic MEMS schematic

4.1 Fully-Coupled, Structural-Electrostatic Model

COMSOL is a commercially available finite element modeling software and was chosen for two reasons. First, COMSOL is capable of being accessed from within MATLAB. This capability is valuable when integrating finite element models with optimization programs or control system design. Secondly, COMSOL is capable of combining multiple physics domains in a single model. This capability is valuable in solving a structural analysis coupled with an electrostatic analysis, which is many times required when modeling electrostatic MEMS.

Electrostatic MEMS are actuated by applying a voltage potential difference between

two electrodes, illustrated in Figure 4.1. The electrostatic force between those electrodes attracts a movable electrode towards a fixed electrode. The electrostatic force that pulls the movable electrode is dependent upon the air gap between them. Thus, as the device deforms, so does the electrostatic field, and ultimately the electrostatic force acting on the device. Therefore, a coupled analysis is required to determine the static deflection of a micro device under electrostatic actuation, and the use of COMSOL for this analysis affords this capability.

To perform this analysis in COMSOL, 3 applications are required:

1. 3D Solid, Stress-Strain (SMSLD),

2. Deformed Mesh (ALE), and

3. Electrostatics (EMES).

The problem extends from an example in reference (122). The EMES application solves for the potential, V, in the air gap between the two electrodes, defined by Eq. 4.1. This solution corresponds to Eq. 2.17 in Section 2.1, however, the notation in this section is converted to be the same used by COMSOL. The solution to Eq. 4.1 is used to deduce the electrostatic forces, defined by Eq. 4.2 acting on the movable electrode (123), where $\vec{E}$ is the electric field vector, $\vec{D}$ is the electric displacement vector and $\vec{n}$ is the outward normal vector.

$$-\nabla \cdot (\epsilon_0 \cdot \nabla V) = 0 \tag{4.1}$$

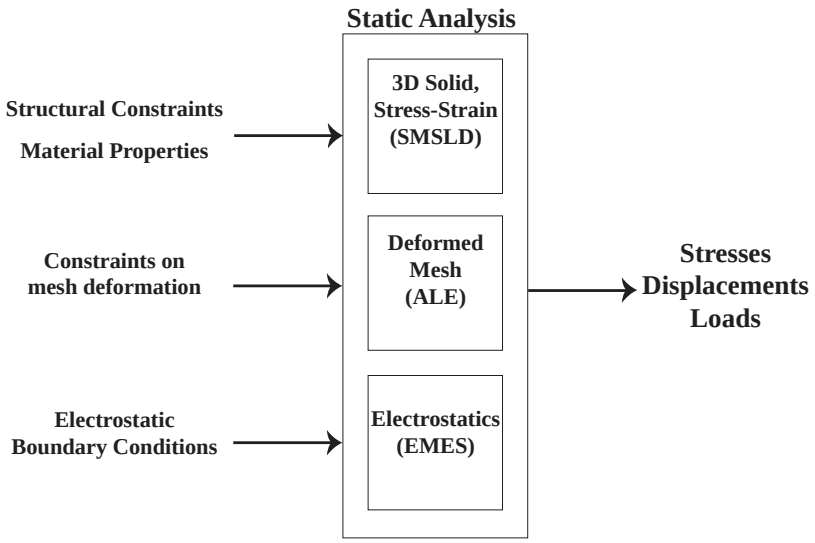

Figure 4.2. Schematic for the fully-coupled, structural-electrostatic model in COMSOL

$$\vec{F_{es}} = -\frac{1}{2}(\vec{E} \cdot \vec{D})\vec{n} + (\vec{n} \cdot \vec{E})\vec{D}^T \tag{4.2}$$

These equations are solved using the locations defined in the ALE application, whose mesh deforms according to the structural deformation of the device computed in the SMSLD application. The SMSLD application solves for the deformation using the principle of virtual work, assuming the external forces acting on the domain, in this case the electrostatic forces acting on the device, are equal to the internal strains, and that the variation of the virtual work is equal to zero, as shown in Eq. 4.3 (123). Figure 4.2 illustrates the solution sequence of the fully-coupled, structural-electrostatic analysis.

$$\delta W = 0 \tag{4.3}$$

The benefit of the fully-coupled, structural-electrostatic analysis over a non-coupled analysis is an improvement in accuracy, since the electrostatic forces changes as a function of the deformation. For this reason, the coupled analysis is used as the benchmark model. A disadvantage of the coupled analysis is the computational inefficiency. This becomes an important limitation if the model is to be used in both genetic algorithm optimization and control system design. The remainder of Chapter 4 explores two methods to combat this negative attribute.

4.2 Parallel Plate Approximation Model

A common simplification when modeling electrostatic MEMS is to work under two assumptions. The first assumption is that the two electrodes are rigid bodies and remain parallel throughout the deformation. The second assumption is that the length and width of the electrodes is much greater than the air gap dimension. As described in Section 3.1.2, these two assumptions lead to the statement that, at any position near the center of the electrodes, the electric scalar potential varies only in the direction normal to the plates, and thus, the electrostatic field is uniform. The two charged plates then represent a parallel plate capacitor, for which the capacitance, C, is approximated by Eq. 3.7. The approximate electrostatic force can be computed directly from the capacitance equation given in Eq. 4.4, where A is the area of the electrodes, V is the potential difference between the two electrodes, g is the air gap between the electrodes and ϵ_0 is the permittivity of free space.

$$F_{es} = \frac{1}{2}\frac{\partial C}{\partial g}V^2 = \frac{1}{2}\frac{\partial}{\partial g}\left(\frac{\epsilon_0 A}{g}\right)V^2 = -\frac{\epsilon_0 A V^2}{2g^2} \tag{4.4}$$

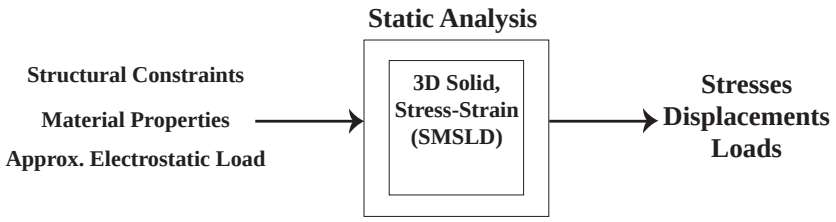

Figure 4.3. Schematic for the parallel plate approximation model in COMSOL

The parallel plate approximation model is also implemented in COMSOL, however, since the electrostatic force acting on the device is closed-form, only the SMSLD application is required. Figure 4.3 illustrates the solution sequence of the parallel plate approximation model. The model is implemented by applying a boundary load equivalent to the approximate electrostatic force to any material area of the device that is located directly across the air gap from an actuation electrode. This implies that any area of the device that is not located directly across from an actuation electrode is not subject to any loading, even if fringing forces exist. One can propose that the configuration for which the parallel plate approximation model performs the best is one where all of the device material is located directly across the air gap from all of the actuation electrodes. Similarly, one can also propose that the configuration for which the parallel plate approximation model performs most poorly is one where there is no overlapping area of the device material and the actuation electrodes, such that any deformation of the device is due purely to fringing forces.

The advantage of a closed-form solution for the electrostatic force is that it de-couples the analyses, significantly reducing the solution time. However, for this improvement in computational efficiency, accuracy for some configurations is sacrificed. The accuracy of the parallel plate approximation model depends greatly on the configuration of material

distribution and electrode configurations. For the application of genetic algorithm based optimization, the model used must be able to accurately compute the static deflection for all configurations. Section 4.4 will illustrate the shortcomings of using this model for genetic algorithm based optimization and the capability of the proposed model described in Section 4.3 to handle these configurations with improved accuracy, while reducing the solution time relative to the benchmark model.

Alternatively, Section 3.1.3 reviews published formulas for approximating the capacitance, including fringing effects, between two electrodes held at a potential difference. These approximations are only valid for particular geometries, none of which encompass all of the geometries possible for the genetic algorithm based optimization problem.

4.3 Interpolated Force Model

A model is presented that approximates the electrostatic forces, including fringing, without solving the coupled analysis described in Section 4.1. The model will be referred to as the interpolated force model and consists of two steps. First, the electrostatic problem, using the EMES application in COMSOL, is solved at specified air gaps. The electrostatic load on each geometric face of the movable electrode is tabulated. Secondly, the structural problem, using the SMSLD application in COMSOL, is solved. In this part of the model, the load on each geometric face of the movable electrode is taken from a look-up table generated in the first part of the analysis. The look-up tables specify the electrostatic load for each domain with material in the device, as a function of the instantaneous gap. The instantaneous gap is defined by the difference between the initial air gap at zero actuation and the

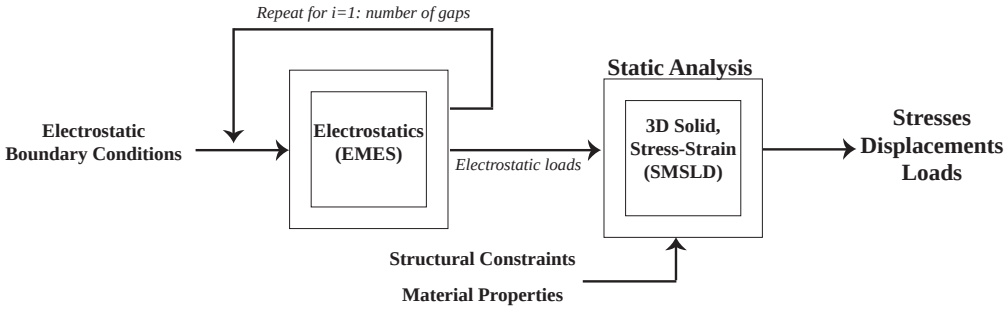

Figure 4.4. Schematic for the interpolated force model in COMSOL

deflection. Figure 4.4 illustrates the solution sequence of the interpolated force model.

The benefit of the interpolated force model is that it affords the capability of expressing the electrostatic force as a closed-form function of the gap, eliminating the need to solve the fully-coupled, structural-electrostatic analysis. The computational efficiency is superior the parallel plate approximation model since the electrostatic problem must be solved multiple times in addition to the structural problem; however, the solution time is reduced relative to the fully-coupled model.

4.4 Model Performance in a Static Deflection Analysis

The modeling techniques are evaluated for a static deflection analysis of a MEMS resonant mass sensor by computing the static deflection of the configuration with an applied voltage of 100 volts. The sensor is a fixed-free cantilever beam composed of poly-silicon. Further details of device composition and operation are discussed in Chapter 6.

Three different sensor configurations are used to test the performance of the parallel

plate approximation model and the interpolated force model relative to the benchmark model. The 3 configurations are illustrated in Figures 4.5(a)-(c). Note, the configurations shown are before the symmetry constraint is imposed. The configurations illustrated are symmetric about the lower horizontal axis. The first configuration, illustrated in Figure 4.5(a), is a scenario for which one would expect the parallel plate approximation model to perform its best. This configuration is close to two parallel plates. The second configuration, illustrated in Figure 4.5(b), is a scenario for which one would expect the parallel plate model to perform poorly. The deformation is due purely to fringing forces, since there is no actuation electrode located directly across the gap from the device material. The third configuration, illustrated in Figure 4.5(c), is a configuration produced during a genetic algorithm optimization run. This configuration was chosen as it is a typical configuration the optimization process must analyze. Figure 4.5(d) illustrates a legend corresponding to the 3 configurations. This legend will be used throughout the remainder of this document for describing the material distribution and the electrode configurations in the design space.

Figure 4.6 and Figure 4.7 describe the performance of the parallel plate approximation model and the interpolated force model for configuration 1. Figure 4.6 illustrates the percent error in applied load for each domain with material. The maximum error in applied load using the parallel plate approximation model is 3.9% and the maximum error in applied load using the interpolated force model is 2.2%. Figure 4.7 illustrates the percent error in static deflection for geometry corners of domains with material. The maximum error in deflection using the parallel plate approximation model is 1.6% and the maximum error in deflection using the interpolated force model is 0.88%.

Figure 4.8 and Figure 4.9 describe the performance of the parallel plate approximation model and the interpolated force model for configuration 2. Figure 4.8 illustrates the per-

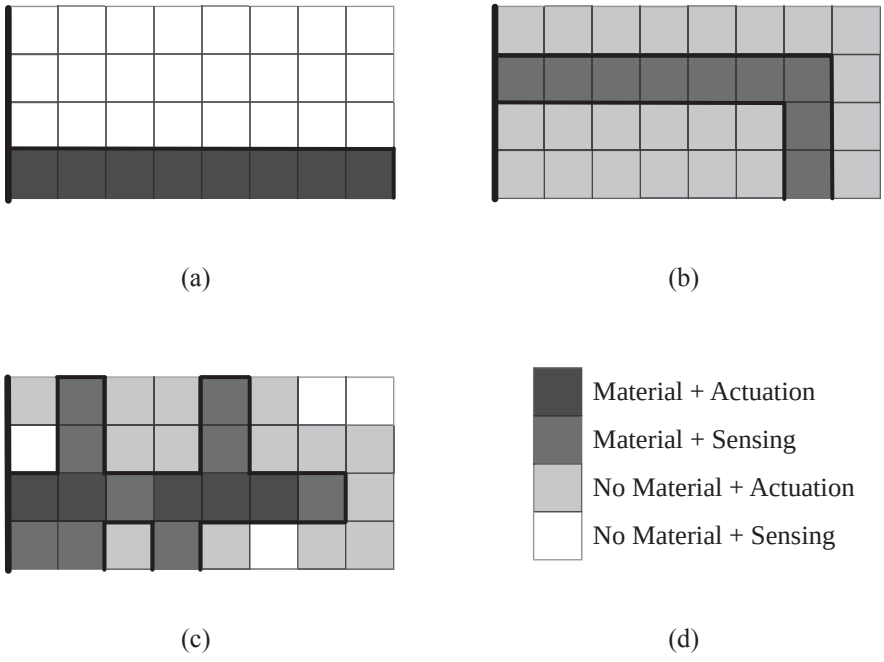

Figure 4.5. (a) Configuration 1 - Best case configuration for the parallel plate approximation model; (b) Configuration 2 - Worst case configuration for the parallel plate approximation model; (c) Configuration 3 - Typical configuration for optimization; (d) Material distribution and electrode configuration legend

cent error in applied load for each domain with material. The maximum error using the interpolated force model is 13%. The parallel plate approximation model has infinite error in applied loads for domains with material and sensing, represented by a value of 100% in the plot. Figure 4.9 illustrates the percent error in static deflection for geometry corners of domains with material. The maximum error in deflection using the interpolated force model is 2.9%. The parallel plate approximation model has infinite error in deflection since the applied load is zero for this configuration.

Figure 4.10 and Figure 4.11 describe the performance of the parallel plate approximation model and the interpolated force model for configuration 3. Figure 4.10 illustrates the

percent error in applied load for each domain with material. The maximum error using the interpolated force model is 38%. The parallel plate approximation model has infinite error in applied load for domains with material and sensing, represented by a value of 100% in the plot. Figure 4.11 illustrates the percent error in static deflection for geometry corners of domains with material. The maximum error in deflection using the interpolated force model is 18%. The maximum error in deflection using the parallel plate approximation model is 62%.

A second measure of performance is computational efficiency. For the analyses above, the parallel plate approximation model reduces the solution time by approximately 88% relative to the benchmark model. The interpolated force model reduces the solution time by approximately 50% relative to the benchmark model.

Figures 4.6-4.11 show that the parallel plate approximation model can accurately model the static deflection for some electrode configurations, but cannot accurately model others. For the application of genetic algorithm based optimization, the model must be able to handle any configuration generated. The fully-coupled, structural-electrostatic analysis and the interpolated force model both provide this capability, but the interpolated force model has superior computational efficiency.

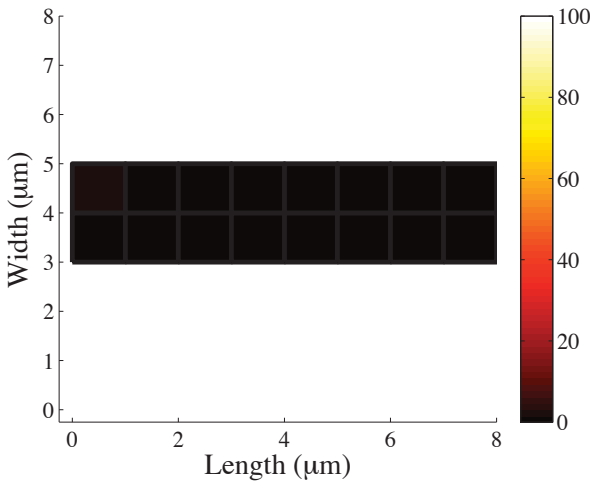

(a)

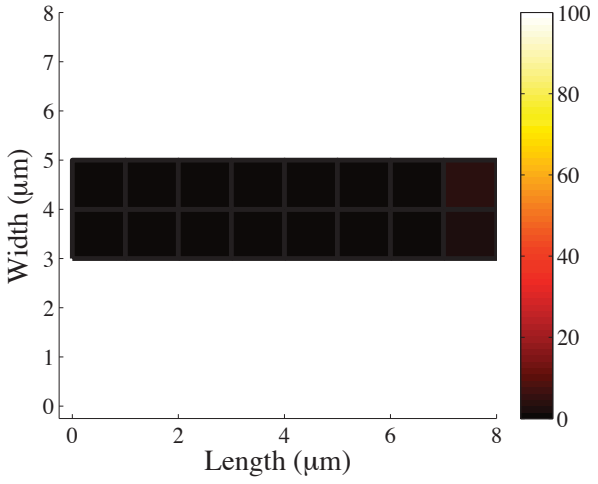

(b)

Figure 4.6. Model performance for configuration 1 (a) Percent error in applied load for each domain with material using the interpolated force model; (b) Percent error in applied load for each domain with material using the parallel plate approximation model

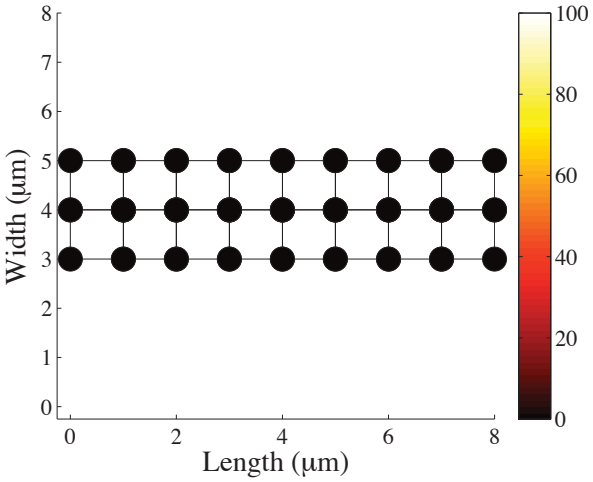

(a)

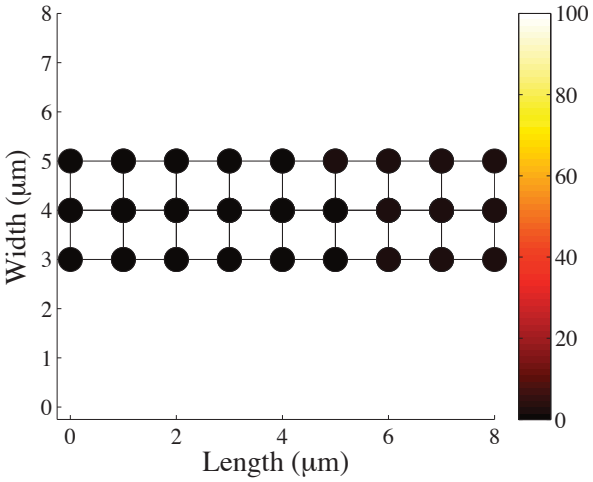

(b)

Figure 4.7. Model performance for configuration 1 (a) Percent error in static deflection for each geometry point corresponding to domains with material using the interpolated force model; (b) Percent error in static deflection for each geometry point corresponding to domains with material using the parallel plate approximation model

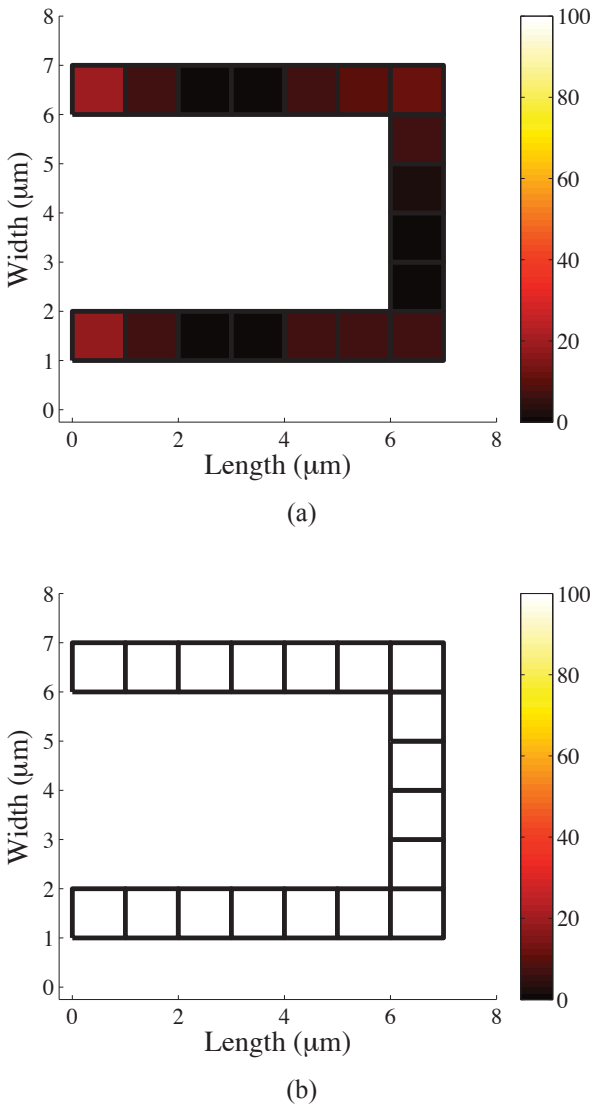

Figure 4.8. Model performance for configuration 2 (a) Percent error in applied load for each domain with material using the interpolated force model; (b) Percent error in applied load for each domain with material using the parallel plate approximation model

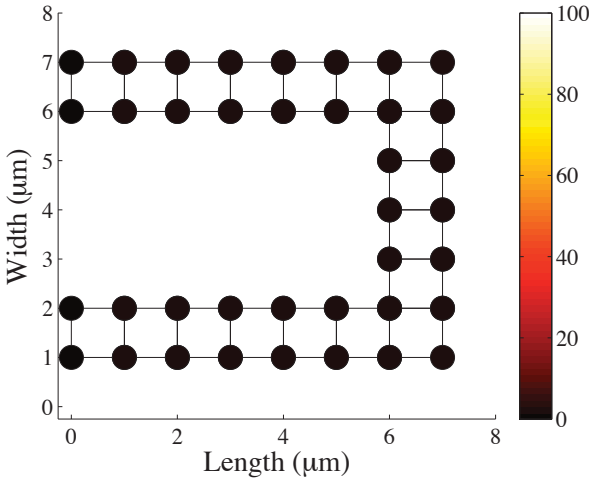

(a)

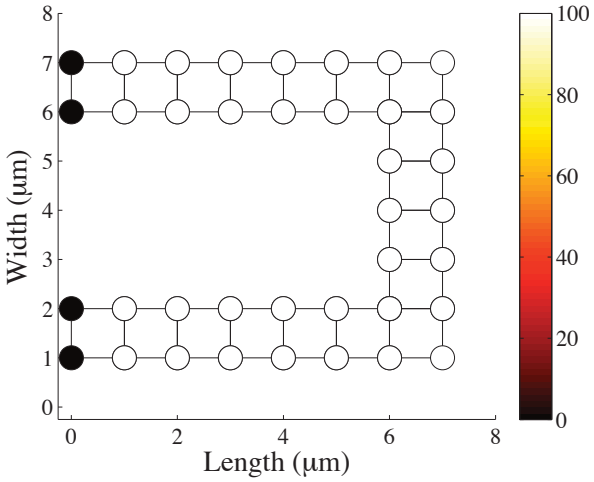

(b)

Figure 4.9. Model performance for configuration 2 (a) Percent error in static deflection for each geometry point corresponding to domains with material using the interpolated force model; (b) Percent error in static deflection for each geometry point corresponding to domains with material using the parallel plate approximation model

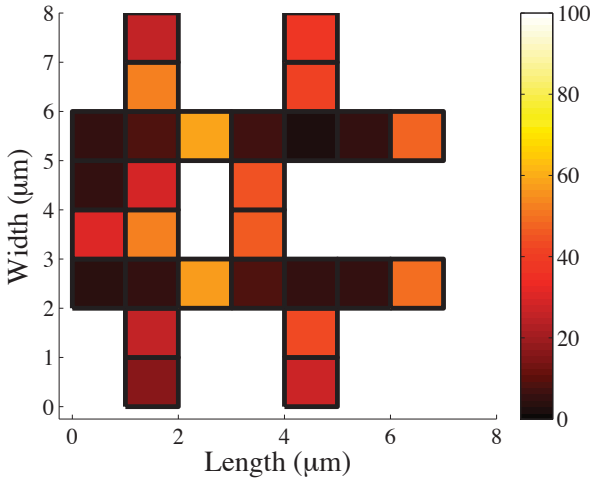

(a)

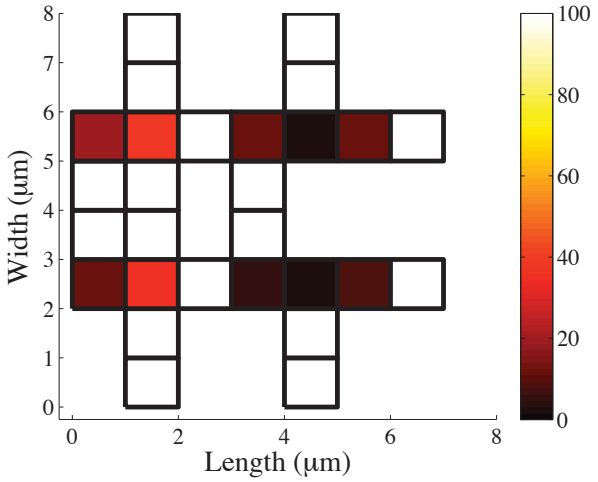

(b)

Figure 4.10. Model performance for configuration 3 (a) Percent error in applied load for each domain with material using the interpolated force model; (b) Percent error in applied load for each domain with material using the parallel plate approximation model

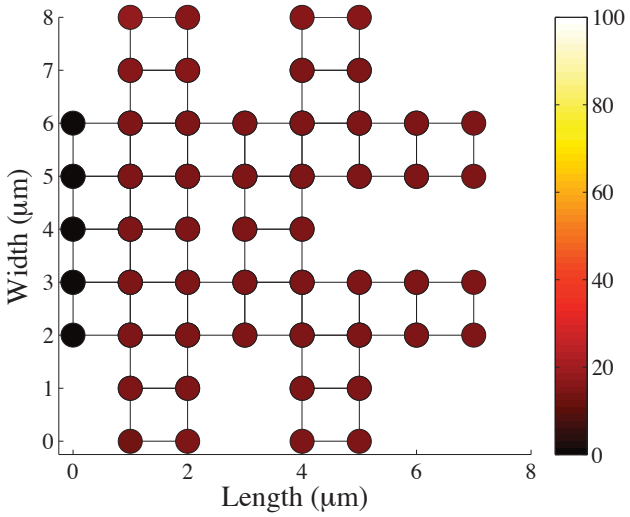

(a)

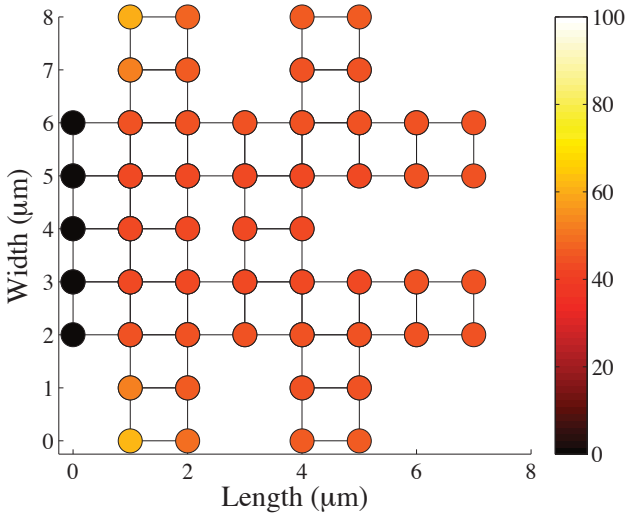

(b)

Figure 4.11. Model performance for configuration 3 (a) Percent error in static deflection for each geometry point corresponding to domains with material using the interpolated force model; (b) Percent error in static deflection for each geometry point corresponding to domains with material using the parallel plate approximation model

5. Input Shaping Techniques for Detection of Mass on a MEMS Mass Sensor

In this section, an alternative sensing technique is proposed for a MEMS mass sensor. MEMS resonant mass sensors are challenged with detecting very small changes in mass that do not significantly alter the performance of the device in the frequency domain. The proposed strategy employs input shaping techniques and makes use of the inherent sensitivity to parameter variation for detection. The strategy is demonstrated in simulation on the sample configuration illustrated in Figure 5.1. The initial gap and the thickness of the beam are 3.0 μm and 3.5 μm, respectively. The applied voltage is set to 100 V. Section 5.1 discusses sensing a small mass change in the frequency domain for this configuration. Section 5.2 introduces a proposed sensing method using input shaping techniques.

A frequency response analysis in COMSOL is used to obtain the response of the configuration for a range of frequencies, before and after mass accumulation. The mass accumulation is modeled as a 0.1% increase in density. The analysis uses the interpolated force modeling method. The response of the configuration is shown in Figure 5.2. Second order parameters are determined from the COMSOL response using a Nelder-Mead simplex direct search method, and are listed in Table 5.1

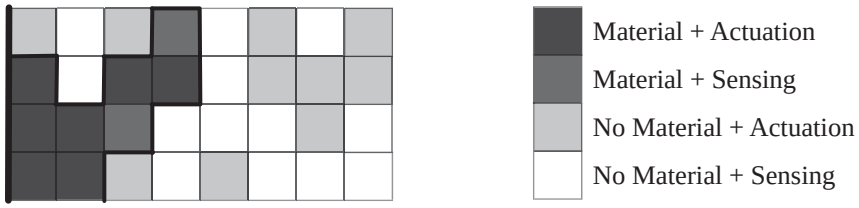

Figure 5.1. (a) Sample configuration for control design; (b) Material distribution and electrode configuration legend

Table 5.1.
Second order system parameters for the system before and after mass accumulation

Parameter	Units	Original System	System plus Mass
Gain, K	–	5.7×10^{-20}	5.7×10^{-20}
Damping Ratio, ζ	–	2.1427×10^{-4}	2.1418×10^{-4}
Natural Frequency, ω_n	rad/s	2.558×10^{6}	2.557×10^{6}

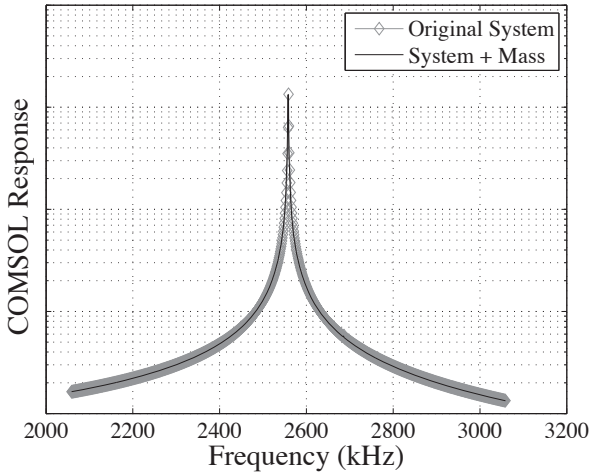

Figure 5.2. Response of the system before and after mass accumulation

5.1 MEMS Resonant Mass Sensing in the Frequency Domain

One method of mass detection is to search for a change in natural frequency of the device, as illustrated by the arrow in Figure 5.3. Referring to Figure 5.2, for this particular configuration and mass accumulation model, the sensor would need to detect a 0.04% change in frequency.

Rather than only investigating a shift in natural frequency, a second frequency domain sensing method investigates changes in both frequency and magnitude using a root mean square (RMS) computation. This particular method is used to compute the fitness value for the optimization described in Chapter 6 and is illustrated by Figure 5.4. Two frequency locations are chosen and the responses of the configuration before and after mass accumulation is recorded for each frequency. Then, the change in response between the two models at each frequency, illustrated by the arrows, is computed and used to calculate the RMS change. Referring to Figure 5.2, for this particular configuration and mass accumulation model, the sensor would need to detect a 0.07 fF change in capacitance.

The two methods for MEMS resonant mass detection described above face some challenges. The first challenge is detecting the relatively small changes in performance that result from minuscule changes in mass. Another challenge is practical implementation in real world environments, since extra signal processing is required on-chip to convert the response to the frequency domain in real time. These negative attributes do not make the sensing methods impossible, but do require special consideration for on-chip signal processing and structure sensitivity.

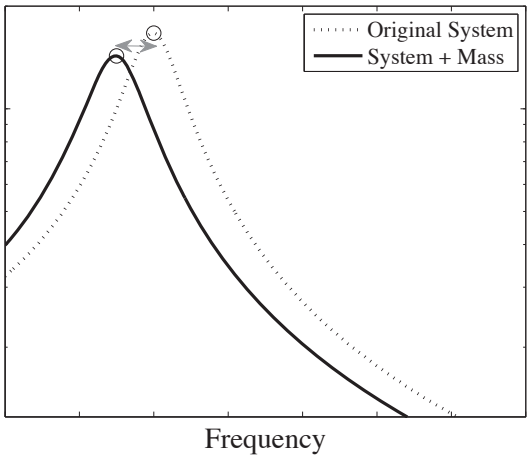

Figure 5.3. Generic response for frequency shift detection of MEMS resonant mass sensors

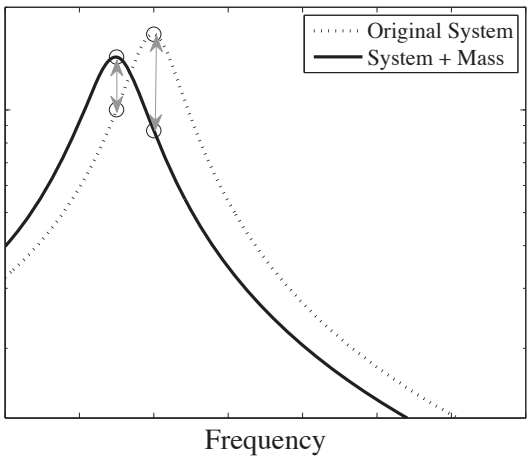

Figure 5.4. Generic response for a 2 point RMS detection of MEMS resonant mass sensors

5.2 MEMS Mass Sensing using Input Shaping Techniques

Input shaping is a control technique that designs a special input waveform to reduce residual vibrations of a system after actuation. The authors in reference (124) step through the design of an input waveform for flexible structures and the work presented below is based upon the method presented in this publication. Input shaping is chosen for sensing for two reasons - (i) input shaping is an open loop control strategy, so the challenges of feedback in micro systems, as discussed in Section 3.3, are eliminated and (ii) input shaping is notably sensitive to model parameters (124). The latter of the two is especially appealing since a change in mass is precisely what the sensor needs to detect.

For this work, a step input is convolved with a set of two impulses. The magnitude of the initial step function is set to unity and the duration of the step is chosen to be 1 μs. One impulse actuates the structure and the second impulse, if timed correctly, cancels the dynamics. If the input waveform is not designed correctly because of an inaccurate estimation of plant parameters, there will be residual vibrations following the actuation. The open-loop block diagram for this sensing technique is illustrated in Figure 5.5.

The open loop response for the sample configuration is shown in Figure 5.6. The residual vibrations are highlighted in Figure 5.6(b). After mass accumulation, the input waveform is no longer perfectly shaped to cancel the dynamics.

Figure 5.5. Open-loop block diagram of a system with a shaped input

Using input shaping as a sensing technique for a MEMS mass sensor is advantageous due to eliminating the need for feedback and the sensitivity to parameter changes. Also, since the timing of the response is known, a time-dependent gain could be added to amplify the residual vibrations for easier detection. The challenge of this type of feedback is the requirement of exact plant parameters for the input waveform design. However, because of the open-loop structure of the system, this drawback could be mitigated with the design of a self-calibration technique using learning control, using the method presented in Chapter 7.

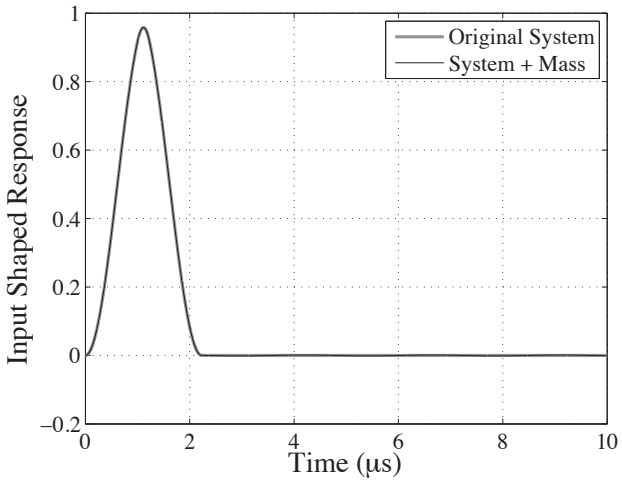

(a)

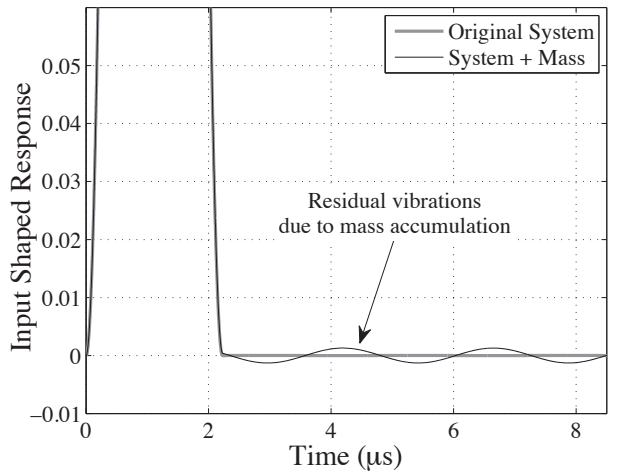

(b)

Figure 5.6. (a) Open-loop response of the system before and after mass accumulation for a shaped input; (b) (Zoom View)

6. Genetic Algorithm Optimization for MEMS Sensor Design

In this chapter, the use of genetic algorithm based optimization for the design of a MEMS resonant mass sensor will be investigated. The resonant micro sensor is an electrostatically actuated, fixed-free, poly-silicon micro beam with capacitive sensing capabilities. The sensor has a polymer coating to which airborne contaminants attach, causing a mass change. The objective of the optimization is to assign a combination of sensor dimensions, material and electrodes, such that the largest average change in capacitance is sensed for an accumulated change in mass. Figure 6.1 describes the flow of the optimization.

Section 6.1 will describe the design space and arrangement of the design variables. The structure of the optimization will be discussed in Section 6.2 and geometry considerations are given in Section 6.3. Section 6.4 will define how to calculate the fitness value for each configuration, given by step 2 in Figure 6.1. Finally, Section 6.5 will present the results of several sample optimization runs.

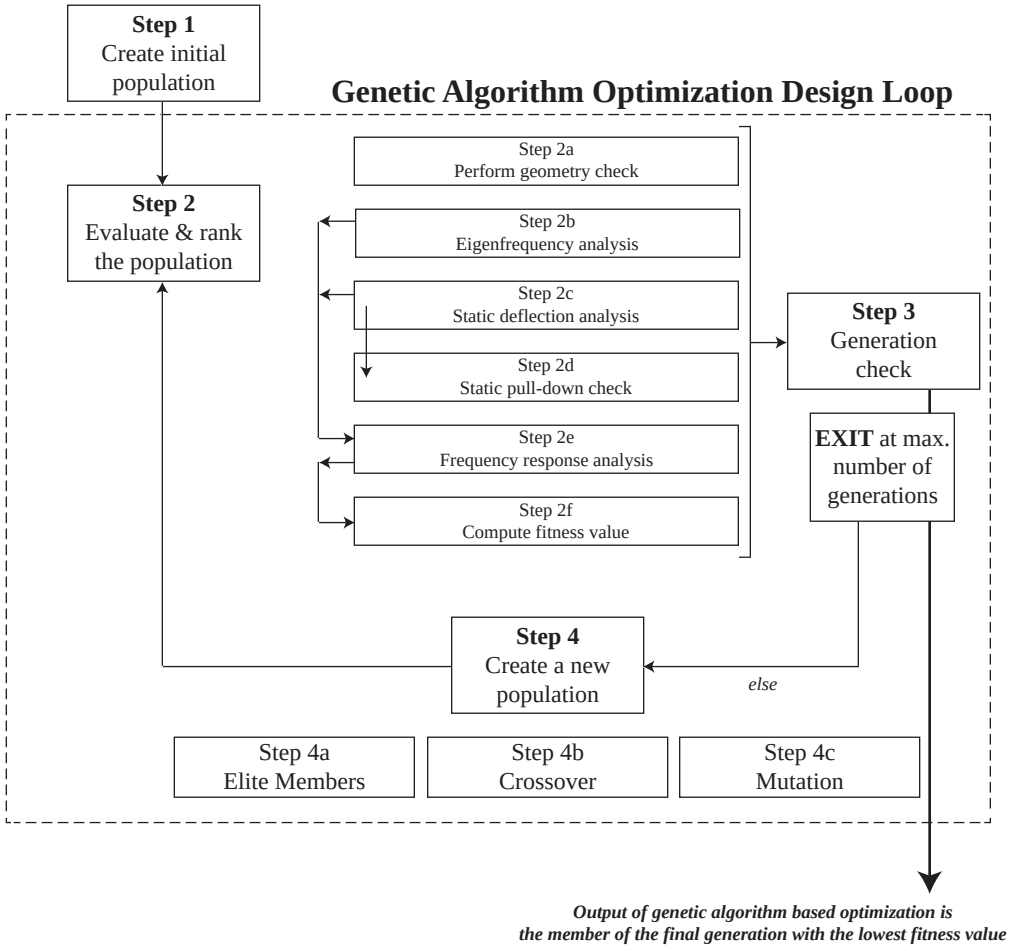

Figure 6.1. Process flow of the optimization integrating the use of COMSOL and genetic algorithms

6.1 Design Variables

Each design configuration is defined discretely by a bit string. The physical design space is divided into grid-like regions. The design space for a sample configuration is shown in Figure 6.2. The optimization is constrained to symmetric designs only. This reduces the total design space by half and eliminates the role of torsional modes. Thus the bit string only needs to define half of the configuration. Assume that the ranges and values for the initial gap, actuation voltage and beam thickness are those given in Table 6.1.

Two bits are assigned to each region in the design space. The first bit determines if there is material in that region. The second bit determines if the electrode in that region is used for sensing or actuation. An additional set of bits describes the magnitude of the initial gap, applied voltage and beam thickness. For examples in this work, assume 2 bits represent the range for each of the miscellaneous parameters. For the case illustrated in Figure 6.2, the configuration and its identifying bit string are broken down and described in Figure 6.3.

Table 6.1.
Miscellaneous parameter ranges and values

Parameter	Units	Max.	Min.	Value
Initial Gap	μm	4.0	2.5	2.5
Applied Voltage	V	100	40	100
Beam Thickness	μm	4.0	2.5	3.5

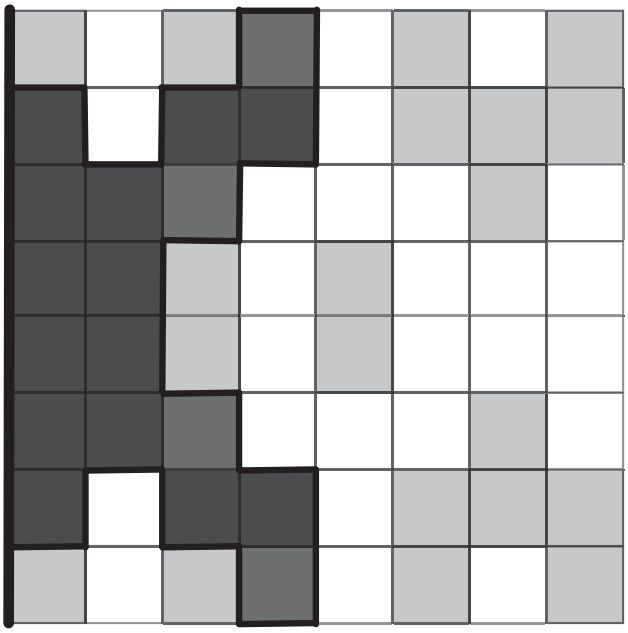

(a)

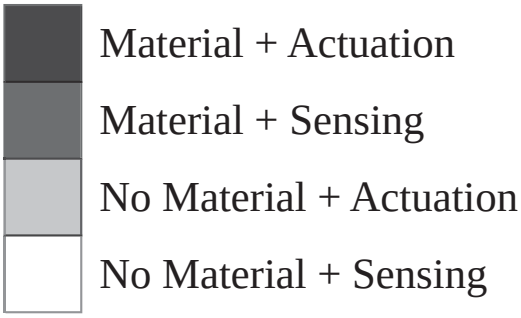

(b)

Figure 6.2. (a) Sample configuration for a MEMS resonant mass sensor; (b) Material distribution and electrode configuration legend

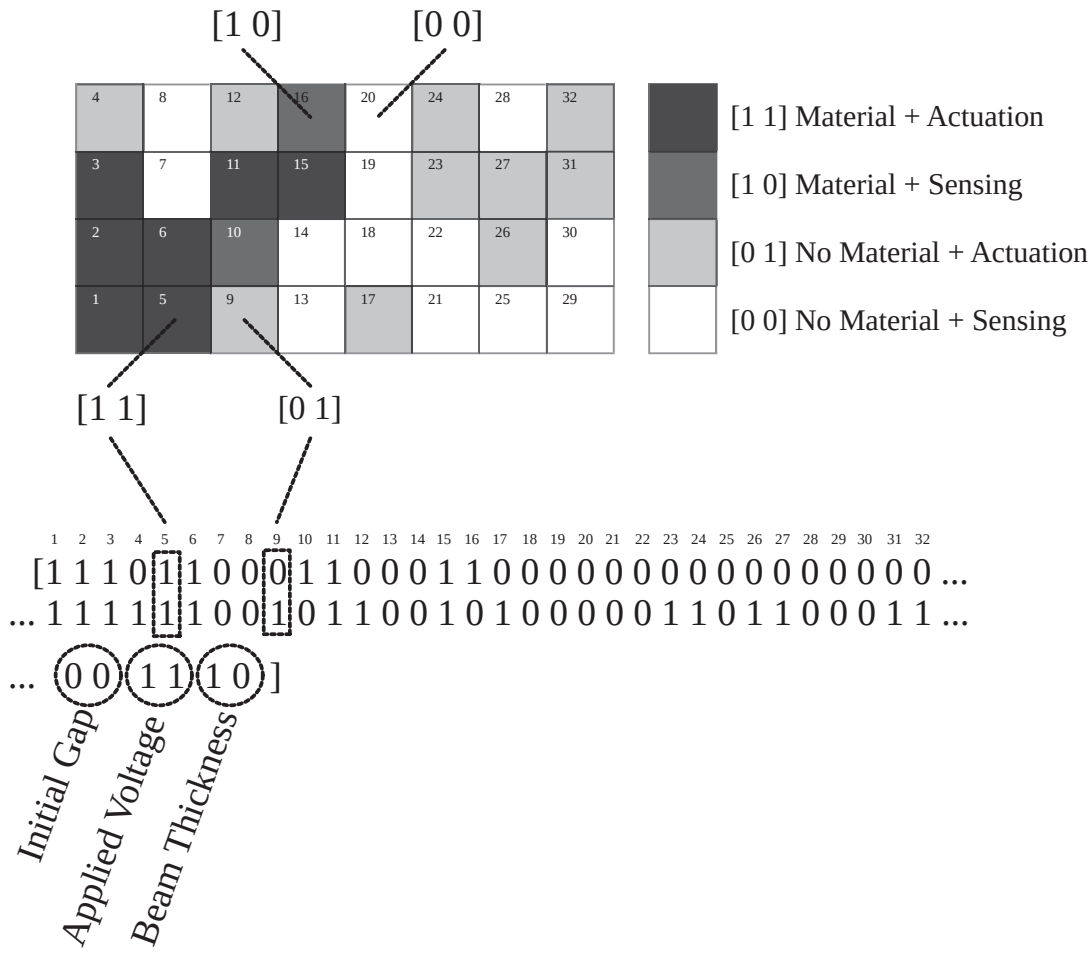

Figure 6.3. Sample configuration with identifying bit string for a MEMS resonant mass sensor

6.2 Genetic Algorithm Structure

The general structure for genetic algorithm based optimization was discussed in Section 2.2. The optimization protocol used in this work follows this structure and the methods for scaling, selection, elite members, crossover and mutation are described below. The optimization in this work does not include migration.

The fitness value is scaled after each generation is ranked and the fitness scale in this work is based upon the rank of the configuration. The best member in each generation has a scaled fitness value of unity. The second best member has a scaled fitness value of two, etc. The worst member of each generation has a scaled fitness value equal to the size of the population.

The parent selection process is a stochastic uniform method. A line is generated and each member of the current generation corresponds to a segment of that line proportional to its scaled fitness value. The selection algorithm progresses along the line, assigning a parent from each segment it stops at. The selection algorithm advances in steps of equal length.

Together, elite members and the crossover fraction, determine how many children are produced by each of the three processes - elite members, crossover and mutation. For this work, elite members is set to a value of two, indicating that the two best configurations automatically survive to the ensuing generation. The crossover fraction determines what percentage of the children, excluding those generated by elite members, will be created using crossover. The remaining population is generated through mutation. In this work, the crossover fraction is set to 0.8, indicating that 80% of the children not generated by elite

Table 6.2.
Scattered crossover example

Parent 1	[111000]
Parent 2	[000111]
Binary Array	[101000]
Child	[101111]

members are created using crossover and 20% are generated through mutation.

The crossover process in this work uses a scattered method. For each child to be generated using crossover, a random binary array, equal in length to each member, is generated. The genes of the child are taken from the first parent for each index corresponding to unity in the binary array and are taken from the second parent for each index corresponding to zero in the binary array. An example of this crossover method is shown in Table 6.2.

The mutation function in this work adds a random number to each gene in the mutation parent. The random number is taken from a Gaussian distribution. The mean of the distribution is zero. The standard deviation at the first generation is assigned to unity, as is the rate at which the mutation decreases. The mutation decreases to zero at the final generation.

6.3 Geometry Considerations for Finite Element Analysis

The evaluation of the fitness function, described in Section 6.4, requires mutliple computations in COMSOL, so this section will describe the geometry used in these analyses.

The geometry is drawn in 3 distinct steps, summarized by the illustrations in Figure 6.4. First, a solid 3D block is drawn to represent each grid-like region of the beam. These regions

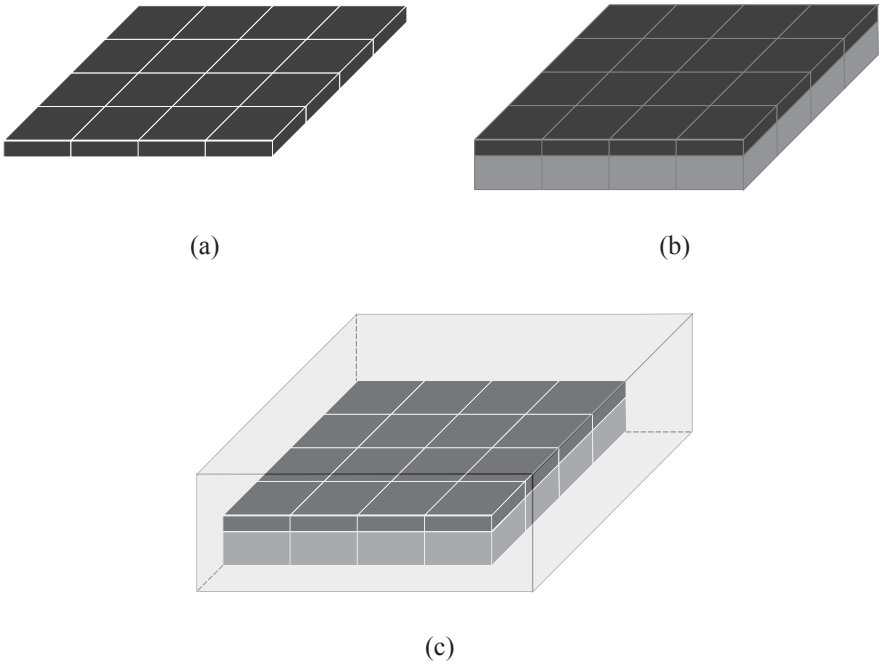

Figure 6.4. (a) Illustration of beam subdomains; (b) Illustration of beam subdomains and electrostatic subdomains; (c) Complete illustration of the geometry in the physical design space

will be referred to as "beam subdomains" and are shown in Figure 6.4(a). Secondly, a solid 3D block is drawn to represent the air gap beneath each of the beam subdomains. These regions will be referred to as "electrostatic subdomains" and are shown in Figure 6.4(b). Finally, a larger block is drawn to encompass the entire beam and the air gap to allow for evaluation and visualization of the electrostatic field around the device. The entire physical design space is illustrated in Figure 6.4(c). Drawing each individual region of the design space allows each region to be assigned the necessary boundary conditions defined by the identifying bit string.

The total number of regions in the geometry is dependent upon the number of rows and columns specified. The results in this work use 8 rows and 8 columns, after symmetry is

imposed. The length and width of each region is specified at the beginning of the program and remains consistent throughout the design process. The results in this work assigned each subdomain to be 10 μm long and 10 μm wide.

Special consideration for disconnected geometries must be made when using discrete topology optimization. Geometry configurations with no material elements on the fixed-end, or configurations with floating portions of material are considered invalid designs. Examples of valid and invalid geometries are illustrated in Figure 6.5, where material domains are represented by shaded domains.

A special geometry creation function assures only connected geometries enter the genetic algorithm optimization in the initial population. The function initially places material is domains 1, 2 and 5, as illustrated in Figure 6.3. The material in these domains exists in every configuration of the initial population, but these domains are not constrained to have material after crossover or mutation. Next, a random number between zero and unity is generated for each adjacent neighbor using a standard uniform distribution. If the number rounds to unity, that neighbor is assigned material. if the number rounds to zero, that neighbor remains a hole. This process is repeated until all of the adjacent edges of the domain have neighbors without material or the configuration has reached a design space border.

Disconnected geometries can still enter the optimization through the crossover and mutation functions. Thus, a geometry check is performed to evaluate each configuration before fitness evaluation. The geometry check first looks for a domain along the fixed edge with material. If none is found, the geometry is deemed invalid. If one is found, each adjacent neighbor also with material is cataloged. Once all of the adjacent neighbors are examined, each neighbor with material is cycled through in a similar manner. The process continues until there remains no new neighbor with material. The cataloged geometry is then com-

pared to the original geometry. If the two geometries do not match, that indicates there is additional material disconnected to the base and the geometry is invalid. If the two geometries match, the configuration is valid and the process proceeds to the fitness evaluation. Invalid geometries are discarded and replaced by a new geometry generated by the initial population creation function.

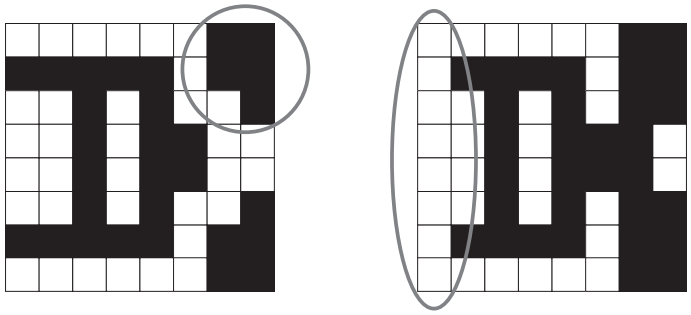

(a) (b)

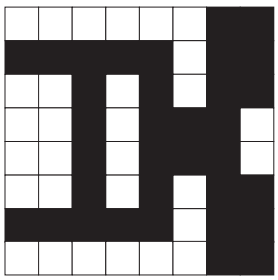

(c)

Figure 6.5. (a) Example of an invalid geometry configuration with disconnected sections of material; (b) Example of an invalid geometry configuration with no material at fixed-end; (c) Example of a valid geometry configuration

6.4 Fitness Function Evaluation

The goal of the fitness function is to increase the averaged sensed change in capacitance for a given mass accumulation of the device. This section will investigate the details of that computation, as outlined by step 2 in Figure 6.1. Step 2 requires 3 models in COMSOL - an eigenfrequency analysis, static deflection analysis and a frequency response analysis. The boundary conditions and details of the 3 models will be discussed in Sections 6.4.1-6.4.3, respectively. Section 6.4.4 will describe the computation of the fitness value.

6.4.1 Eigenfrequency Analysis

The fitness evaluation investigates the change in natural frequency of the sensor after a mass change. Thus, the first natural frequency of the device must be computed before and after mass accumulation using an eigenfrequency analysis, corresponding to step 2b in Figure 6.1. The SMSLD application in COMSOL is used. The mass change of the device is modeled as a 0.1% increase in density. A function developed in MATALB is used to compute the indices for proper assignment of subdomain and boundary conditions for each configuration.

Table 6.3 summarizes the subdomain settings to be used in this model. Beam subdomains with material are active in this application and are assigned poly-silicon material properties. The remaining subdomains are inactive in this analysis.

The boundary settings for this analysis are illustrated in Figure 6.6. The boundaries along the fixed edge of beam subdomains with material are assigned a fixed constraint. The remaining boundaries of the beam subdomains with material are assigned a free condi-

Table 6.3.
COMSOL subdomain settings for the eigenfrequency analysis

	Beam Subdomains	**Electrostatic Subdomains**
Material + Actuation or *Material + Sensing*		
SMSLD	Active/Poly-Silicon	Inactive
No Material + Actuation or *No Material + Sensing*		
SMSLD	Inactive	Inactive

tion. All other boundaries, those belonging to electrostatic subdomains or beam subdomains without material, are inactive in this analysis.

The natural frequency of the device, before and after mass accumulation, is recorded and used in the frequency response analysis, to be discussed in Section 6.4.3.

6.4.2 Static Deflection Analysis

Subsequent to the natural frequency computations in Section 6.4.1, a stationary analysis for the static deflection of the beam is performed for the assigned actuation voltage. This analysis corresponds to Step 2c in Figure 6.1.

The static analysis is implemented in COMSOL differently for each of the models described in Chapter 4. The fully-coupled structural-electrostatic analysis utilizes the SMSLD, EMES and ALE applications. A function developed in MATLAB computes the indices for proper assignment of subdomain and boundary conditions in each application.

Table 6.4 summarizes the subdomain settings to be used in this model for each application. Beam subdomains with material are active in the SMSLD application with the material properties of poly-silicon, assigned a mesh deformation in the ALE application consistent

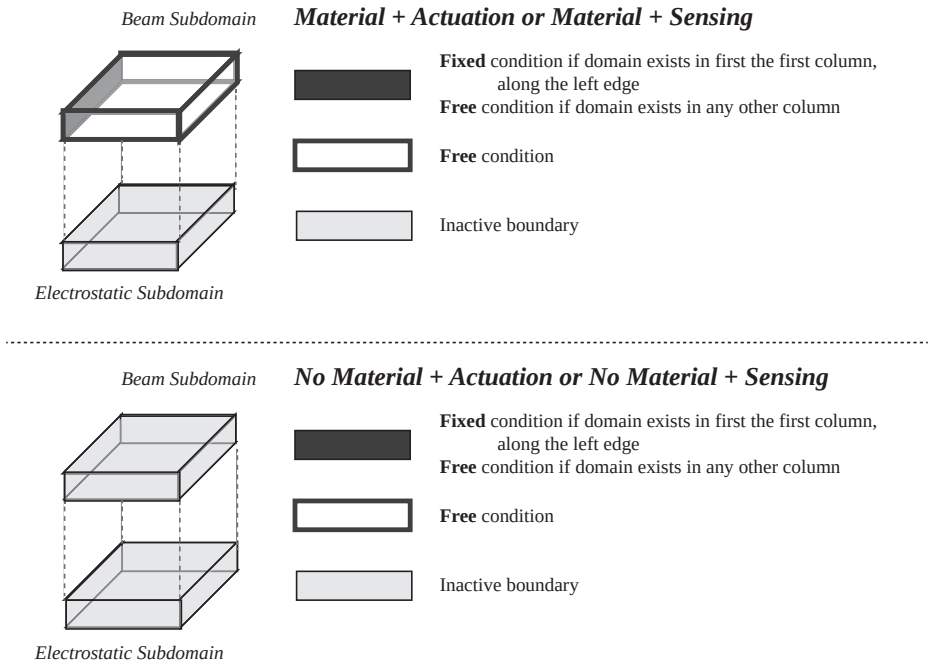

Figure 6.6. COMSOL boundary settings in the SMSLD application for the eigenfrequency analysis

with the physics from the output of the SMSLD application and are inactive in the EMES application. The remaining subdomains are inactive in the SMSLD application, allowed free mesh deformation in the ALE application and active with the material properties of air in the EMES application.

For the parallel plate approximation model and the interpolated force model, the physics are uncoupled with a closed-form expression for the electrostatic force. In the case of these two models, only the SMSLD application is used. Table 6.5 summarizes the subdomain settings to be used in this model for each application. Beam subdomains with material are active and assigned poly-silicon material properties. The remaining subdomains are inactive in this analysis.

Table 6.4.
COMSOL subdomain settings for the static deflection analysis using the fully-coupled, structural-electrostatic model

	Beam Subdomains	**Electrostatic Subdomains**
Material + *Actuation* or *Material* + *Sensing*		
SMSLD	Active/Poly-Silicon	Inactive
ALE	Active Physics Induced Deformation	Active Free Deformation
EMES	Inactive	Active/Air
No Material + *Actuation* or *No Material* + *Sensing*		
SMSLD	Inactive	Inactive
ALE	Active Free Deformation	Active Free Deformation
EMES	Active/Air	Active/Air

The boundary settings for each application of the fully-coupled model are illustrated in Figure 6.7-Figure 6.9. In the SMSLD application, boundaries along the fixed edge that represent material are assigned a fixed constraint. Bottom boundaries of beam subdomains with material are assigned an electrostatic load computed by the EMES application. Any remaining boundaries that represent material are assigned a free condition. All other boundaries, those belonging to electrostatic subdomains or beam subdomains without material, are

Table 6.5.
COMSOL subdomain settings for the static deflection analysis using the parallel plate approximation model or the interpolated force model

	Beam Subdomains	**Electrostatic Subdomains**
Material + *Actuation* or *Material* + *Sensing*		
SMSLD	Active/Poly-Silicon	Inactive
No Material + *Actuation* or *No Material* + *Sensing*		
SMSLD	Inactive	Inactive

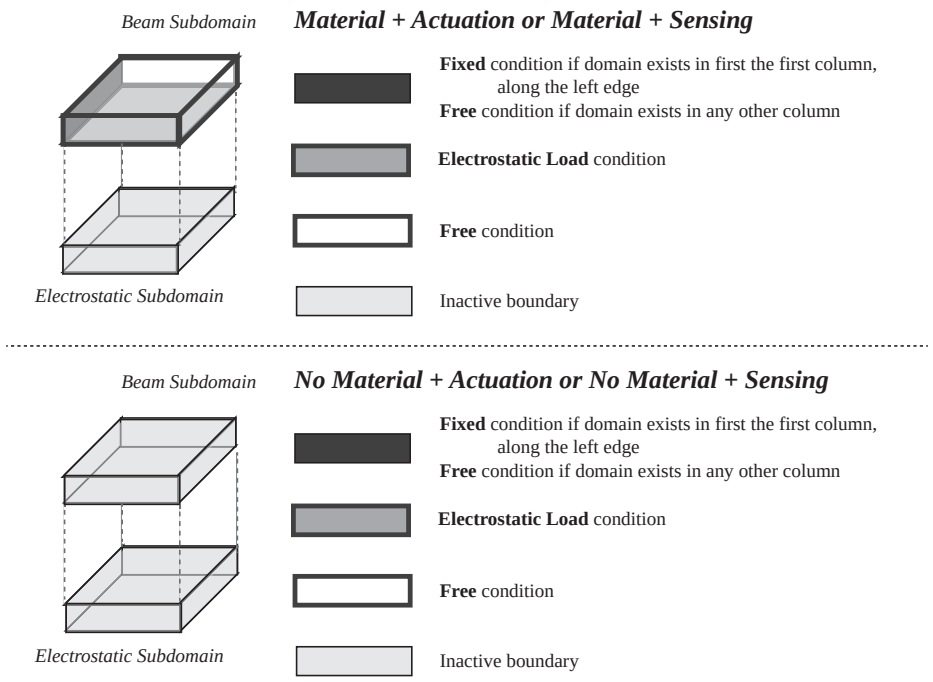

Figure 6.7. COMSOL boundary settings in the SMSLD application for the fully-coupled, structural-electrostatic static deflection analysis

inactive in this analysis. In the EMES application, all bottom surfaces of beam subdomains with material are assigned a voltage potential condition. Also, all bottom surfaces of the electrostatic subdomains that represent actuation are assigned a ground condition. Remaining active boundaries are assigned either a zero charge or continuous condition, depending on the configuration. Beam subdomain boundaries are inactive in this analysis. In the ALE application, all boundaries are active. Any boundary representing material is assigned mesh deformation defined by output of the SMSLD application. Any boundary representing the outer surface of the device or air region is assigned a fixed constraint, not allowing the mesh to deform in those locations. Finally, all remaining boundaries are assigned a free deformation mesh condition.

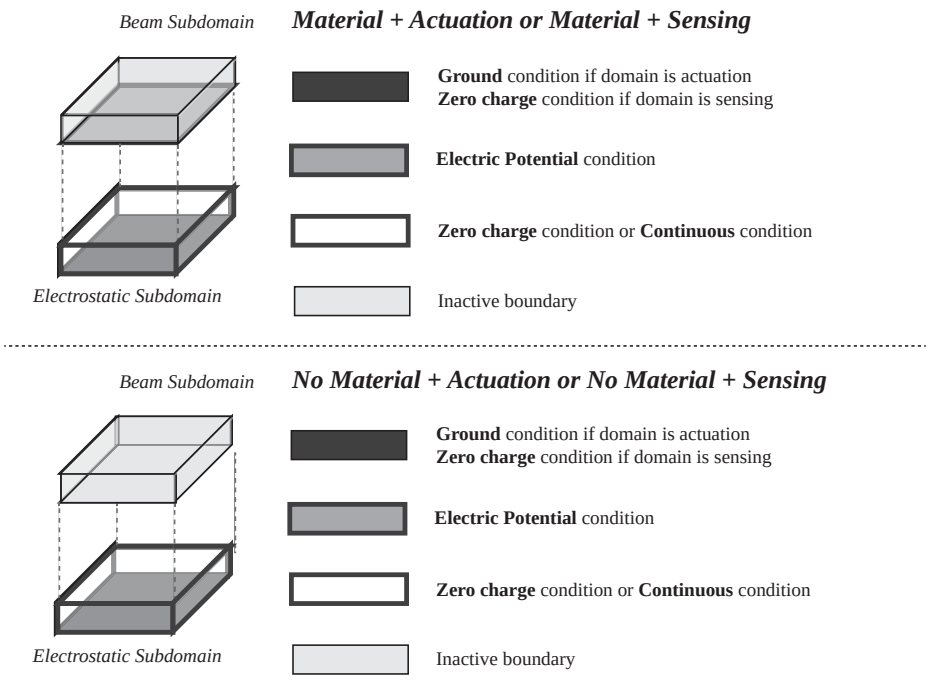

Figure 6.8. COMSOL boundary settings in the EMES application for the fully-coupled, structural-electrostatic static deflection analysis

The parallel plate approximation model and the interpolated force model decouple the analysis through a known expression for the electrostatic loading. Therefore, only the SM-SLD application in COMSOL is used. The boundary settings for the static deflection analysis using the parallel plate approximation model and the interpolated force model are illustrated in Figure 6.10. A fixed constraint is applied to boundaries of the beam subdomains with material along the fixed edge. The bottom surfaces of the beam subdomains with material are assigned a boundary load. Any remaining boundaries that represent material are assigned a free condition. All other boundaries, those belonging to electrostatic subdomains or beam subdomains without material, are inactive in this analysis.

The calculation of the applied electrostatic load differs for the parallel plate approxima-

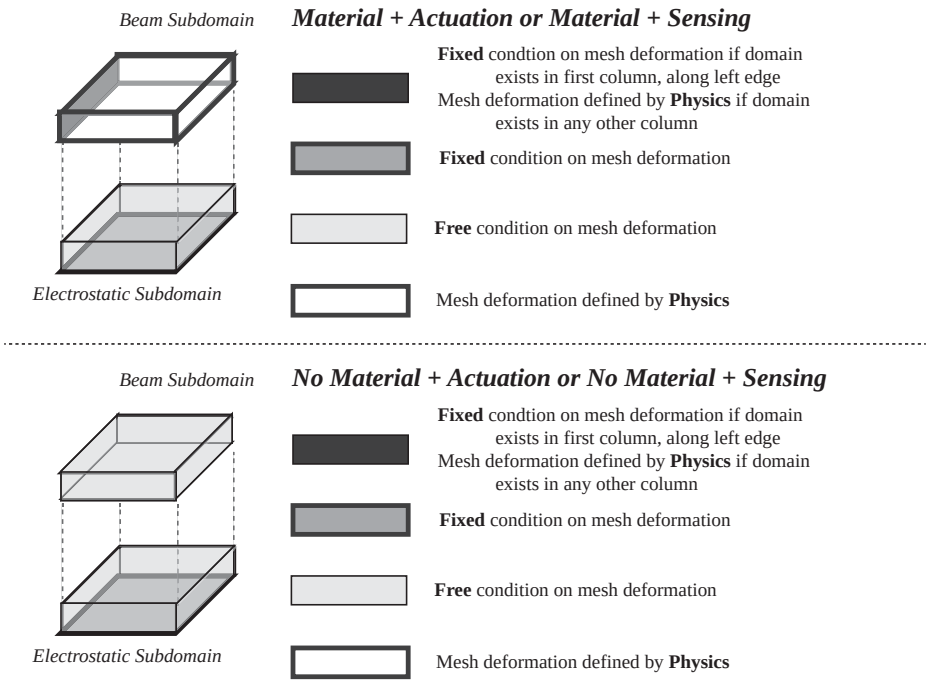

Figure 6.9. COMSOL boundary settings in the ALE application for the fully-coupled, structural-electrostatic static deflection analysis

tion model and the interpoloated force model. For the parallel plate approximationmodel, the load is computed using Eq. 4.4. In the interpolated force model, the boundary load is determined by first solving a number of electrostatic models in the EMES application in COMSOL for specified gaps. The electrostatic force on each boundary is recorded and a look-up table is generated for each boundary. The table is linearly interpolated to form an expression for the electrostatic force on each boundary as a function of the gap. For this work, the electrostatic load is solved for gap values of $g_0 \pm 2$ μm in 0.4 μm increments, where g_0 is the initial gap of the configuration.

The boundary conditions for the electrostatic analysis in COMSOL are illustrated in Figure 6.11. All bottom surfaces of beam subdomains with material are assigned a voltage

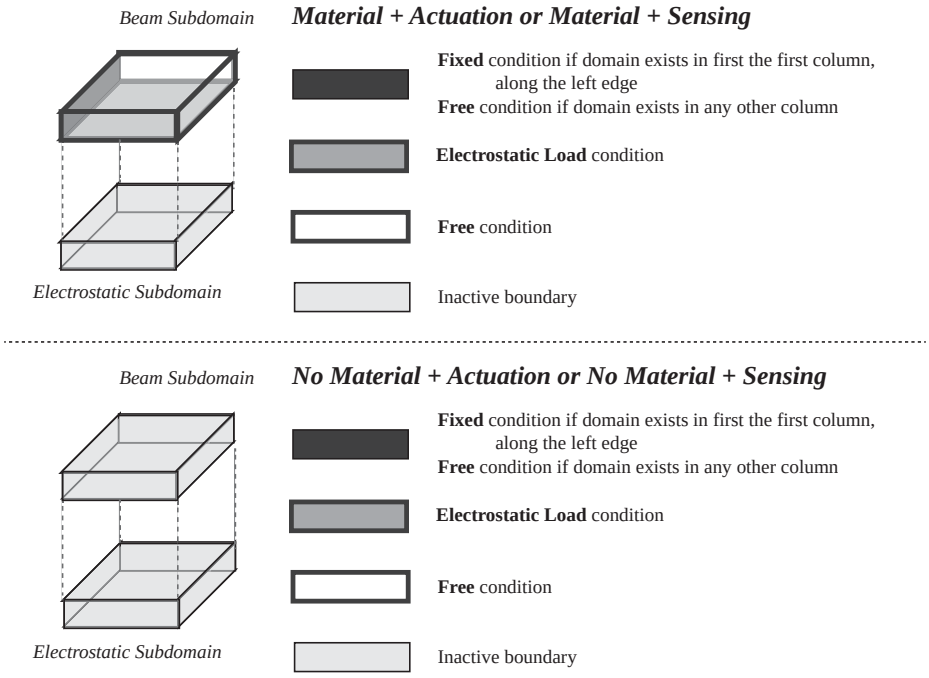

Figure 6.10. COMSOL boundary settings in the SMSLD application for static deflection analysis using either the parallel plate approximation model or the interpolated force model

potential condition. Also, all bottom surfaces of the electrostatic subdomains that represent actuation are assigned a ground condition. Remaining active boundaries are assigned either a zero charge or continuous condition, depending on the configuration. Beam subdomain boundaries are inactive in this analysis.

Parallel plate electrostatic MEMS are subject to an instability called pull-down at approximately one-third of the initial gap. A larger description of pull-down in electrostatic MEMS is given in Section 7.1. In this application, pull-down is not a desirable situation and could potentially cause damage to the sensor. Therefore, a pull-down check is used to detect if the event occurs during the static deflection analysis. Since there is a numerical challenge

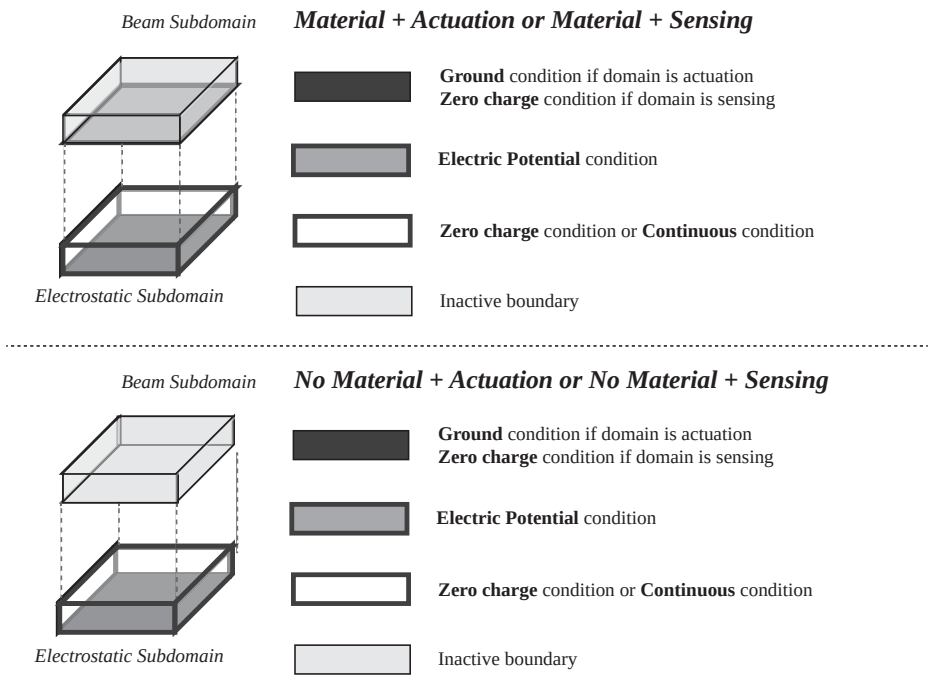

Figure 6.11. COMSOL boundary settings in the EMES application for static deflection analysis using the interpolated force model

with computing displacements exceeding pull-down, COMSOL generates a warning indicating that the solution has not converged. If this occurs, the configuration is flagged and is immediately assigned a high fitness value, and the optimization moves on to evaluating the next member. If pull-down does not occur, two variables are recorded during the static deflection analysis. First, the static deflection for each beam subdomain with material that is located directly across the air gap from a sensing electrode is recorded. Secondly, the electrostatic force acting on each beam subdomain with material is also recorded.

Table 6.6.
COMSOL subdomain settings for the frequency response analysis

	Beam Subdomains	**Electrostatic Subdomains**
Material + *Actuation* or *Material* + *Sensing*		
SMSLD	Active/Poly-Silicon	Inactive
No Material + *Actuation* or *No Material* + *Sensing*		
SMSLD	Inactive	Inactive

6.4.3 Frequency Response Analysis

A change in mass will ultimately affect the frequency response of the sensor. Therefore, a frequency response analysis in COMSOL, using the SMSLD and squeeze-film damping (MMFD) applications is performed next. This analysis corresponds to step 2e in Figure 6.1. The frequency response analysis in COMSOL allows for the computation of the steady-state amplitude of the device when actuated at a specified frequency. The model evaluates the sensor before and after mass accumulation, at both frequencies computed by the eigenfrequency analysis, for a total of 4 solutions. A function developed in MATLAB is used to compute the indices for proper assignment of subdomain and boundary conditions for each configuration.

Table 6.6 summarizes the subdomain settings to be used in this model. Beam subdomains with material are active in this application and are assigned poly-silicon material properties. The remaining subdomains are inactive in this analysis.

The boundary settings for this analysis are illustrated in Figure 6.12-Figure 6.13. In the SMSLD application, boundaries along the fixed edge that represent material are assigned a fixed constraint. Bottom boundaries of beam subdomains with material are assigned a

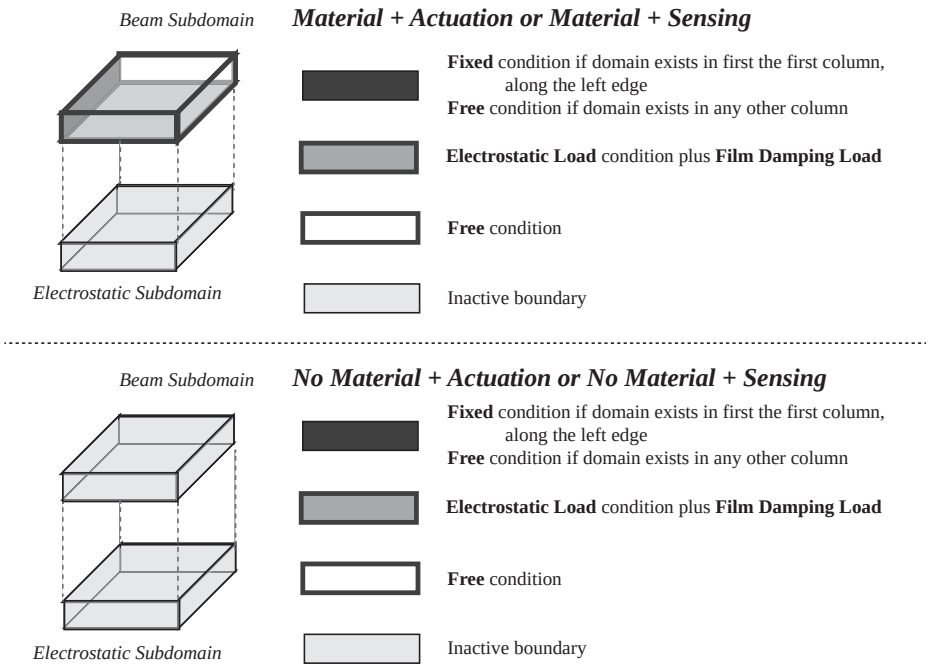

Figure 6.12. COMSOL boundary settings in the SMSLD application for the frequency response analysis

harmonic load. The magnitude of the load is computed as 10% of the electrostatic load plus the squeeze-film damping load computed by the MMFD application. Any remaining boundaries that represent material are assigned a free condition. All other boundaries, those belonging to electrostatic subdomains or beam subdomains without material, are inactive in this analysis. In the MMFD application, all of the bottom surfaces of the beam subdomains with material are assigned a film damping boundary. For this work, the surrounding air pressure is assigned to atmospheric and the initial gap is defined individually according to each configuration.

The steady-state amplitude of oscillation, w_{fr}, for each beam subdomain with material and located directly across the air gap from a sensing electrode is recorded. The absolute

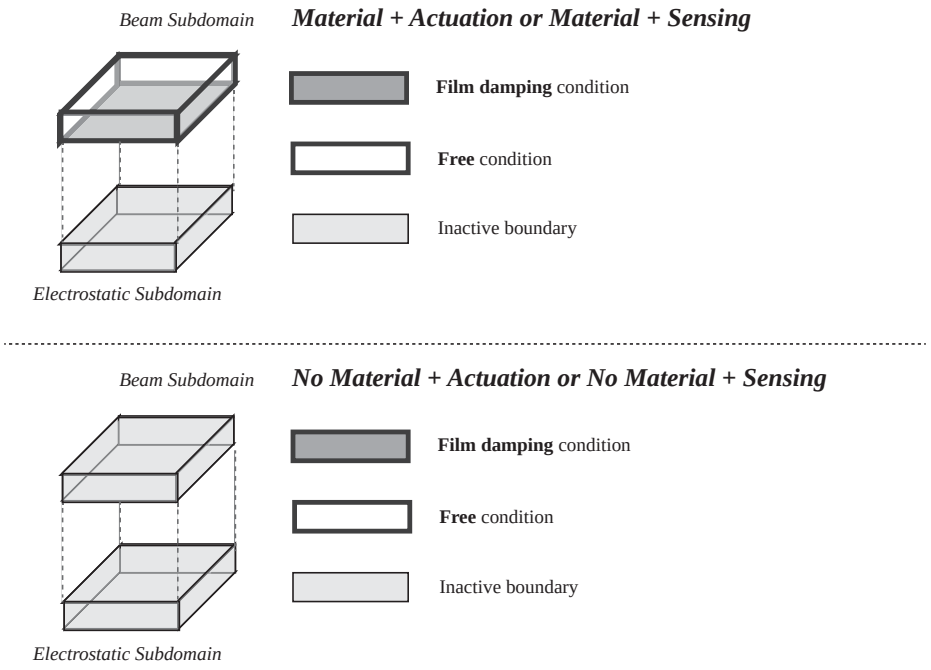

Figure 6.13. COMSOL boundary settings in the MMFD application for the frequency response analysis

difference between the amplitude of oscillation at steady-state, w_{fr}, and the static deflection, w_{sd}, is computed to determine the change in displacement due to harmonic actuation for each sensing beam subdomain, δw. The displacement is then averaged over the entire sensing area, δw_{avg}. The average displacement, is related to a change in capacitance, δc_{avg}, using the parallel plate approximation, shown by Eq. 6.1.

$$\delta c_{avg} = \frac{\epsilon A_{sensing}}{\delta w_{avg}} \tag{6.1}$$

6.4.4 Fitness Evaluation

The fitness value is defined in this work as a two-point RMS computation of the average sensed change in capacitance for the device at two frequencies for a given accumulation of mass. The change in average sensed capacitance before and after mass accumulation for each frequency is computed using Eq. 6.2.

$$\Delta C_{fi} = |\delta c_{avg_{device+mass}} - \delta c_{avg_{device}}| \tag{6.2}$$

The fitness of the configuration, fit, is the two point RMS computation, shown in Eq. 6.3.

$$fit = \sqrt{\frac{\Delta C_{f1}^2 + \Delta C_{f2}^2}{2}} \tag{6.3}$$

The genetic algorithm optimization aims to minimize the cost function. Therefore, the actual fitness value, $fval$, is computed as the recipricoal of the two point RMS calculation, shown in Eq. 6.4. This ensures that devices with the largest changes in average sensed capacitance have the lowest fitness values.

$$fval = \frac{1}{fit} \tag{6.4}$$

6.5 Optimization Results

This section presents the results from several sample optimization runs. The first run is for a small population, over the course of 15 generations, using the parallel plate approximation model. The second run is for a small population, over the course of 15 generations, using the interpolated force model. The third run is for a larger population, over the course of 5 generations using the interpolated force model. The initial population of the third run is seeded with the best output configurations of the previous runs.

6.5.1 Optimization using the Parallel Plate Approximation Model for a Small Population

The genetic algorithm based optimization, using the parallel plate approximation model, is run for a population of 100 members. For this work, the design space after symmetry is set to 8 rows by 8 columns and each domain is 10 μm long by 10 μm wide. The actuation voltage ranges between 40 V and 100 V and is defined by 2 bits. The initial gap and the beam thickness range between 2.5 μm and 4.0 μm and are each defined by 2 bits as well.

After 15 generations, the optimization improves the design by approximately a factor of 2. Figure 6.14 shows the reduction of the best fitness value through each generation. The output configuration of the optimization is illustrated in Figure 6.15, noting the configuration is symmetric about the horizontal axis. For the output configuration, the initial gap and the beam thickness are 4.0 μm and the actuation voltage is 100 V. The fitness of the output configuration is approximately 4.7 fF.

The fitness of this output configuration is also computed using the benchmark model

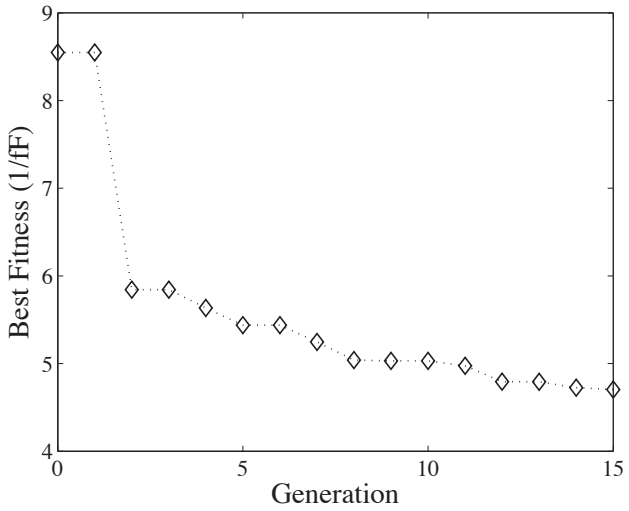

Figure 6.14. Minimum/Best fitness value for each generation of the optimization using the parallel plate approximation model

and the interpolated force model. Using the parallel plate approximation model, the fitness computation contains approximately 25% error compared to the benchmark model and reduces the total solution time by approximately 67%. Using the interpolated force model, the fitness computation contains approximately 2% error and reduces the total solution time by approximately 10% compared to the benchmark model.

6.5.2 Optimization using the Interpolated Force Model for a Small Population

The genetic algorithm based optimization, using the interpolated force model, is run for a population of 100 members. For this work, the design space after symmetry is set to 8 rows by 8 columns and each domain is 10 μm long by 10 μm wide. The actuation voltage ranges between 40 V and 100 V and is defined by 2 bits. The initial gap and the beam thickness range between 2.5 μm and 4.0 μm and are each defined by 2 bits as well.

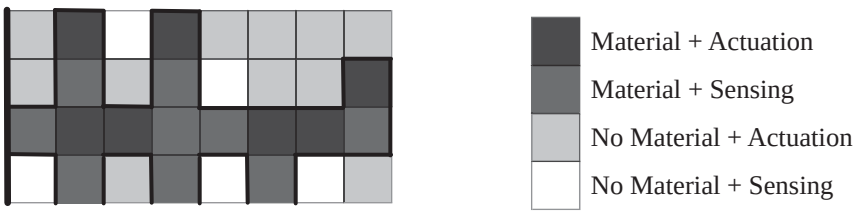

Figure 6.15. (a) Genetic algorithm optimization output configuration using the parallel plate approximation model; (b) Material distribution and electrode configuration legend

After 15 generations, the optimization improves the design by approximately a factor of 6. Figure 6.16 shows the reduction of the best fitness value through each generation. The output configuration of the optimization is illustrated in Figure 6.17, noting the configuration is symmetric about the horizontal axis. For the output configuration, the initial gap and the beam thickness are 4.0 μm and 3.5 μm, respectively and the actuation voltage is 100 V. The fitness of the output configuration is approximately 3.2 fF.

The fitness of this output configuration is also computed using the benchmark model and the parallel plate approximation model. Using the parallel plate approximation model, the fitness computation contains approximately 86% error compared to the benchmark model and reduces the total solution time by approximately 70%. Using the interpolated force model, the fitness computation contains approximately 12% error and reduces the total solution time by approximately 25% compared to the benchmark model.

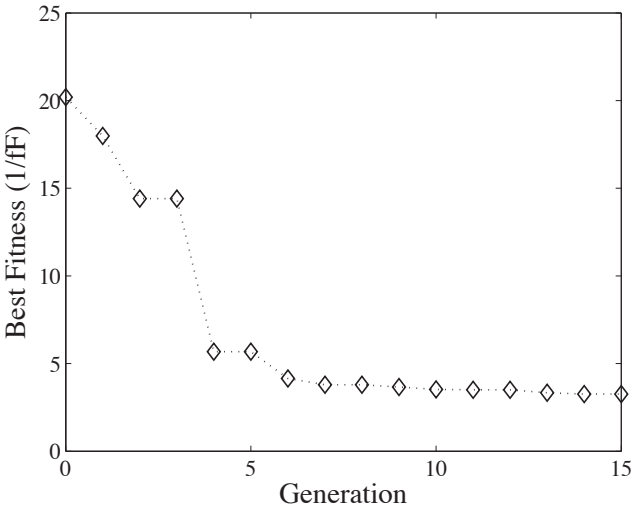

Figure 6.16. Minimum/Best fitness value for each generation of the optimization using the interpolated force model

6.5.3 Optimization using the Interpolated Force Model for a Large Population

The genetic algorithm based optimization, using the interpolated force model, is run for a population of 1000 members. For this work, the design space after symmetry is set to 8 rows by 8 columns and each domain is 10 μm long by 10 μm wide. The actuation voltage ranges between 40 V and 100 V and is defined by 2 bits. The initial gap and the beam thickness range between 2.5 μm and 4.0 μm and are each defined by 2 bits as well. The initial population is seeded with the output configurations shown in Figure 6.15 and Figure 6.17.

After 5 generations, the optimization improved the design beyond the previous optimization runs by approximately 7%. Figure 6.18 shows the reduction of the best fitness value through each generation. The output configuration of the optimization is illustrated in Figure 6.19, noting the configuration is symmetric about the horizontal axis. For the output configuration, the initial gap and the beam thickness are 4.0 μm and 3.5μm, respectively

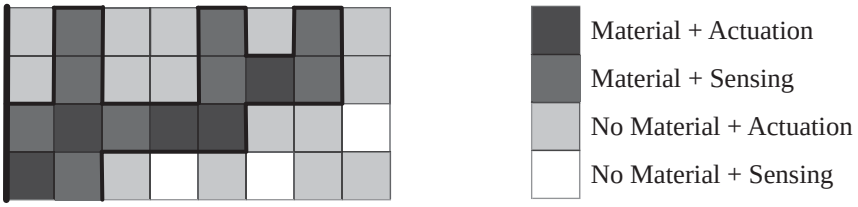

Figure 6.17. (a) Genetic algorithm optimization output configuration using the interpolated force model; (b) Material distribution and electrode configuration legend

and the actuation voltage is 100 V. The fitness of the output configuration is approximately 3.0 fF.

The fitness of this output configuration is also computed using the benchmark model and the parallel plate approximation model. Using the parallel plate approximation model, the fitness computation contains approximately 80% error compared to the benchmark model and reduces the total solution time by approximately 67%. Using the interpolated force model, the fitness computation contains approximately 13% error and reduces the total solution time by approximately 16% compared to the benchmark model.

6.5.4 Optimization Conclusions

Genetic algorithm based optimization is a viable tool for improving the design of an electrostatic MEMS resonant mass sensor. The optimization does not guarantee a global minimum, but does report a family of good designs, improved from the initial population. Besides defining actuation and material configurations for flexible structures that are are sensitive to changes in mass, a number of other trends are noted from the results due to the expanded

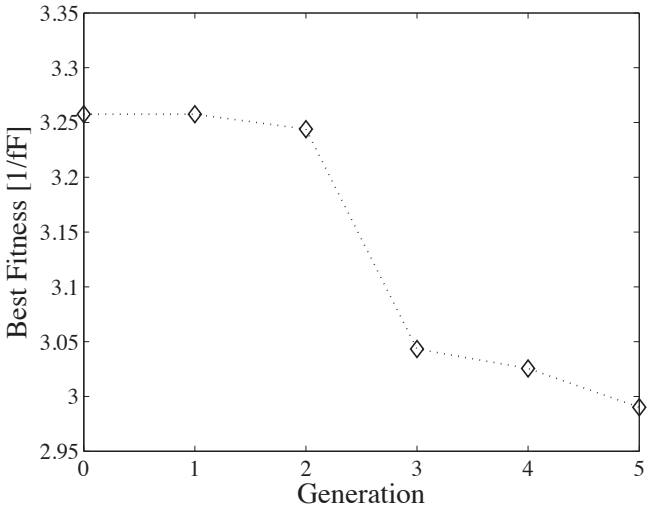

Figure 6.18. Minimum/Best fitness value for each generation of the optimization using the interpolated force model with a larger population

design space. Three trends are discussed below and are demonstrated on the configuration illustrated by Figure 6.19.

1. *Large areas of material increases the effect of squeeze-film damping on the structure, increasing the fitness of the configuration.* The configuration in Figure 6.19 shows a hole in domain 9 (see Figure 6.3 for domain numbering scheme). Changing domain 9 from a domain without material and assigned actuation to a domain with material and assigned actuation impedes the motion of the structure by way of an increased damping force, and increases the fitness value by approximately 103%.

2. *Actuation due to fringing fields of electrodes not placed directly across the gap from material, leads to larger deflections, decreasing the fitness.* Fringing forces are generally small enough in magnitude so as to not induce pull-down. The configuration in Figure 6.19 contains 14 domains assigned no material and actuation. The fring-

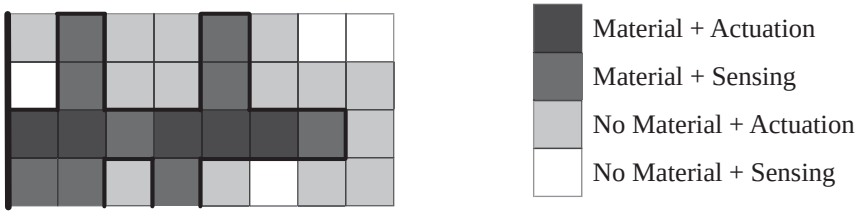

Figure 6.19. (a) Genetic algorithm optimization output configuration using the interpolated force model with a larger population; (b) Material distribution and electrode configuration legend

ing forces generated by these domains contribute to the deflection of the structure. Changing these domains, numbers 4, 9, 11, 12, 15-17, 23-25, 27 and 29-31, to no material and sensing increases the fitness value by approximately 98%. In fact, changing the 4 domains assigned no material and sensing (numbers 3, 21, 28 and 32) to domains assigned no material and actuation, improves the fitness value by approximately 2.0%.

3. *Sensor electrode placement must be considered carefully as placement of sensing domains affects both the magnitude of the actuation force and the average deflection.* Sensing location is important for two reasons. The first reason is that sensing electrodes take away from the magnitude of the electrostatic actuation force, affecting the deflection of the device. The second reason is that a sensing location with limited motion can detract from the average deflection and make a configuration with good sensitivity appear as though it does not. It is also important to note that a domain sensitive to a mass change without being assigned a sensing electrode can also make a configuration with good sensitivity appear as though it does not, assuming that the

removal of the actuation electrode (required for the addition of the sensing electrode) does not significantly alter the motion of that domain.

7. Learning Control to Eliminate Bounce for a RF-MEMS Switch

A learning control algorithm is presented that reduces the closing time of a radio frequency microelectromechanical systems switch by minimizing bounce while maintaining robustness to fabrication variability. A single degree-of-freedom model was utilized to design a learning control algorithm that shapes the actuation voltage based on the open/closed state of the switch in real-time. The initial input is based on the soft landing presented in (65) and (66).

Section 7.1 will discuss the dynamics of the device and identification of system parameters. The details of the learning control will be described in Section 7.2. Simulation results and experimental results appear in Section 7.3 and Section 7.4, respectively. The conclusions are given in Section 7.5

A single degree-of-freedom model was used to design a learning control algorithm that

shapes the actuation voltage based on the open/closed state of the switch. Experiments on 3 test switches show that after 5-10 iterations, the learning algorithm lands the switch plate with an impact velocity not exceeding 0.20 m/s, eliminating bounce. Simulations show that robustness to parameter variation is directly related to the number of required iterations for the device to learn the input for a bounce-free closure.

7.1 Switch Dynamics and System Identification

The device considered is an electrostatically actuated, parallel plate RF-MEMS switch similar to that sketched in Figure 4.1 in Section 4.1. The movable electrode is suspended above the fixed electrode with 4 folded-beam springs. The springs are attached to the substrate by 2 anchors and connect to each corner of the switch plate. The electrostatic force to close the switch is generated by a voltage potential applied between the plate and the electrodes on the substrate directly beneath it.

Upon actuation, the electrostatic force overcomes the spring restoring force and the plate moves towards the contacts. Under static conditions, stability is limited to one-third of the initial gap between the plate and the contacts. The instability is an inherent result of the nonlienar electrostatic actuation force. When the plate reaches the unstable position, it snaps down to the contacts and closes the switch. This phenomenon is referred to as pull-in (125–127). Pull-in dynamics result in excessive impact velocities of the plate, causing wear on the electrodes and reducing the lifetime of the switch (see, e.g. references (66) and (128)). Another side effect of a large impact velocity is the plate bouncing and interrupting the transmission after initial closure. Since switch closure time is defined as the time after all

bounce has decayed, this results in long closure times. The goal of the learning control is to maintain minimum closure time of the switch by reducing the bounce at impact, eliminating interruptions subsequent to switch closure.

A single degree-of-freedom model of the switch is created for simulation-based development of the control strategy. While the nonlinearities associated with damping in MEMS devices have been investigated (129), to maintain the simplicity of the model, constant damping is assumed. The following notation will be used throughout the remainder of this section: natural frequency of the free system, ω_f; damping ratio of the free system, ζ_f; position of the mass, x; initial distance between the plate and the substrate (with zero input), d_g; travel range the plate is required to move to close the switch, d_t; electrostatic force exerted on the plate, F_{es}; permittivity of free space, ϵ_0; surface area of the electrodes, A; actuation voltage, V_a; mass of the switch plate, m. Figure 4.1 is re-sketched in Figure 7.1 to represent the RF-MEMS switch.

The electrostatic force exerted on the switch plate is approximated using the parallel plate model described in Section 4.2 is given in Eq. 7.1.

$$F_{es} = -\frac{\epsilon_0 A V^2}{2(d_g - x)^2} \tag{7.1}$$

The dynamic equation for the model is given by Eq. 7.2.

$$\ddot{x} + 2\zeta_f \omega_f \dot{x} + \omega_f^2 x = \frac{F_{es}}{m} \tag{7.2}$$

An electrostatic constant, K_{es}, is defined by Eq. 7.3 to give the dynamic equation in Eq. 7.4.

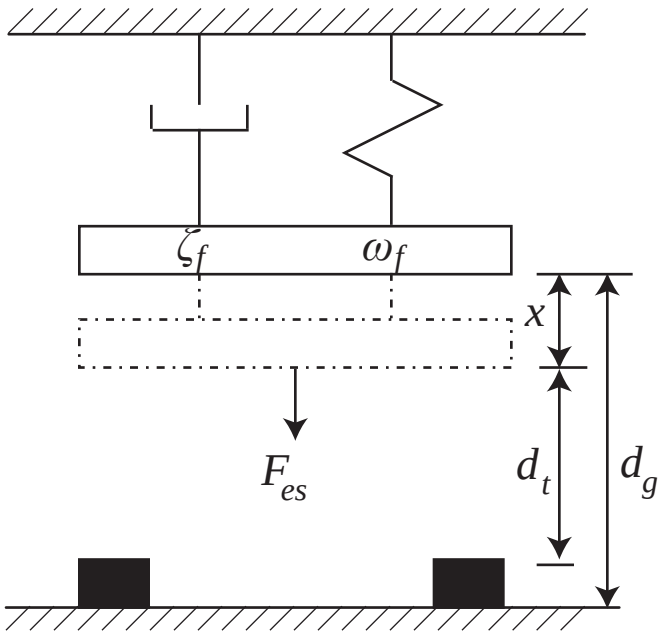

Figure 7.1. Single degree-of-freedom RF-MEMS switch model for free dynamics

$$K_{es} = \frac{\epsilon_0 A}{2m} \tag{7.3}$$

$$\ddot{x} + 2\zeta_f \omega_f \dot{x} + \omega_f^2 x = \frac{K_{es} V_a^2}{(d_g - x)^2} \tag{7.4}$$

A secondary single degree-of-freedom system, adding stiffness and damping, is used to model an impact, illustrated by Figure 7.2, similar to the work presented in (128). The natural frequency and damping ratio of the system during contact are represented by ω_c and ζ_c, respectively. This secondary system is implemented in the simulation only when the dynamics of the system indicated contact between the electrodes.

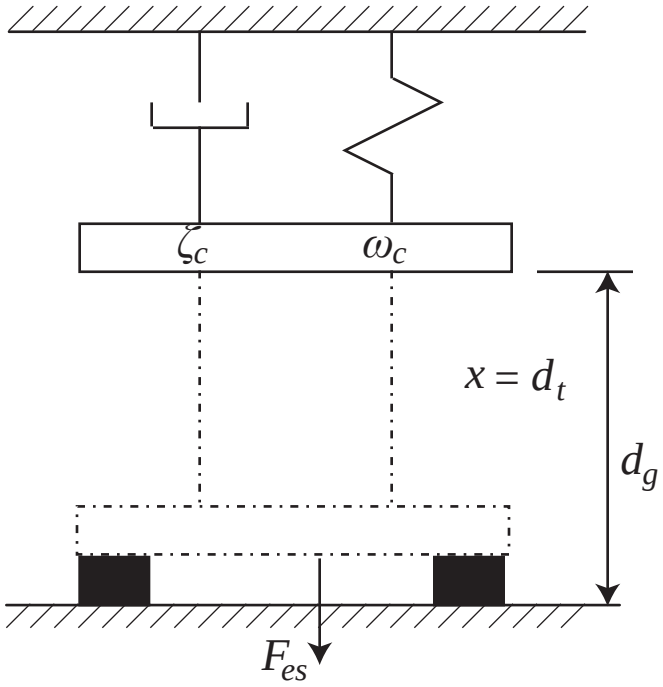

Figure 7.2. Single degree-of-freedom RF-MEMS switch model for contact dynamics

The linear parameters, ω_f and ζ_f, in the model are determined experimentally using base motion to excite the switch (130). Figure 7.3 shows the frequency response function between the plate mass and the substrate. The first significant mode of the system, ω_f, is found to be at 21 kHz with a damping ratio, ζ_f, of 0.02.

The gap, d_g is obtained from the work in (65) and (66) performed on the same type of switch. A gradient-based optimization algorithm is used to tune the remaining parameters, d_t, K_{es}, ω_c and ζ_c to a measured data set. The final list of model parameters is displayed in Table 7.1.

A time domain simulation is created using the parameters identified in Table 7.1. When the switch is in an open position, the simulation runs using the system described by Eq. 7.4.

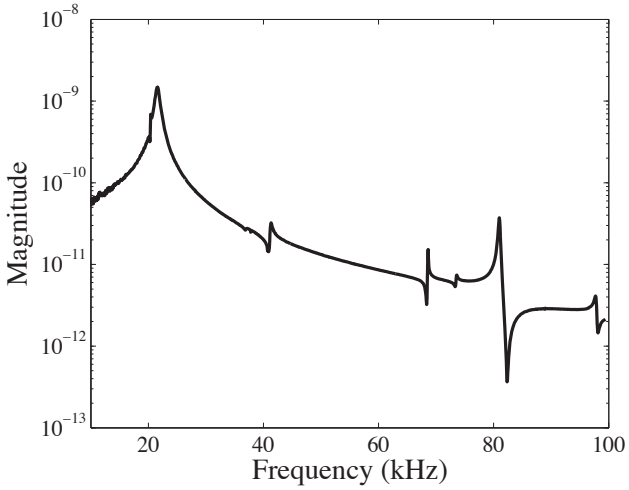

Figure 7.3. Base excitation frequency response of the switch plate in reference to the substrate

An idealized voltage across the contacts is simulated in the model as well. The voltage is high when the switch is open and low when the position of the plate, x, is less than a threshold. The threshold to signal contact was set at 0.1 μm in the simulation. While the simulated voltage is low, the simulation runs the impact model described by Eq. 7.5.

Table 7.1.
Nominal parameters for model simulation

Parameter	Units	Value
ω_f	Hz	2.1×10^4
ζ_f	–	2.0×10^{-2}
d_g	m	3.8×10^{-6}
d_t	m	2.6×10^{-6}
K_{es}	F·m/kg	1.9×10^{-11}
ω_c	Hz	6.1×10^4
ζ_c	–	4.2×10^{-1}

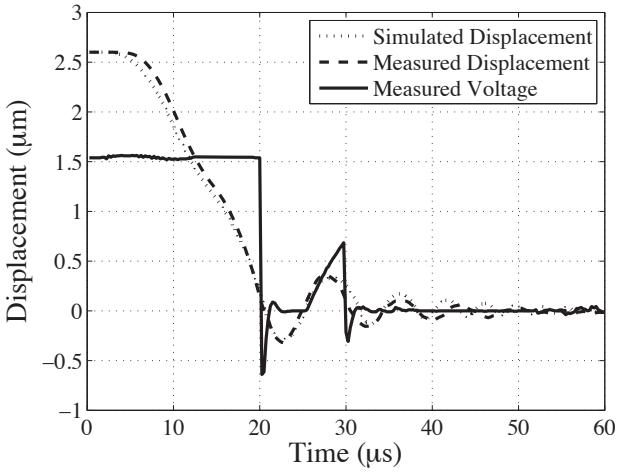

Figure 7.4. Comparison of model to measured response, including bounce

$$\ddot{x} + 2\zeta_c\omega_c\dot{x} + \omega_c^2 x = \frac{K_{es}V_a^2}{(d_g - x)^2} \tag{7.5}$$

The system reverts to the system model in Eq. 7.4 when the electrodes are no longer in contact (simulation voltage high). Figure 7.4 compares the simulation to measured data from a test part, including bounce. The data is collected using single-point velocity measurements on a laser Doppler vibrometer and did not capture tilt or bending of the plate that can cause one location of the plate to be at a different displacement than the exact point of the contact. When the location of the laser is not placed directly over the contact, the displacement can surpass the travel range of the switch, dipping below a position of 0 μm.

7.2 Learning Control Design

Learning control utilizes the system response to a known input to adjust the control law after each cycle (131–133). Different implementations of learning control are employed depending on the knowledge of the system. If the desired path is known, the error function is generally a function of the difference between desired and actual system states at each point in the trajectory. For the RF-MEMS switch, good variables to monitor would be displacement and velocity. However, obtaining velocity measurements on MEMS parts is currently impractical outside of a laboratory setting, and displacement measurements would likely require the inclusion of microelectronics at the RF-MEMS devices. To eliminate the need for any changes to the switch and to make control of the switch practical, the control algorithm developed in this paper is based only on the continuity across the switch contacts (if the switch is open or closed). The voltage is sampled at 4 MHz - a rate faster than the switch dynamics.

Measuring the continuity across the switch gives no significant information about the path of the switch - it only indicates contacting and non-contacting positions. In this particular case, there are two critical components of the trajectory: (i) the timing of the initial closure relative to the application of the switch close command and (ii) whether an interruption exists in the continuity after the initial closure (switch re-opening due to bounce). The desired end-point conditions of the switch are that of minimal close time with a soft landing - ideally, the plate reaches closure with zero velocity, makes contact, and stays in contact.

To achieve these goals, an iterative method is developed for generating the switch input voltage time history that results in a bounce-free closure and is robust to parameter variation.

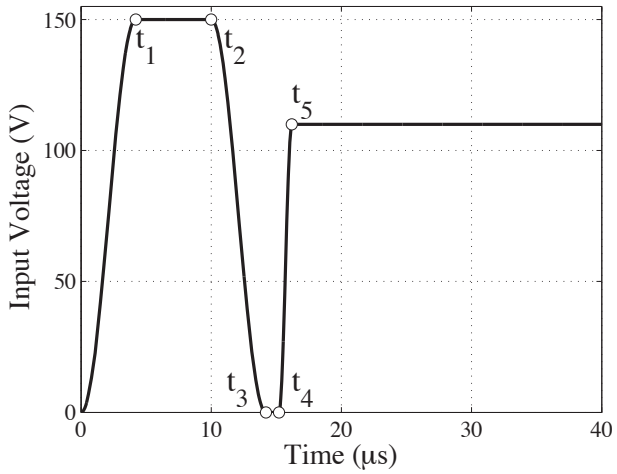

Figure 7.5. Sample shaped input waveform

The shaped time history input was first introduced in (65) and (66). A sample input is shown in Figure 7.5 and described in the functional form by Eq. 7.6.

$$V_a(t) = \begin{cases} 0 \leq t < t_1 & \frac{1}{2}V_p(1 - cos(\omega_1 t) \\ t_1 \leq t < t_2 & V_p \\ t_2 \leq t < t_3 & \frac{1}{2}V_p(1 - cos(\omega_1(t - t_2 + t_1))) \\ t_3 \leq t < t_4 & 0 \\ t_4 \leq t < t_5 & \frac{1}{2}V_h(1 - cos(\omega_2(t - t_4) \\ t_5 \leq t < t_6 & V_h \end{cases} \tag{7.6}$$

Each time designation in Figure 7.5 and Eq. 7.6 is defined in Table 7.2. In general, the input is characterized by an initial pulse, followed by a hold voltage, separated from the pulse by a short zero voltage. The initial pulse of the waveform is used to move the switch toward the contacts. Before it reaches pull-in, the voltage is set to zero, and the momentum in the switch plate allows it to coast toward the contacts. At the end of the coast period, the

Table 7.2.
Input waveform breakpoints

Parameter	Units	Value
t_1	s	4.20×10^{-6}
t_2	s	t_p
t_3	s	$t_1 + t_2$
t_4	s	$t_c + t_3$
t_5	s	$t_4 + 1.00 \times 10^{-6}$
t_6	s	100×10^{-6}
ω_1	rad/s	7.4×10^5
ω_2	rad/s	3.1×10^6

hold voltage is applied. The waveform utilizes a haversine function to transition between the different voltage levels. A piecewise continuous function, given in Eq. 7.6, compiles the waveform based on the values of V_h, V_p, t_p and t_c.

In the learning process, any of the 4 variables can be changed: the magnitude of the initial pulse, V_p, the hold voltage, V_h, the coast time, t_c and the end time of the initial pulse, t_p. The input waveform must start out conservative so as to not break the device. The device will fail when enough voltage is applied such that the displacement of the mass equals or exceeds the total gap, welding the switch in the closed position. The correct voltages may not be known prior to operation. This type of learning control can determine those voltages, as long as the initial attempts are conservative enough to avoid breaking the device.

Nominal values of 98 V and 72 V for V_p and V_h are chosen, respectively. These values are 65% of the magnitudes suggested in (65) and (66) for a similar device ($V_p = 150$ V and $V_h = 110$ V). If the switch does not make contact during the first iteration, the magnitudes are increased to 70% of the suggested waveform. The waveform is then increased by 5% at each iteration until contact is made.

Once contact is made for the first time, the magnitudes in the waveform are fixed, and only t_p and t_c are adjusted on future iterations. Upper and lower limits are set at the beginning of the control algorithm for t_p and t_c. Both variables begin at their lower limits, 5 and 1 μs, respectively. Once the magnitude of the input is fixed, if the switch does not land within a region of when V_h is applied, t_p is incrementally increased using Eq. 7.7 until the switch lands within the region or lands early (before V_h is applied). The current value of t_p is denoted by $t_{p,n}$. The fraction by which $t_{p,n}$ is adjusted for the next iteration is denoted by Δt_p, and the new value of $t_{p,n}$ is denoted by $t_{p,n+1}$.

$$t_{p,n+1} = (1 + \Delta t_p) \cdot t_{p,n} \tag{7.7}$$

After the first iteration that records an early initial closure, the current and previous values of t_p are used as the new limits, and the next value of t_p is assigned the central value in that interval. Each adjustment after this iteration employs the same bisectional-type method of adjustment described in Eq. 7.8, where the upper and lower limits are determined by the values used in the previous two input waveforms. The upper and lower bounds are denoted by $t_{p,u}$ and $t_{p,l}$, respectively.

$$t_{p,n+1} = \frac{1}{2} \cdot (t_{p,l} + t_{p,u}) \tag{7.8}$$

Once contact is recorded within the region of when V_h is applied, t_c is increased incrementally, according to Eq. 7.9, until bounce is eliminated. The current value of t_c is denoted by $t_{c,n}$. The fraction by which $t_{c,n}$ is adjusted is denoted by Δt_c, and the new value of $t_{c,n}$ is denoted by $t_{c,n+1}$.

$$t_{c,n+1} = (1 + \Delta t_c) \cdot t_{c,n} \tag{7.9}$$

At any point in the learning process, if closure no longer occurs when V_h is applied, the control reverts back to adjust t_p.

7.3 Simulation Results

By using the set of nominal model parameters listed in Table 7.1 and the input parameters in Table 7.3, the simulation required 10 iterations to eliminate ounce. In the final iteration of the simulation, V_h is equal to 82.5 V and V_p is equal to 112 V. Figure 7.6 shows the adjustments made to t_p and t_c throughout the simulation. Figure 7.7 shows the position time history of the initial response, an intermediate response and the response on the final iteration.

As mentioned in Section 7.2, devices can fail if too much voltage is applied. Even among parameter variations, this type of learning control can determine an initial waveform

Table 7.3.
Input parameters

Parameter	Units	Value
V_p	V	98
V_h	s	72
t_p	μs	5.0
t_c	μs	1.0
Δt_p	%	25
Δt_c	%	25

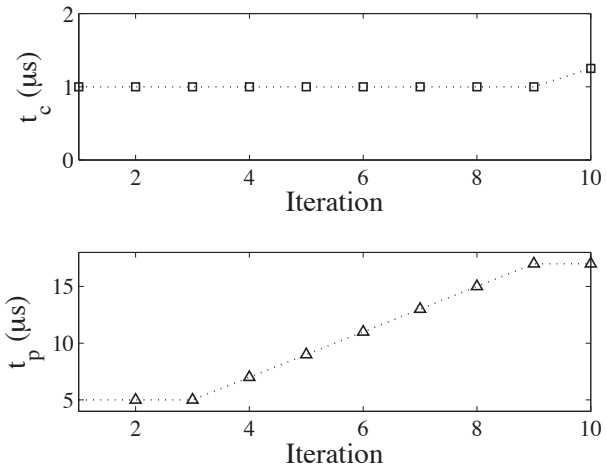

Figure 7.6. Simulation value of t_c and t_p, in μs, for each iteration

that is conservative enough to not break the switch. However, increased robustness of the system comes at a cost of iterations - more time will be required to find a solution that has eliminated bounce. An analysis looked briefly at the relationship between the number of iterations, the number of failed devices, and parameter uncertainty. By using a random uniform distribution, each system parameter (ζ_f, ω_f, K_{es}) was varied up to $\pm 5\%$, $\pm 25\%$ and $\pm 50\%$ of the nominal value. Fifteen simulations were completed for each case, once using the suggested waveform as an initial input and second using 50% of the magnitude of the suggested waveform as the initial input. Table 7.4 displays the average number of iterations for each simulation set. The simulations show that the more conservative the initial waveform is, the larger the number of required iterations, but the number of failed devices is also reduced. Zero devices failed using the reduced initial waveform.

With the control strategy described in Section 7.2, 225 simulation trials are run with the parameters varied up to $\pm 15\%$ uing a uniform random distribution. In all cases, the control found a solution that eliminated bounce with an average of 14.8 iterations. The simulations

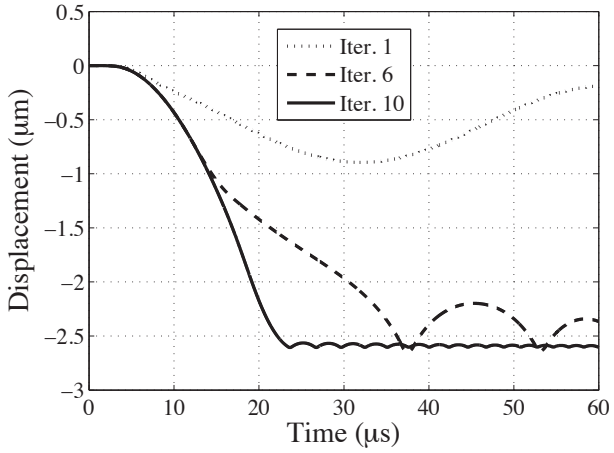

Figure 7.7. Position time history of the simulated response to show elimination of bounce

Table 7.4.
Average number of iterations for each simulation set

V_p	V_h	$\pm 5\%$	$\pm 25\%$	$\pm 50\%$
150 V	110 V	5.80	11.0	12.8
75 V	55 V	16.7	17.1	17.9

ranged from 1 to 24 iterations. Figure 7.8 shows the iteration distribution over the range. At most, the strategy would require 240 ms (24 iterations at 100 μs per iteration) to learn the correct input for zero bounce closure.

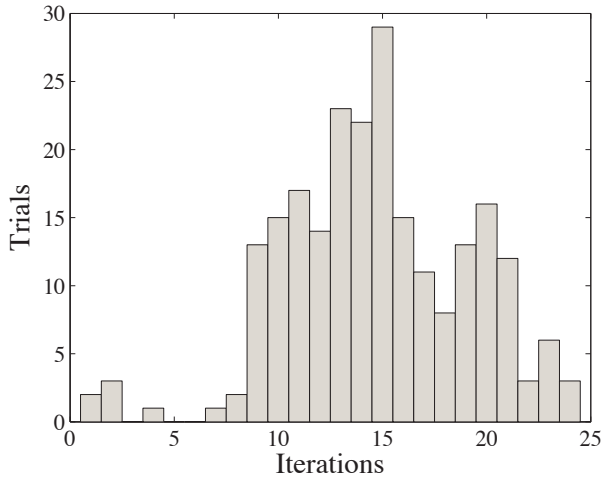

Figure 7.8. Iteration distribution for the simulation set

7.4 Experimental Results

The control scheme is implemented experimentally on 3 test switches. Since it is known that a value of V_h equal to 110 V and V_p equal to 150 V are appropriate for this type of switch based on the work in (65) and (66), the control implemented in the tests begins with these magnitudes as the nominal values in order to reduce the number of iterations, and wear on the actual test pieces.

The test bed consisted of a four-probe station with a laser Doppler vibrometer for measuring switch displacement. Two probes provide switch actuation voltage, while two more probes measure continuity across the switch by recording the voltage across a resistor and a constant voltage source placed in series with the switch. The controller logic, programmed in LabView, relied solely on the binary continuity measurement. Results were recorded for the 3 switches, referred to as devices 1, 2 and 3.

Table 7.5.
Experimental input parameters

Parameter	Units	Value
V_p	V	150
V_h	V	110
t_p	s	5.00×10^{-6}
t_c	s	1.00×10^{-6}
Δt_p	%	25
Δt_c	%	25

The input parameters, listed in Table 7.5, when applied to device 1, require 7 iterations to eliminate bounce. Figure 7.9 shows the actuation waveform for the first and final iterations. Figure 7.10 shows the associated time history of the continuity measured across the switch as well as the position measured from the laser vibrometer for the response of the switch under the initial waveform and the final waveform in the learning process. The interesting points to note are the lack of interruption in the continuity in the final iteration and the reduction of closing time between the two iterations.

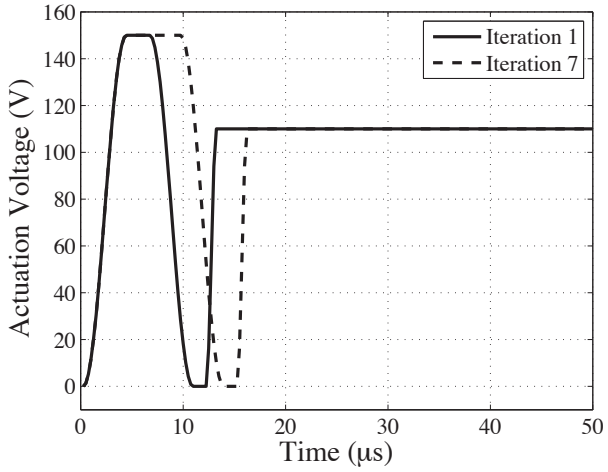

Figure 7.9. Device 1 experimental open-loop voltage command for the first and final iterations

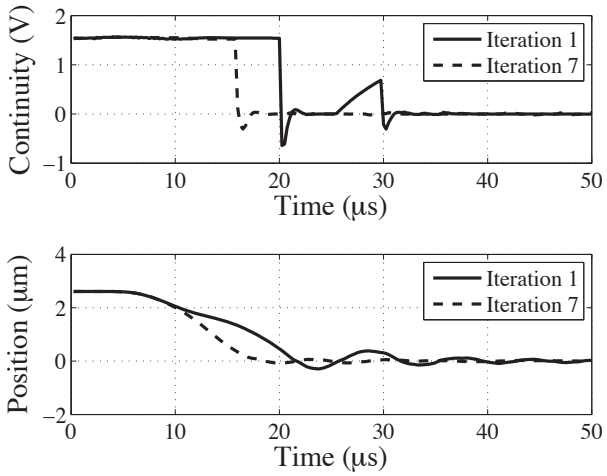

Figure 7.10. Device 1 experimental continuity measurement and position time history to show elimination of bounce

During the experiment, t_p changes from 5 to 9.8 μs and t_c remains at 1 μs, as shown in Figure 7.11. Figure 7.10 shows that on the first iteration, the switch plate initially lands at approximately 20 μs. Figure 7.9 shows the landing occurring after V_h is applied at 13 μs. Since the landing occurs too late, t_p is incrementally increased. This continues through iteration 4. Iteration 5 records an initial closure too early (before V_h was applied). By using the value of t_p on iteration 4 as the lower bound and the value of t_p on iteration 5 as the upper bound, the value of t_p is adjusted using the bi-sectional method on iteration 7, described by Eq 7.8, after resetting its value in iteration 6. On the final iteration, the initial closure of the switch coincides with the application of the hold voltage, V_h at approximately 16 μs.

Figure 7.12 shows the measured velocity response of device 1 for the first and final iterations. Two markers on the plot indicate initial landing of the switch plate. The learning algorithm reduces the initial contact velocity from 0.29 m/s on the first iteration to 0.11 m/s on the final iteration. This reduction in velocity between the two iterations eliminates the

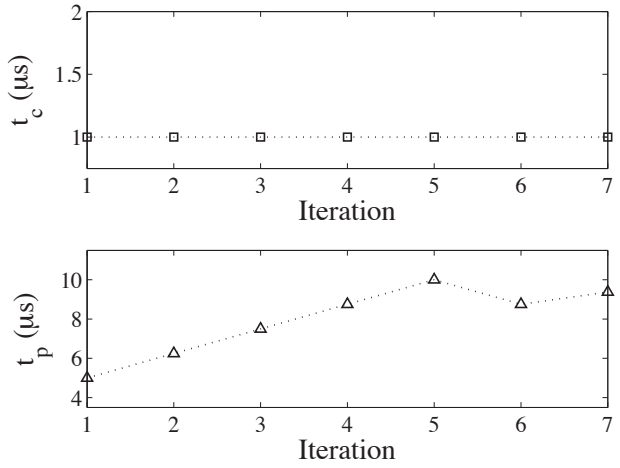

Figure 7.11. Experimental value of t_p and t_c, in μs, at each iteration for device 1

Table 7.6.
Experimental waveform parameters for 3 devices

Device	Iterations	Initial t_p (μs)	Initial t_c (μs)	Final t_p (μs)	Final t_c (μs)
1	7	5.00	1.00	9.38	1.00
2	9	5.00	1.00	9.50	1.50
3A	7	5.00	1.00	9.38	1.00
3B	4	10.0	1.00	9.38	1.00

bounce of the switch plate. Without bounce, the total closure time of the switch is reduced from $34 - 16$ μs. The higher frequency content shown in Figure 7.12 is attributed to higher modes of the system that could appear if the measurement location is not on the exact contact location.

The same initial parameters are applied to device 2 with the exception that Δt_p is set to 40%. Table 7.6 compares the values of t_p and t_c for the each of the tests.

Comparing devices 1 and 2, similar initial inputs to the system, the tests result in dif-

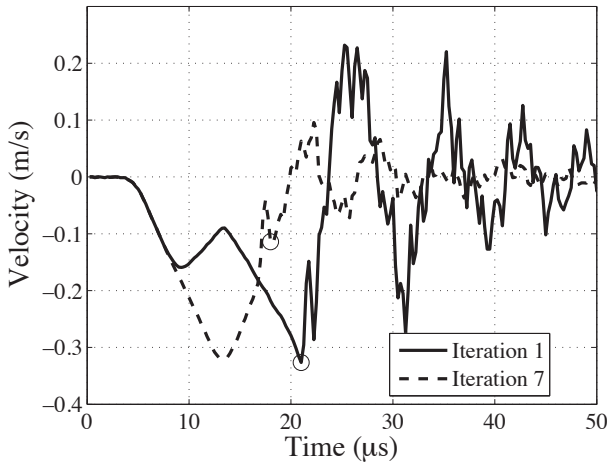

Figure 7.12. Device 1 experimental velocity response

Table 7.7.
Experimental impact velocity for 3 devices

Device	Iter.	Initial impact velocity (m/s)	Final impact velocity (m/s)	Initial time to close (s)	Final time to close (s)
1	7	0.29	0.11	34	16
2	9	0.25	0.18	45	18
3A	7	0.35	0.20	38	17
3B	4	0.37	0.20	31	17

ferent waveforms. This indicates that there is variation within one or more parameters that affects the dynamics of the switch; however, the strategy is still able to find a waveform for each that eliminates bounce. The impact velocities and closure times are compared in Table 7.7. The final waveform reduces the impact velocity, thus reducing the bounce event, for all cases.

Two different input waveforms are applied to device 3, referred to as set A and set B, respectively, to explore the effect that changing the initial waveform has on the control

algorithm output. Set A uses the parameters described in Table 7.5. Set B uses the same parameters, but begins with a value of 10 μs for t_p. The values of t_p and t_c in the two tests on device 3 are compared in Table 7.6. Upon elimination of the bounce, the total closure time is reduced to the same value as set A, 17 μs. The velocity at impact for device 3 is also compared in Table 7.7.

The results of the experiments demonstrated that the learning algorithm could be implemented to reduce the velocity of the initial impact and thus remove any significant bounce of the switch plate. The elimination of bounce greatly reduces the time required for closure of the switch.

7.5 Learning Control for RF-MEMS Switch Conclusions

A strategy was developed to generate an open-loop input to a RF-MEMS switch that is subject to parameter variation from part to part. The algorithm used the continuity measured across the switch to adjust the parameters. Simulations show that the strategy can account for parameter uncertainty and there exists a direct relationship between the number of iterations and the magnitude of variation.

The algorithm was also tested experimentally on 3 switches and shown to eliminate bounce. The elimination of bounce due to the reduction of impact velocity to less than 0.2 m/s allowed the total closure time to be no larger than 20 μs. For the experimental data sets, 5-10 iterations were required to find a bounce free solution. It was also shown that changing the initial parameters of the waveform still results in a similar solution wen applied to the same device.

Since the control algorithm relies only on the continuity measurement across the contacts, it is imperative that this measurement be accurate. Contamination between the two electrodes could cause the continuity to degrade, even at impact, resulting in a larger number of iterations to find a solution, or no solution at all if the contamination is large enough and is not removed with the motion of the device. However, the fact that only a continuity measurement is required makes the control practical. For design and monetary cost, the continuity measurement could be placed in the circuitry on the chip such that the device could be calibrated at the demand of the user while in service.

8. Future Work

As with any research endeavor, there exist considerations beyond the scope of the project. This section lists 5 additions to this work that could lead to some interesting results.

1. In the genetic algorithm based optimization of the MEMS resonant mass sensor, an enhanced mass accumulation model could be added for improved control over how mass is added to the sensor to more accurately represent real conditions.

2. Practical constraints on electrode configurations in the genetic algorithm based optimization of the MEMS resonant mass sensor would be required for real-life fabrication and implementation.

3. In the genetic algorithm based optimization of the MEMS resonant mass sensor, allowing the thickness of the beam material to vary for each domain could contribute to a configuration with improved sensitivity given the effect thickness has on the stiffness of the device. Also, allowing the actuation voltage to vary at each domain could allow the fringing effects of neighboring electrodes to play a larger role in the behavior of the sensor without increasing the risk of pull-down.

4. Develop a learning control strategy, similar to that presented in Chapter 7, to determine the ideal shaped input for zero vibration actuation of the mass sensor to achieve

self calibration prior to use.

5. Integrate sensing using input shaping, presented in Chapter 5, or control designs, into the fitness function of the genetic algorithm based optimization to improve the complete system design of a MEMS mass sensor.

9. Summary of Contributions

The research described in this document provides the following contributions:

Challenge 1: A fully-coupled, structural-electrostatic model for micro devices is too computationally expensive to be used for optimization or control system design, and published approximations are not applicable to complex electrode configurations.

Contribution 1: Developed an alternative modeling technique for electrostatic micro devices with improved computational efficiency relative to a fully-coupled analysis that is valid for irregular electrode configurations.

Challenge 2: Many factors affect the sensitivity of micro sensors creating a complex design space with many local minima. Gradient based optimization methods are limited in application to electrostatic micro device design due to a tendency to be constrained by local minima, as well as fabrication limitations for topology optimization.

Contribution 2: Genetic algorithm based optimization was shown to be a valuable tool for the design of an electrostatic micro sensor. The optimization improved sensor design at each successive generation. Unique to this work, the design space was expanded upon published optimization results for micro devices to include material distribution (capable of filtering out invalid geometries), sensing and actuation electrode configuration, actuation

voltage, and other geometric parameters.

Challenge 3: MEMS resonant mass sensors based in the frequency domain require consideration for on chip signal processing and must be sensitive enough to detect very small changes in mass.

Contribution 3: Proposed using input shaping techniques as an alternative sensing strategy for the detection of mass, or other parameter changes, for micro sensors.

Challenge 4: Part-to-part variation in fabricated micro devices can lead to poor performance due to unknown plant parameters.

Contribution 4: A learning control strategy was developed to calibrate a radio-frequency micro switch by altering an input voltage waveform to eliminate bounce upon closure of the switch. The control strategy relied only on the voltage potential across the electrodes to maintain practical implementation in real world environments.

REFERENCES

[1] J. Bryzek, S. Roundy, B. Bircumshaw, C. Chung, K. Castellino, J. Stetter, and M. Vestel, "Marvelous mems," *Circuits and Devices Magazine, IEEE*, vol. 22, pp. 8–28, Mar. 2006.

[2] M. Mehregany, "Microelectromechanical systems," *Circuits and Devices Magazine, IEEE*, vol. 9, pp. 14–22, Jul. 1993.

[3] R. M. Lin and W. J. Wang, "Structural dynamics of microsystems - current state of research and future directions," *Mechanical Systems and Signal Processing*, vol. 20, pp. 1015–1043, Jul. 2006.

[4] A. Fargas Marques, R. Costa Castello, and A. Shkel, "Modelling the electrostatic actuation of mems state of the art 2005," 2005. http://bibliotecnica.upc.es/reports/ioc/IOC-DT-P-2005-18.pdf.

[5] G. Leu, S. Simion, and A. Serbanescu, "Mems optimization using genetic algorithms," in *Proc. International Semiconductor Conference*, vol. 2, pp. 475–478, Oct. 2004.

[6] M. Liu, K. Maute, and D. M. Frangopol, "Multi-objective design optimization of electrostatically actuated microbeam resonators with and without parameter uncer-

tainty," *Reliability Engineering and System Safety*, vol. 92, no. 10, pp. 1333–1343, 2007.

[7] S. Karbasi, M. Shamshirsaz, M. Naraghi, and M. Maroufi, "Optimal design analysis of electrothermally driven microactuators," *Microsystem Technologies*, vol. 16, pp. 1065–1071, 2010.

[8] H. Kotera, M. Senga, T. Hirasawa, and S. Shima, "Optimization of thickness distribution of micro-membrane by genetic algorithm," in *Proceedings of the Second International Conference on Intelligent Processing and Manufacturing of Materials*, vol. 1, pp. 245–250, Jul. 1999.

[9] M. Raulli and K. Maute, "Topology optimization of electrostatically actuated microsystems," *Structural and Multidisciplinary Optimization*, vol. 30, no. 5, pp. 342–359, 2005.

[10] B. Borovic, A. Q. Liu, D. Popa, H. Cai, and F. L. Lewis, "Open-loop versus closed-loop control of mems devices: choices and issues," *Journal of Micromechanics and Microengineering*, vol. 15, no. 10, pp. 1917–1924, 2005.

[11] R. Elliott, *Electromagnetics*. New York, NY: McGraw-Hill, Inc., 1966.

[12] J. Pelesko and T. Driscoll, "The effect of the small-aspect-ratio approximation on canonical electrostatic mems models," *Journal of Engineering Mathematics*, vol. 53, pp. 239–252, 2005.

[13] G. J. Sloggett, N. G. Barton, and S. J. Spencer, "Fringing fields in disc capacitors," *Journal of Physics A: Mathematical and General*, vol. 19, no. 14, pp. 2725–2736, 1986.

[14] G. J. Sloggett, N. G. Barton, and S. J. Spencer, "Addendum to fringing fields in disc capacitors," *Journal of Physics A: Mathematical and General*, vol. 20, no. 12, pp. 4061–4062, 1987.

[15] K. Suresh and M. Sinha, "A 2-d model that accounts for 3-d fringing in mems devices," *Engineering Analysis with Boundary Elements*, vol. 30, no. 11, pp. 963 – 970, 2006.

[16] H. Hammer, "Analytical model for comb-capacitance fringe fields," *Journal of Microelectromechanical Systems*, vol. 19, pp. 175–182, Feb. 2010.

[17] H. B. Palmer, "The capacitance of a parallel-plate capacitor by the schwartz-christoffel transformation," *Transactions of the American Institute of Electrical Engineers*, vol. 56, pp. 363–366, Mar. 1937.

[18] W. Chang, "Analytical ic metal-line capacitance formulas," *IEEE Transactions on Microwave Theory and Techniques*, vol. 24, pp. 608–611, Sept. 1976.

[19] W. Chang, "Correction to analytical ic metal-line capacitance formulas," *IEEE Transactions on Microwave Theory and Techniques*, vol. 25, p. 712, Aug. 1977.

[20] C. Yuan and T. Trick, "A simple formula for the estimation of the capacitance of two-dimensional interconnects in vlsi circuits," *IEEE Electron Device Letters*, vol. 3, pp. 391–393, Dec. 1982.

[21] T. Sakurai and K. Tamaru, "Simple formulas for two- and three-dimensional capacitances," *IEEE Transactions on Electron Devices*, vol. 30, pp. 183–185, Feb. 1983.

[22] N. P. van der Meijs and J. T. Fokkema, "Vlsi circuit reconstruction from mask topology," *Integration, the VLSI Journal*, vol. 2, no. 2, pp. 85 – 119, 1984.

[23] H. Nishiyama and M. Nakamura, "Capacitance of a strip capacitor," *IEEE Transactions on Components, Hybrids, and Manufacturing Technology*, vol. 13, pp. 417–423, Jun. 1990.

[24] H. Nishiyama and M. Nakamura, "Form and capacitance of parallel-plate capacitors," *IEEE Transactions on Components, Packaging, and Manufacturing Technology, Part A*, vol. 17, pp. 477–484, Sept. 1994.

[25] V. Leus and D. Elata, "Fringing field effect in electrostatic actuators," 2004. Technical Report ETR-2004-2.

[26] O. Sigmund, "Design of multiphysics actuators using topology optimization - part i: One-material structures," *Computer Methods in Applied Mechanics and Engineering*, vol. 190, no. 49-50, pp. 6577 – 6604, 2001.

[27] G. H. Yoon and O. Sigmund, "A monolithic approach for topology optimization of electrostatically actuated devices," *Computer Methods in Applied Mechanics and Engineering*, vol. 197, no. 45-48, pp. 4062 – 4075, 2008.

[28] S. Heo, G. H. Yoon, and Y. Y. Kim, "Minimum scale controlled topology optimization and experimental test of a micro thermal actuator," *Sensors and Actuators A: Physical*, vol. 141, no. 2, pp. 603 – 609, 2008.

[29] S. Heo and Y. Y. Kim, "Optimal design and fabrication of mems rotary thermal actuators," *Journal of Micromechanics and Microengineering*, vol. 17, no. 11, pp. 2241–2247, 2007.

[30] M. Brenner, J. Lang, J. Li, J. Qiu, and A. Slocum, "Optimal design of a mems re-

lay switch," in *Technical Proceedings of International Conference on Modeling and Simulation of Microsystems*, vol. 1, 2002.

[31] N. Pedersen, "Maximization of eigenvalues using topology optimization," *Structural and Multidisciplinary Optimization*, vol. 20, pp. 2–11, 2000. 10.1007/s001580050130.

[32] W. Ye, S. Mukherjee, and N. MacDonald, "Optimal shape design of an electrostatic comb drive in microelectromechanical systems," *Journal of Microelectromechanical Systems*, vol. 7, pp. 16–26, Mar. 1998.

[33] J. Liu, Y. Chen, and Z. Luo, "Design of monolithic compliant mechanisms for microactuator using topology optimization schemes," in *World Congress on Intelligent Control and Automation*, vol. 2, pp. 6465–6469, 2006.

[34] Z. Luo, L. Tong, and H. Ma, "Shape and topology optimization for electrothermomechanical microactuators using level set methods," *Journal of Computational Physics*, vol. 228, no. 9, pp. 3173 – 3181, 2009.

[35] R. C. Carbonari, E. C. N. Silva, and S. Nishiwaki, "Design of piezoelectric multiactuated microtools using topology optimization," *Smart Materials and Structures*, vol. 14, no. 6, pp. 1431–1447, 2005.

[36] J. S. Han, J. S. Ko, and J. G. Korvink, "Structural optimization of a large-displacement electromagnetic lorentz force microactuator for optical switching applications," *Journal of Micromechanics and Microengineering*, vol. 14, no. 11, pp. 1585–1596, 2004.

[37] J. Han and B. Kwak, "Robust optimization using a gradient index: Mems applications," *Structural and Multidisciplinary Optimization*, vol. 27, pp. 469–478, 2004. 10.1007/s00158-004-0410-3.

[38] J.-K. Byun, I.-H. Park, and S.-Y. Hahn, "Topology optimization of electrostatic actuator using design sensitivity," *IEEE Transactions on Magnetics*, vol. 38, no. 2, pp. 1053–1056, 2002.

[39] H. Li and E. Antonsson, "Genetic algorithms in mems synthesis," in *International Mechanical Engineering Congress and Expositions*, 1998.

[40] N. Zhou, "Automated design synthesis for micro-electro-mechanical systems," in *In Proc. of the ASME Design Automation Conference*, 2002.

[41] Y. Zhang, R. Kamalian, A. M. Agogino, and C. H. Sequin, "Hierarchical mems synthesis and optimization," in *SPIE Conference on Smart Structures and Materials, March 7-10, 2005, San Diego CA*, 2005.

[42] Z. Fan, K. Seo, J. Hu, E. D. G. A, and R. C. Rosenberg, "A novel evolutionary engineering design approach for mixed-domain systems," *Engineering Optimization*, vol. 36, no. 2, pp. 127–147, 2004.

[43] K. Susanto and B. Yang, "Genetic algorithm based optimization design of miniature piezoelectric forceps," in *IEEE International Conference on Robotics and Automation*, 2004.

[44] Y. Gong, F. Zhao, H. Xin, J. Lin, and Q. Bai, "Simulation and optimal design for rf mems cantilevered beam switch," in *International Conference on Future Computer and Communication*, pp. 84–87, 2009.

[45] W. Yuan, H. Chang, W. Li, and B. Ma, "Application of an optimization methodology for multidisciplinary system design of microgyroscopes," *Microsystem Technologies*, vol. 12, pp. 315–323, 2006.

[46] M. Engesser, A. Franke, M. Maute, D. Meisel, and J. Korvink, "A robust and flexible optimization technique for efficient shrinking of mems accelerometers," *Microsystem Technologies*, vol. 16, pp. 647–654, 2010.

[47] Y. Li, X. Xin, N. Kikuchi, and K. Saitou, "Optimal shape and location of piezoelectric materials for topology optimization of flextensional actuators," in *Genetic and Evolutionary Computation Conference*, pp. 1085–1089, 2000.

[48] M. Motiee, A. Khajepour, and R. Mansour, "A new topology optimization method for multi-physics micro domains," in *International Conference on Mechatronic and Embedded Systems and Applications*, pp. 106–111, 2008.

[49] G. Hornby, W. Kraus, and J. Lohn, "Evolving mems resonator designs for fabrication," in *Evolvable Systems: From Biology to Hardware*, Lecture Notes in Computer Science, pp. 213–224, Springer Berlin / Heidelberg, 2008.

[50] R. Legtenberg, J. Gilbert, S. Senturia, and M. Elwenspoek, "Electrostatic curved electrode actuators," *Journal of Microelectromechanical Systems*, vol. 6, pp. 257–265, Sept. 1997.

[51] M. A. Rosa, D. D. Bruyker, A. R. Völkel, E. Peeters, and J. Dunec, "A novel external electrode configuration for the electrostatic actuation of mems based devices," *Journal of Micromechanics and Microengineering*, vol. 14, no. 4, p. 446, 2004.

[52] J. Su, H. Yang, P. Fay, W. Porod, and G. H. Bernstein, "A surface micromachined offset-drive method to extend the electrostatic travel range," *Journal of Micromechanics and Microengineering*, vol. 20, no. 1, 2010.

[53] E. Hung and S. Senturia, "Extending the travel range of analog-tuned electrostatic actuators," *Journal of Microelectromechanical Systems*, vol. 8, pp. 497–505, Dec. 1999.

[54] M. T.-K. Hou, G. K.-W. Huang, J.-Y. Huang, K.-M. Liao, R. Chen, and J.-L. A. Yeh, "Extending displacements of comb drive actuators by adding secondary comb electrodes," *Journal of Micromechanics and Microengineering*, vol. 16, no. 4, pp. 684–691, 2006.

[55] X. tao Wu, R. Brown, S. Mathews, and K. Farmer, "Extending the travel range of electrostatic micro-mirrors using insulator coated electrodes," in *IEEE/LEOS International Conference on Optical MEMS*, pp. 151–152, 2000.

[56] G. Gray, M. Morgan, and P. Kohl, "Electrostatic actuators with expanded tuning range due to biaxial intrinsic stress gradients," *Journal of Microelectromechanical Systems*, vol. 13, pp. 51–62, feb. 2004.

[57] D. M. Burns and V. M. Bright, "Nonlinear flexures for stable deflection of an electrostatically actuated micromirror," in *Microelectronic Structures and MEMS for Optical Processing III*, pp. 125–136, SPIE Vol. 3226, 1997.

[58] G. Zhou and P. Dowd, "Tilted folded-beam suspension for extending the stable travel range of comb-drive actuators," *Journal of Micromechanics and Microengineering*, vol. 13, no. 2, pp. 178–183, 2003.

[59] J. Bronson, G. Wiens, and J. Allen, "Modeling and alleviating instability in a mems vertical comb drive using a progressive linkage," in *ASME International Design Engineering Technical Conferences and Computers and Information in Engineering Conference*, (Long Beach, CA), 2005.

[60] Y. Zhang and M. L. Dunn, "Vertical electrostatic actuator with extended digital range via tailored topology," in *Smart Structures and Materials 2002: Smart Electronics, MEMS, and Nanotechnology*, pp. 147–156, SPIE Vol. 4700, 2002.

[61] D.-Y. Qiao, W.-Z. Yuan, and X.-Y. Li, "A two-beam method for extending the working range of electrostatic parallel-plate micro-actuators," *Journal of Electrostatics*, vol. 65, no. 4, pp. 256 – 262, 2007.

[62] R. Nadal-Guardia, A. Dehe, R. Aigner, and L. Castaner, "Current drive methods to extend the range of travel of electrostatic microactuators beyond the voltage pull-in point," *Journal of Microelectromechanical Systems*, vol. 11, pp. 255–263, Jun. 2002.

[63] T. Sugimoto, K. Nonaka, and M. Horenstein, "Bidirectional electrostatic actuator operated with charge control," *Journal of Microelectromechanical Systems*, vol. 14, pp. 718–724, Aug. 2005.

[64] S. Krylov, I. Harari, and Y. Cohen, "Stabilization of electrostatically actuated microstructures using parametric excitation," *Journal of Micromechanics and Microengineering*, vol. 15, no. 6, pp. 1188–1204, 2005.

[65] D. Czaplewski, C. Dyck, H. Sumali, J. Massad, J. Kuppers, I. Reines, W. Cowan, and C. Tigges, "A soft-landing waveform for actuation of a single-pole single-throw ohmic rf mems switch," *Journal of Microelectromechanical Systems*, vol. 15, pp. 1586–1594, Dec. 2006.

[66] H. Sumali, J. E. Massad, D. A. Czaplewski, and C. W. Dyck, "Waveform design for pulse-and-hold electrostatic actuation in mems," *Sensors and Actuators A: Physical*, vol. 134, no. 1, pp. 213–220, 2007.

[67] K.-S. Chen and K.-S. Ou, "Command-shaping techniques for electrostatic mems actuation: Analysis and simulation," *Journal of Microelectromechanical Systems*, vol. 16, pp. 537–549, Jun. 2007.

[68] M. Daqaq, C. Reddy, and A. Nayfeh, "Input-shaping control of nonlinear mems," *Nonlinear Dynamics*, vol. 54, pp. 167–179, 2008.

[69] J. Seeger and S. Crary, "Stabilization of electrostatically actuated mechanical devices," in *International Conference on Solid State Sensors and Actuators*, vol. 2, pp. 1133–1136, Jun. 1997.

[70] J. I. Seeger and B. E. Boser, "Dynamics and control of parallel-plate actuators beyond the electrostatic instability," in *Proc. Transducers*, pp. 474–477, 1999.

[71] J. Seeger and B. Boser, "Charge control of parallel-plate, electrostatic actuators and the tip-in instability," *Journal of Microelectromechanical Systems*, vol. 12, pp. 656–671, Oct. 2003.

[72] J. Seeger and B. Boser, "Negative capacitance for control of gap-closing electrostatic actuators," in *International Conference on Solid-State Sensors, Actuators and Microsystems*, vol. 1, pp. 484–487, Jun. 2003.

[73] E. K. Chan and R. W. Dutton, "Electrostatic micromechanical actuator with extended range of travel," *Journal of Microelectromechanical Systems*, vol. 9, pp. 321–328, 2000.

[74] J. M. Kyynarainen, A. S. Oja, and H. Seppa, "Increasing the dynamic range of a micromechanical moving-plate capacitor," *Analog Integrated Circuits and Signal Processing*, vol. 29, pp. 61–70, 2001. 10.1023/A:1011230330035.

[75] B. Cagdaser and B. Boser, "Resonant drive for stabilizing parallel-plate actuators beyond the pull-in point," in *International Conference on Solid-State Sensors, Actuators and Microsystems*, vol. 1, pp. 688–692, Jun. 2005.

[76] P. B. Chu and K. S. J. Pister, "Analysis of closed-loop control of parallel-plate electrostatic microgrippers," in *Proc. IEEE International Conference on Robotics and Automation*, pp. 820–825, 1994.

[77] M. I. Beyaz, M. McCarthy, N. Ghalichechian, and R. Ghodssi, "Closed-loop control of a long-range micropositioner using integrated photodiode sensors," *Sensors and Actuators A: Physical*, vol. 151, no. 2, pp. 187–194, 2009.

[78] P. Cheung, R. Horowitz, and R. Rowe, "Design, fabrication, position sensing, and control of an electrostatically-driven polysilicon microactuator," *IEEE Transactions on Magnetics*, vol. 32, pp. 122–128, Jan. 1996.

[79] J. R. Bronson and G. J. Wiens, "Feedback control of mems micromirrors subject to parametric uncertainty," *ASME Conference Proceedings*, pp. 749–757, 2007.

[80] L. Wang, J. Dawson, L. Hornak, P. Famouri, and R. Ghaffarian, "Real-time translational control of a mems comb resonator," *IEEE Transactions on Aerospace and Electronic Systems*, vol. 40, pp. 567–575, Apr. 2004.

[81] Y. Zhao, F. E. Tay, G. Zhou, and F. S. Chau, "Fast and precise positioning of elec-

trostatically actuated dual-axis micromirror by multi-loop digital control," *Sensors and Actuators A: Physical*, vol. 132, no. 2, pp. 421–428, 2006.

[82] D. Horsley, N. Wongkomet, R. Horowitz, and A. Pisano, "Precision positioning using a microfabricated electrostatic actuator," *IEEE Transactions on Magnetics*, vol. 35, pp. 993–999, Mar. 1999.

[83] M.-C. Lu and G. Fedder, "Closed-loop control of a parallel-plate microactuator beyond the pull-in limit," in *Tech. Dig. Solid-State Sensor, Actuator, and Microsystems Workshop*, pp. 255–258, 2002.

[84] M.-C. Lu and G. Fedder, "Position control of parallel-plate microactuators for probe-based data storage," *Journal of Microelectromechanical Systems*, vol. 13, pp. 759–769, Oct. 2004.

[85] L. Rocha, E. Cretu, and R. Wolffenbuttel, "Using dynamic voltage drive in a parallel-plate electrostatic actuator for full-gap travel range and positioning," *Journal of Microelectromechanical Systems*, vol. 15, pp. 69–83, Feb. 2006.

[86] L. Mol, R. Wolffenbuttel, E. Cretu, and L. Rocha, "Full-gap positioning of parallel-plate electrostatic mems using on-off control," in *IEEE International Symposium on Industrial Electronics*, pp. 1464–1468, Jun. 2007.

[87] L. Mol, L. A. Rocha, E. Cretu, and R. F. Wolffenbuttel, "On-off control for full-gap positioning of parallel-plate electrostatic mems," *ASME Conference Proceedings*, vol. 2006, pp. 527–531, 2006.

[88] R. Nadal-Guardia, R. Aigner, W. Nessler, M. Handtmann, and L. Castaner, "Control positioning of torsional electrostatic actuators by current driving," in *Third In-*

ternational EuroConfrence on Advanced Semiconductor Devices and Microsystems, pp. 91–94, 2000.

[89] J. Chen, W. Weingartner, A. Azarov, and R. Giles, "Tilt-angle stabilization of electrostatically actuated micromechanical mirrors beyond the pull-in point," *Journal of Microelectromechanical Systems*, vol. 13, pp. 988–997, Dec. 2004.

[90] B. Ebrahimi and M. Bahrami, "Robust sliding-mode control of a mems optical switch," *Journal of Physics: Conference Series*, vol. 34, no. 1, pp. 728–733, 2006.

[91] M. Nikpanah, Y. Wang, F. Lewis, and A. Liu, "Real time controller design to solve the pull-in instability of mems actuator," in *International Conference on Control, Automation, Robotics and Vision*, pp. 1724–1729, Dec. 2008.

[92] M. Vagia, G. Nikolakopoulos, and A. Tzes, "Design of a robust pid-control switching scheme for an electrostatic micro-actuator," *Control Engineering Practice*, vol. 16, no. 11, pp. 1321–1328, 2008.

[93] Y. Zhao, F. E. H. Tay, F. S. Chau, and G. Zhou, "Stabilization of dual-axis micromirrors beyond the pull-in point by integral sliding mode control," *Journal of Micromechanics and Microengineering*, vol. 16, no. 7, p. 1242, 2006.

[94] Y. Sun, D. Piyabongkarn, A. Sezen, B. J. Nelson, and R. Rajamani, "A high-aspect-ratio two-axis electrostatic microactuator with extended travel range," *Sensors and Actuators A: Physical*, vol. 102, no. 1-2, pp. 49–60, 2002.

[95] D. Fernandez, J. Madrenas, and J. Cosp, "Position, damping and inertia control of parallel-plate electrostatic actuators," in *IEEE International Symposium on Circuits and Systems*, pp. 2118–2121, May 2008.

[96] J. Rogers, P. Ozmun, J. Hung, and R. Dean, "Bi-directional gap closing mems actuator using timing and control techniques," in *IEEE Conference on Industrial Electronics*, pp. 3149–3154, Nov. 2006.

[97] B. Borovic, C. Hong, A. Liu, L. Xie, and F. Lewis, "Control of a mems optical switch," in *IEEE Conference on Decision and Control*, vol. 3, pp. 3039–3044, Dec. 2004.

[98] Y.-J. Pan, Y. Ma, and S. Islam, "Electrostatic torsional micromirror: Its active control and applications in optical network," in *IEEE International Conference on Automation Science and Engineering*, pp. 151–156, Aug. 2008.

[99] H. Sane, "Energy-based control for mems with one-sided actuation," in *American Control Conference*, pp. 1209–1214, Jun. 2006.

[100] G. Zhu, J. Levine, and L. Praly, "Improving the performance of an electrostatically actuated mems by nonlinear control: Some advances and comparisons," in *IEEE Conference on Decision and Control*, pp. 7534–7539, Dec. 2005.

[101] G. Zhu, J. Levine, L. Praly, and Y.-A. Peter, "Flatness-based control of electrostatically actuated mems with application to adaptive optics: A simulation study," *Journal of Microelectromechanical Systems*, vol. 15, pp. 1165–1174, Oct. 2006.

[102] M. Hosseini, G. Zhu, and Y.-A. Peter, "A new formulation of fringing capacitance and its application to the control of parallel-plate electrostatic micro actuators," *Analog Integr. Circuits Signal Process.*, vol. 53, no. 2-3, pp. 119–128, 2007.

[103] G. Zhu, J. Penet, and L. Saydy, "Modeling and control of electrostatically actuated

mems in the presence of parasitics and parametric uncertainties," *Journal of Dynamic Systems, Measurement, and Control*, vol. 129, no. 6, pp. 786–794, 2007.

[104] G. Zhu and L. Saydy, "Robust output feedback control of an electrostatic microactuator," in *American Control Conference*, pp. 3192–3197, Jul. 2007.

[105] G. Zhu, J. Levine, and L. Praly, "Stabilization of an electrostatic mems including uncontrollable linearization," in *IEEE Conference on Decision and Control*, pp. 2433–2438, Dec. 2007.

[106] G. Zhu, L. Saydy, M. Hosseini, J.-F. Chianetta, and Y.-A. Peter, "A robustness approach for handling modeling errors in parallel-plate electrostatic mems control," *Journal of Microelectromechanical Systems*, vol. 17, pp. 1302–1314, Dec. 2008.

[107] G. Zhu, C.-G. Agudelo, L. Saydy, and M. Packirisamy, "Torque multiplication and singularity avoidance in the control of electrostatic torsional micro-mirrors," in *Proc. World Congress on International Federation of Automatic Control*, pp. 1189–1194, 2008.

[108] C. Agudelo, M. Packirisamy, G. Zhu, and L. Saydy, "Design and experimental validation of a nonlinear tracking control law for an electrostatic micromirror," in *American Control Conference*, pp. 4202–4207, Jun. 2009.

[109] D. Maithripala, J. Berg, and W. Dayawansa, "Capacitive stabilization of an electrostatic actuator: output feedback viewpoint," in *American Control Conference*, vol. 5, pp. 4053– 4058, Jun. 2003.

[110] D. Maithripala, J. Berg, and W. Dayawansa, "Nonlinear dynamic output feedback

stabilization of electrostatically actuated mems," in *IEEE Conference on Decision and Control*, vol. 1, pp. 61–66, Dec. 2003.

[111] D. Maithripala, J. Berg, and W. Dayawansa, "Control of an electrostatic microelectromechanical system using static and dynamic output feedback," *Journal of Dynamic Systems, Measurement and Control*, vol. 127, pp. 443–450, 2005.

[112] D. Maithripala, B. Kawade, I. Wickramasinghe, J. Berg, and W. Dayawansa, "A passivity-based controller for an electrostatic mems model in the presence of parasitics," in *International Conference on Industrial and Information Systems*, pp. 267–272, Aug. 2007.

[113] P. K. C. Wang, "Feedback control of vibrations in a micromachined cantilever beam with electrostatic actuators," *Journal of Sound and Vibration*, vol. 213, no. 3, pp. 537–550, 1998.

[114] D. Piyabongkarn, Y. Sun, R. Rajamani, A. Sezen, and B. Nelson, "Travel range extension of a mems electrostatic microactuator," *IEEE Transactions on Control Systems Technology*, vol. 13, pp. 138–145, Jan. 2005.

[115] W. Li and P. Liu, "Robust adaptive tracking control of electrostatic micro-actuators with uncertainty," in *IEEE/ASME International Conference on Advanced Intelligent Mechatronics*, pp. 471–476, Jul. 2008.

[116] W. Li and P. X. Liu, "Robust adaptive tracking control of uncertain electrostatic micro-actuators with h-infinity performance," *Mechatronics*, vol. 19, no. 5, pp. 591–597, 2009.

[117] K. Tee, S. Ge, and E. Tay, "Adaptive control of a class of uncertain electrostatic microactuators," in *American Control Conference*, pp. 3186–3191, Jul. 2007.

[118] K. P. Tee, S. Ge, and F. Eng Hock Tay, "Adaptive control of electrostatic microactuators with bidirectional drive," *IEEE Transactions on Control Systems Technology*, vol. 17, pp. 340–352, Mar. 2009.

[119] K.-P. Tee, S. S. Ge, and E. H. Tay, "Output-feedback adaptive control of electrostatic microactuators," in *American Control Conference*, pp. 4215–4220, Jun. 2009.

[120] A. Izadian, L. Hornak, and P. Famouri, "Trajectory control of mems lateral comb resonators under faulty conditions," in *American Control Conference*, pp. 3198–3203, Jul. 2007.

[121] A. Izadian, L. Hornak, and P. Famouri, "Structure rotation and pull-in voltage control of mems lateral comb resonators under fault conditions," *IEEE Transactions on Control Systems Technology*, vol. 17, pp. 51–59, Jan. 2009.

[122] *COMSOL Multiphysics MEMS Module Model Library*. 1994.

[123] *COMSOL Multiphysics MEMS Module User's Guide*. 1994.

[124] T. Singh and W. Singhose, "Input shaping/time delay control of maneuvering flexible structures," in *American Control Conference*, vol. 3, pp. 1717–1731, 2002.

[125] A. Fargas-Marques and A. Shkel, "On electrostatic actuation beyond snapping condition," in *IEEE Sensors*, 2005.

[126] Y. Nemirovsky and O. Bochobza-Degani, "A methodology and model for the pull-in parameters of electrostatic actuators," *Journal of Microelectromechanical Systems*, vol. 10, no. 4, pp. 601–615, 2001.

[127] A. Nayfeh, M. Younis, and E. Abdel-Rahman, "Dynamic pull-in phenomenon in mems resonators," *Nonlinear Dynamics*, vol. 48, pp. 153–163, 2007.

[128] B. McCarthy, G. Adams, N. McGruer, and D. Potter, "A dynamic model, including contact bounce, of an electrostatically actuated microswitch," *Journal of Microelectromechanical Systems*, vol. 11, no. 3, pp. 276–283, 2002.

[129] T. Veijola, "Compact models for squeezed-film dampers with inertial and rarefied gas effects," *Journal of Micromechanics and Microengineering*, vol. 14, no. 7, pp. 1109–1118, 2004.

[130] J. Blecke, J. Berg, D. Epp, and H. Sumali, "Rf-mems switch system identification for control," in *International Modal Analysis Conference*, no. 260, 2007.

[131] S. Arimoto, S. Kawamura, F. Miyazaki, and S. Tamaki, "Learning control theory for dynamical systems," in *IEEE Conference on Decision and Control*, vol. 24, pp. 1375–1380, 1985.

[132] Y. Tsypkin, "Self learning - what is it?," *IEEE Transactions on Automatic Control*, vol. 13, no. 6, pp. 608–612, 1968.

[133] K.-S. Fu, "Learning control systems - review and outlook," *IEEE Transactions on Automatic Control*, vol. 15, no. 2, pp. 210–221, 1970.

APPENDIX

A. IEEE Copyright Permissions

The permissions discussed below correspond to the work presented in Chapter 7.

Manager, IEEE Intellectual Property Rights

445 Hoes Lane

Piscataway, NJ 0 8855-1331

Phone: 1-732-562-3966

January 19, 2011

Dear IEEE:

I am completing a doctoral dissertation at Michigan Technological University entitled ”Control Design and Genetic Algorithm Optimization for the Design of Electrostatically Actuated MEMS.” I would like your permission to reprint in my dissertation the following IEEE publication that I authored in 2009:

Title: A simple learning control to eliminate RF-MEMS bounce

Authors: J.C. Blecke (myself), D.S. Epp, H. Sumali and G.G. Parker

Publication: Journal of Microelectromechanical Systems

Issue Date: April 2009

Volume; Issue; Pages: 18; 2; 458-465

ISSN: 1057-7157

INSPEC Accession Number: 10547344

Digital Object Identifier: 10.1109/JMEMS.2008.2007243

Date of Publication: February 27, 2009

Date of Current Version: March 31, 2009

Sponsored by: IEEE Electron Devices Society

The requested permission extends to any future revisions and editions of my dissertation, including non-exclusive world rights in all languages and to the prospective publication of my dissertation by UMI. These rights will in no way restrict your republication of the material in any other form by you or others by you.

If these arrangements meet with your approval, please send me official word. My contact information appears below:

Jill C. Blecke

Email: jcblecke@mtu.edu

Ph: (920) 609-1395

Michigan Technological University

Mechanical Engineering □ R.L. Smith Bldg

1400 Townsend Drive

Houghton, MI 49931

Thank you very much.

Sincerely,

Jill Blecke

Dear Jill Blecke :

In response to your email below, we are happy to grant you this permission to reprint your below described IEEE copyrighted paper in your thesis and have it placed on your university's website. The following requirements must be satisfied before we can consider this permission grant final:

1. The following IEEE copyright/credit notice must be placed prominently on the first page of the reprinted material, with the appropriate details filled in: ©2009 IEEE. Reprinted, with permission, from [author names, paper title, IEEE publication title and month/year of publication].

2. The following message should be displayed at the beginning of the credits or in an appropriate place on the website: This material is posted here with permission of

the IEEE. Such permission of the IEEE does not in any way imply IEEE endorsement of any Michigan Technological University products or services. Internal or personal use of this material is permitted. However, permission to reprint/republish this material for advertising or promotional purposes or for creating new collective works for resale or redistribution must be obtained from the IEEE by writing to pubs-permssion@ieee.org. By choosing to view this material, you agree to all provisions of the copyright laws protecting it.

If applicable, the University Microfilms, Inc. and/or ProQuest may supply single copies of the dissertation.

Sincerely,

Jacqueline Hansson, Coordinator

©©©©©©©©©©©©©©©©©©©©

IEEE Intellectual Property Rights Office

445 Hoes Lane

Piscataway, NJ 08855-1331 USA

1 732 562 3966 (phone)

1 732 562 1746 (fax)

IEEE– Fostering technological innovation and excellence for the benefit of humanity.

©©©©©©©©©©©©©©©©©©©©